

TECHNISCHE
UNIVERSITÄT
WIEN

VIENNA
UNIVERSITY OF
TECHNOLOGY

DIPLOMARBEIT

Porous Hybrid Materials as Carrier for Polymeric Waveguides

Ausgeführt am Institut für
Angewandte Synthesechemie (Bereich Makromolekulare Chemie)
der Technischen Universität Wien

unter der Anleitung von ao. Univ.-Prof. Dipl.-Ing. Dr.tech. Robert Liska
und Privatdoz. Mag. Dr.rer.nat. Helga C. Lichtenegger

durch
Stefan Krivec; 0101136
9241 Wernberg, Birkenweg 23

Die Arbeit entstand im Zuge des STRUCMAT Projektes, Materialentwicklung für die Strukturierung mit Zwei-Photonen-Lithographie, Bestandteil des Projektclusters ISOTEC im Rahmen der Österreichischen Nano Initiative. An dieser Stelle möchte ich auch für die finanzielle Unterstützung durch den FWF danken.

Frau Priv.-Doz. Mag. Dr. Helga Lichtenegger vom Institut für Werkstoffwissenschaft und Werkstofftechnologie und Herrn ao. Univ.-Prof. Dipl.-Ing. Dr. Robert Liska vom Institut für Angewandte Synthesechemie möchte ich an dieser Stelle für die interessante Themenstellung, die ausgezeichnete Betreuung, wertvolle Anregungen und Diskussionen während meiner Arbeit sowie für die angenehme Arbeitsatmosphäre danken.

Desweiteren möchte ich hiermit folgenden Personen danken:

Herrn Dr. Thomas Koch vom Institut für Werkstoffwissenschaft und Werkstofftechnologie für die Unterstützung und die wertvollen Ratschläge bei den Nano-Indentation Messungen.

Frau Dr. Marie Neouze vom Institut für Materialchemie für die Durchführung der N₂-Adsorptions Messungen.

Herrn Dr. Volker Schmidt und Herrn Dr. Valentin Satzinger vom Joanneum Research in Weiz für die reibungslose Durchführung der Zwei Photonen Strukturierung.

Frau Dr. Nadejda Matsko vom FELMI-ZFE an der Technischen Universität Graz für die Aufnahme der AFM Bilder und die damit verbundene Probenpräperierung.

Frau Mag. Nicole Galler vom Institut für Experimentalphysik an der Karl-Franzens Universität Graz für die Lichteinkopplungsversuche

Mein Dank gilt auch allen Kolleginnen, Kollegen und Mitarbeitern beider involvierten Institute, die mich in meiner Arbeit unterstützt und zu einem positiven und angenehmen Arbeitsklima beigetragen haben.

Mein ganz spezieller Dank gilt meinen Eltern Sieglinde und Felix, die mir das Studium ermöglicht und mich immer vorbehaltlos unterstützt haben.

Danke meiner Freundin Martina für die Liebe, die Geduld und das Verständnis.

KURZFASSUNG

Im Signaltransfer zwischen elektronischen Komponenten haben optische Lichtwellenleiter gegenüber Kupferleiterbahnen viele Vorteile, wie zum Beispiel kein auftretender Ohmscher Widerstand oder die höhere Übertragungsrate bei gleichem Querschnitt. In dieser Arbeit wurden silikatbasierende transparente nanoporöse Monolithen und dünne Schichten hergestellt und auf ihre Eignung als Trägermaterial für polymere Lichtwellenleiterbahnen geprüft. Solche Systeme haben Potential für den Einsatz in der Leiterplattentechnik, um mittels generieren von optischen Verbindungen via Zwei Photonen Polymerisation (TPP) vorgegebene elektronische Komponenten nachträglich miteinander zu verbinden. Durch die Zugabe des Siliziumprecursors Tetramethoxysilane (TMOS) zu einem lyotropischen flüssigkristallinen (LCC) L_3 Phasen Template konnte ein durchgehend nanoporöses Trägermaterial mit einem einstellbarem Porendurchmesser von 80 – 280 nm hergestellt werden, welches sich zur Infiltration durch ein Monomer eignete. Um die mechanischen Eigenschaften des Materials zu verbessern, wurden anorganische-organische Hybridmoleküle auf Basis von Polyethylenglykol in verschiedener Kettenlänge als Co-Precursor hinzugegeben. Nach aushärten einer Mischung aus TMOS und Co-Precursors, konnte das eingesetzte Template mittels Lösungsmittel und, bei monolithischen Proben, zusätzlicher Soxhlet Extraktion wieder entfernt werden, wodurch flexibles und rissfreies Trägermaterial erhalten werden konnte. Anschließend wurde ein geeignetes Acrylat-Monomer infiltriert und durch UV-Bestrahlung gehärtet. Die Wahl des Monomers musste hinsichtlich eines Brechungsindexunterschiedes von $n_D^{20} \geq 0.003$ zwischen Träger und Leiterbahn bei zusätzlich erhaltener Transparenz des Gesamtsystems getroffen werden. Thermogravimetrische Analysen zeigten die Zersetzung des Trägermaterialies als auch den Gehalt an aufgenommenem Monomer in den Poren, deren Größe und Verteilung mittels Atomic Force Microscopy erfasst wurde. Durch Nano Indentation konnte mit steigender Co-Precursor Konzentration und mit länger werdender Polyethylenglykol-Kettenlänge eine Abnahme der Indentation-Härte als auch des Indentation-Moduls festgestellt werden, resultierend in einer erhöhten Resistenz gegen Rissbildung im Material. Schlussendlich wurden auch noch erfolgreich erste Versuche zur Strukturierung von Lichtwellenleitern im Trägermaterial mittels TPP unternommen.

ABSTRACT

For signal transfer between electronic device components, the use of optical waveguides has various advantages over conventional copper circuits: a higher transmission rate at constant cross-section, no heating up due to lack of ohmic resistance, limitation of cross-talk between adjacent circuits etc. In this work, silica-based transparent nanoporous monoliths and thin films were investigated for use as carrier material for polymeric waveguides to be inscribed into the solid host structure by selective polymerization. Such an approach should enable also direct writing of waveguides as interconnects between pre-aligned components of integrated circuits by two photon polymerization (TPP). By adding the silica precursor tetramethoxysilane (TMOS) to a lyotropic liquid crystalline (LCC) L_3 “sponge” phase template, a continuous nanoporous system with adjustable channel dimensions of about 80 - 280 nm was fabricated via sol-gel processing that could be infiltrated with monomer. The composition of the carrier was varied by adding various inorganic-organic hybrid compounds as co-precursor consisting of sol-gel compatible silica-heads with an organic polyethyleneglycol spacer, in order to adjust the mechanical properties. After hardening of the precursor via sol-gel process, the template was removed by both solvent exchange and, as required for monolithic samples, additional Soxhlet extraction. The carrier material was infiltrated with an appropriate monomer, whereas the appropriate choice of the monomer ensured a refractive index gap between carrier and waveguide of $n_D^{20} \geq 0.003$ and full transparency, properties necessary to use the polymeric structures as effective waveguides. Thermogravimetric analysis gives an insight both in the thermal decomposition of the material and in the materials content of pores, accessible for monomer infiltration. Nano-indentation experiments of the carrier material showed a distinct decrease of indentation hardness and indentation modulus with increasing concentration and spacer length of the co-precursor. A higher co-precursor concentration also led to an improved stability of the final carrier material, i.e. appearance of cracking could be suppressed and completely avoided, respectively. By Atomic Force Microscopy cross-section images of the various material compositions could be made as well as an investigation of the pore sizes and their distribution. Last but not least, first successful tests to inscribe waveguides via TPP were carried out, verifying the operability of the approach and hence opening a promising field of further development.

TABLE OF CONTENTS

1. INTRODUCTION	1
1.1. True Liquid Crystal Templating	3
1.2. Sol-Gel Process of Silica Compounds	10
1.3. Structuring of Waveguides by Two Photon Polymerisation	14
1.4. State of the Art of Silica – Based Nanoporous Materials.....	15
2. METHODS	18
2.1. Silica Sources	18
2.2. Mesoporous Template	21
2.3. Calculation of the Initial Weights	22
2.4. Monomers.....	24
2.5. Preparation of the Carrier Material	25
2.5.1. Sol-Gel Transition	25
2.5.2. Solvent Exchange	26
2.5.3. Extraction of the Template	27
2.6. Generating Waveguides	27
2.6.1. Infiltration with Monomer.....	27
2.6.2. Two Photon Polymerisation	29
2.7. Determination of Thermal Properties.....	29
2.7.1. Thermogravimetric Analysis.....	29
2.7.2. Differential Scanning Calorimetry	31
2.8. Determination of Mechanical Properties.....	31
2.8.1. Indentation Hardness (H_{IT}).....	33
2.8.2. Indentation Modulus (E_{IT}).....	34
2.8.3. Plastic and Elastic Parts of the Indentation Work	35
2.9. Structural Properties	36
2.9.1. Scanning Electron Microscopy	36
2.9.2. Atomic Force Microscopy.....	37
3. EXPERIMENTAL	39
3.1. Synthesis of the Co-Precursor Compounds	39

3.1.1.	Synthesis of Bismuth(III)hexanoate.....	39
3.1.2.	Synthesis of Co-Precursors with different PEG chain lengths.....	40
3.2.	Generation of the L ₃ “Sponge” Phase Template.....	42
3.3.	Preparation of the Carrier Material	43
4.	RESULTS	47
4.1.	Gel Time	48
4.2.	Refractive Indices	49
4.3.	Observation of the Carrier Material throughout Preparation.....	52
4.3.1.	General Considerations	52
4.3.2.	Mass Loss	55
4.3.3.	Removal of Template	57
4.3.4.	Shrinkage.....	59
4.4.	Thermal Properties	61
4.4.1.	Thermal Behaviour of the Co-Precursor	61
4.4.2.	Suitability of Monomers for Infiltration.....	64
4.4.3.	Monomer Content in the Carrier Material.....	65
4.5.	Mechanical Properties	68
4.5.1.	Indentation Hardness (H _{IT}).....	69
4.5.2.	Indentation Modulus (E _{IT}).....	71
4.5.3.	Plastic and Elastic Parts of the Indentation Work	72
4.6.	Structural Properties	74
4.6.1.	Scanning Electron Microscopy (SEM).....	75
4.6.2.	Atomic Force Microscopy (AFM)	76
4.7.	Two Photon Polymerisation.....	79
4.7.1.	Varying the Laser Power.....	80
4.7.2.	Varying the Speed of Structuring.....	82
4.7.3.	Functionality of Waveguides.....	84
5.	SUMMARY	88
	MATERIALS, DEVICES, ANALYSIS.....	94
	ABBREVIATIONS.....	95
	REFERENCES.....	96

1. INTRODUCTION

Nowadays, printed circuit boards (PCB) in electronic devices conventionally are based on copper circuits. With decreasing size of the PCB several problems such as overheating, limited signal transfer rates and cross-talk between neighbouring circuits arise. This situation could be considerably improved by use of optical interconnections such as waveguides. And indeed, in the last couple of years the idea to integrate optical interconnections in PCB raised a great deal of interest worldwide.¹

In general, optical waveguides are structures in which a commonly dielectric material with a high permittivity (i.e. the transmission of an electric field in a dielectric medium) and thus a high refractive index is surrounded by a cladding material with a lower refractive index. The structure guides light waves from one point to another by total internal reflection (fig. 1). The most common applications of optical waveguides are optical fibres made of polymers or glass.

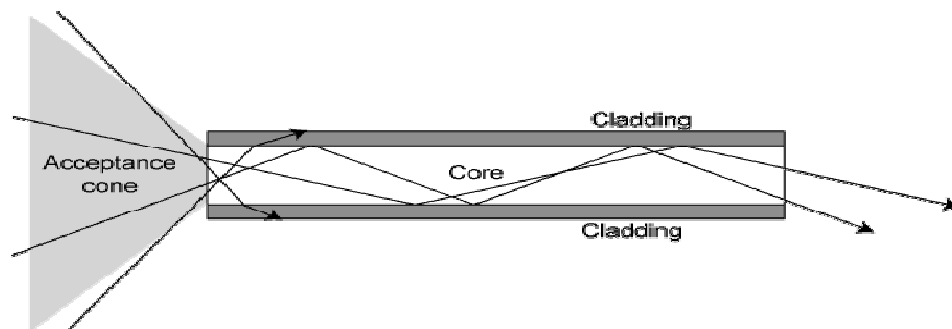


Figure 1: The idea of waveguiding

As mentioned above, a further possible application of the waveguiding concept is signal transfer in PCB.¹ An approach was developed by the integration of thin films of an optical material in which waveguides can be structured. The structuring can be done by using several technologies like photolithography,² ablation,³ embossing,⁴ or direct laser writing⁵. Especially the latter has gained remarkable interest by the application of two photon adsorption (TPA) structuring. Nowadays, a commonly used optical material class

Introduction

are ORMOCERS[®]; silica based inorganic-organic hybrid polymers with outstanding properties resulting from their inorganic and organic units.^{6, 7} Hence waveguides can be produced within one material class.⁸ Additional advantages of ORMOCERS[®] are the good adhesion on most substrates as metalized Si-wafers, inorganic glasses and polymers. The thermal stability is high enough for most of the technological applications and the refractive index is tuneable by mixing various resins.

The aim of this work was to develop an alternative mechanically and thermal stable optical material for the structuring of waveguides. Since silica-based materials have commonly rather low refractive indices, the development of a silica-based porous carrier material, which can be infiltrated with a photocurable monomer with a high refractive index for subsequent structuring of waveguides by two photon polymerisation (TPP; theory: chapter 1.3), was considered to be a suitable solution. This implied several requirements for the material, for instance full transparency and the ability to withstand the stress of monomer infiltration. Unlike well known one component approaches for waveguide structuring, as the application of ORMOCERS[®], the work focused on a two component system consisting of different materials for the waveguide and the surrounding carrier, respectively. A related research project at the Vienna University of Technology is based on the use of a polydimethylsiloxan matrix as carrier material, which can be swollen by a photocurable monomer.⁹ In contrast, in this work a porous, silica based matrix should be employed as host material suitable to be infiltrated with monomer. Based on the idea of true liquid crystal templating (theoretical background: chapter 1.1), appropriate silica precursors were applied on lyotropic surfactant aggregates with a defined porosity, in order to generate the host matrix by sol-gel processing (theory: chapter 1.2). Note that on the one hand the pore diameter had to be large enough to enable the infiltration of monomers but on the other hand the pores had to be considerably smaller than the wavelength of visible light, in order to avoid light scattering and thus a limitation of the materials transparency. These requirements were met by mesoporous silica with controlled porosity. Moreover, silica material exhibits a very low refractive index, making it a promising carrier material for optical waveguides. Tetramethoxysilane (TMOS) is a commonly used precursor in sol-gel chemistry, but with the disadvantage of resulting in very brittle glass-like solids, that usually results in

cracking in the course of the preparation process. An enhancement of the commonly applied precursor by addition of inorganic-organic hybrid molecules with flexible polyethyleneglycol chains as co-precursor was considered to improve the mechanical properties of the carrier material combined with a retained ability to monomer uptake. The improvement should prevent cracking of the material to make it suitable for applications in various fields with the respective requested geometries, as for instance monolithic shapes or thin layers. Furthermore, the monomer used for infiltration should retain its transparency even after curing and to guarantee waveguiding ability after structuring by TPP, its refractive index had to exhibit a considerable increase compared to those of the hosting material. The system should also be stable and free of cracking when the remaining uncured monomer is removed after the process of waveguide structuring. Last but not least, waveguides should be inscribed in the synthesized host matrix by TPP and tested in their functionality by incoupling of lightwaves.

1.1. True Liquid Crystal Templating

Nowadays, liquid crystal phases have a broad relevance for technical applications. Unlike liquids these phases have a certain degree of regularity, but lower than those of solid crystals. Regarding their behaviour, liquid crystal phases can be classified as by thermotropic or, relevant for this work, lyotropic. Thermotropic liquid crystals are governed by variations in their appearance caused by temperature changes. However, lyotropic liquid crystals (LLC) are usually made by self-assembly of amphiphilic molecules in a solvent. Among other parameters like temperature, LLC phases are governed by the composition of the system.

Amphiphilic molecules consist of a hydrophobic part (“tail”) and a hydrophilic part (“head”), denoting that one part is soluble in water and the other one remains unsolved. In general, these types of molecules, also known as surfactants, can be classified as non-ionic, cationic, anionic and amphoteric, depending on the charge of the hydrophilic head. The hydrophobic tail consists commonly of an aliphatic hydrocarbon chain. Examples for amphiphiles are block copolymers, proteins or polysaccharides.

Introduction

Specifying the behaviour of micelles and LLC in solution, it is obvious that the concentration of surfactant in the solvent is a crucial parameter. Already low amounts of surfactant trigger a spherical self-assembly of the molecules, known as micelle (fig. 2).

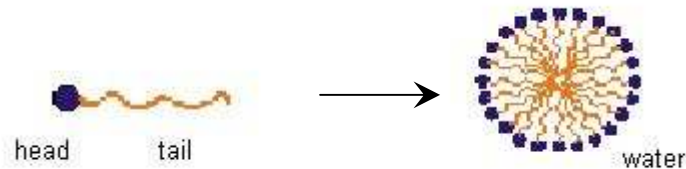


Figure 2: Generation of micelles from surfactants

The reason is the following: The more surfactants are gathered on the water surface, the lower becomes the surface tension. When the surface is entirely occupied with surfactant molecules (critical micelle formation concentration; CMC) the surface tension does not decrease anymore and certain structures in the solvents interior will be generated, depended on the type of surfactant (e.g. micelles).¹⁰

In water, the molecules are arranged such that the hydrophilic heads compose a spherical interface between the hydrophilic solvent and the hydrophobic interior of the micelles. Increasing the concentration of the surfactant in the solvent can cause intermicellar repulsive forces and hence release an agglomeration of the micellar structures up to three dimensional LLC structures (fig. 3). In general, the self-assembled morphology can be roughly classified as discrete or infinitely connected.

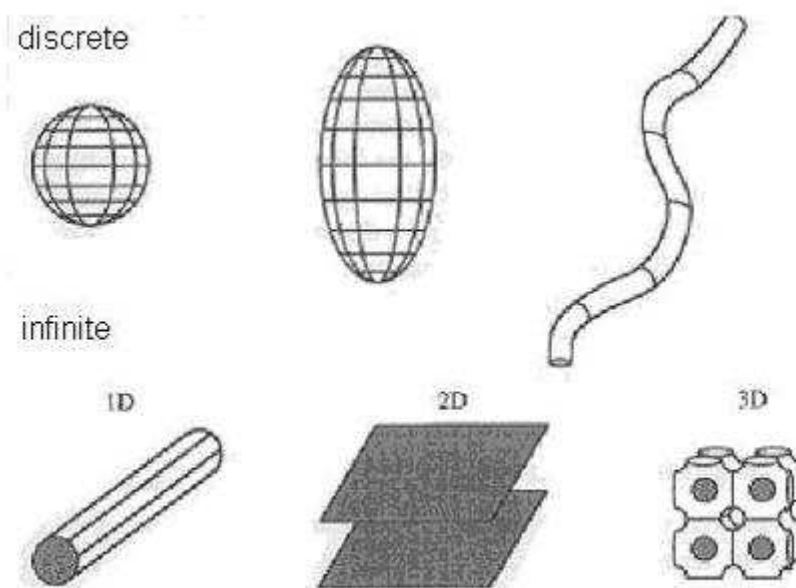


Figure 3: Possible structural variants for aggregation of surfactants

However, the ability to generate a certain structure is associated with the type of the respective surfactant molecule. The morphology of the aggregates now essentially depends on the energetically most favoured local curvature of the aggregates¹¹ or equivalently on the most favoured ratio of the head group area to the volume of the lipophilic tails. For the latter, Israelachvili and co-workers developed a method to predict structures, which can be obtained by a certain surfactant.¹²

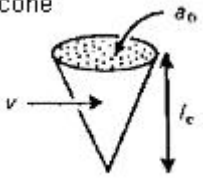
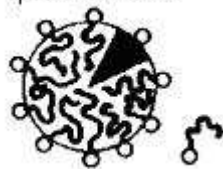

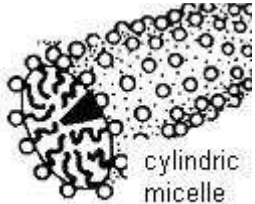

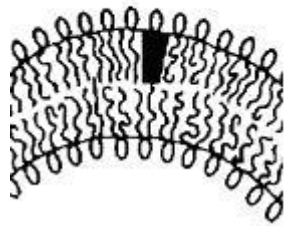

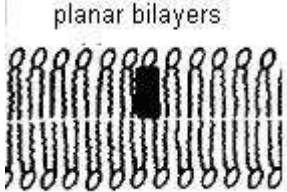

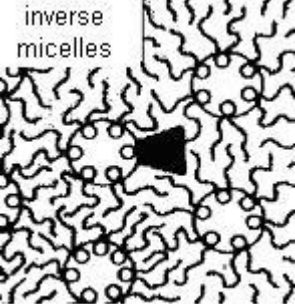
$$CPP = \frac{v_t}{a_0 \cdot l_0} \quad (1)$$

CPP	critical packing parameter; form factor
v_t	volume of the hydrophobic part (“tail”) [m ³]
a_0	area of the hydrophilic part (“head”) [m ²]
l_0	maximum length of the hydrophobic part [m]

For systems consisting of surfactant and solvent (i.e. water) the formation of the following structures are favoured, depending on the form factor (Table 1).¹³ Note the used solvent for all the surfactants is water:

Introduction

Table 1: Form factor of surfactants and the resulting structures

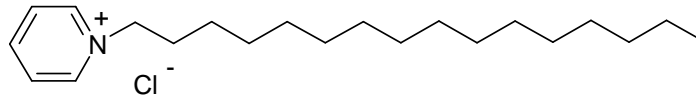
CCP acc. to lit. ¹² and eq. (1)	critical packing form	favoured structure	examples for surfactants
$< 1/3$	cone 	spheric micelle 	Surfactants with large heads and one tail. e.g.: Sodium dodecylsulphate, 1-hexadecylpyridinium chloride monohydrate
$1/3 - 1/2$	truncated cone 	cylindric micelle 	Surfactants with small heads and one tail. e.g.: Cetyltrimethylammoniumbromide
$1/2 - 1$	truncated cone 	flexible bilayers, vesicles 	Surfactants with large heads and two flexible tails. e.g.: Dialkyldimethylammonium surfactants (DDAS)
~ 1	cylinder 	planar bilayers 	Surfactants with small heads and two tails. e.g.: Phosphatidylethanolamine
> 1	inverse truncated cone 	inverse micelles 	Surfactants with small heads and two flexible tails. e.g.: Unsaturated phosphatidylethanolamine

However, by the help of an auxiliary chemical, aggregations of surfactants can be modified. For example, 1-hexanol with a short hydrocarbon chain and a small hydrophobic group lowers the rigidity of the structure caused by its placement in the interior.¹⁴ The $-OH$ groups of the alcohol should decrease any electrical and mechanical

Introduction

repulsion between the surfactant polar heads.¹⁵ Thus structural transitions can be controlled by varying the ratio of auxiliary chemical to surfactant. Moreover, non-ionic surfactants are also known to change its aggregation form by elevated temperature.

As example the addition of 1-hexanol to a system of the surfactant 1-hexadecylpyridinium chloride monohydrate (alternative name: cetylpyridinium chloride monohydrate; CpCl·H₂O) in the solvent water (in fig. 4 a 0.2 M NaCl solution serves as solvent) will be explained in more detail in the following: Fig. 4 shows a pseudo-binary representation (1-hexanol and surfactant as ratio on the y-axis) of a quasi-ternary phase diagram.¹⁶ The solvent content of the system has a range of 53 to >98 wt%:



1-Hexadecylpyridinium chloride monohydrate

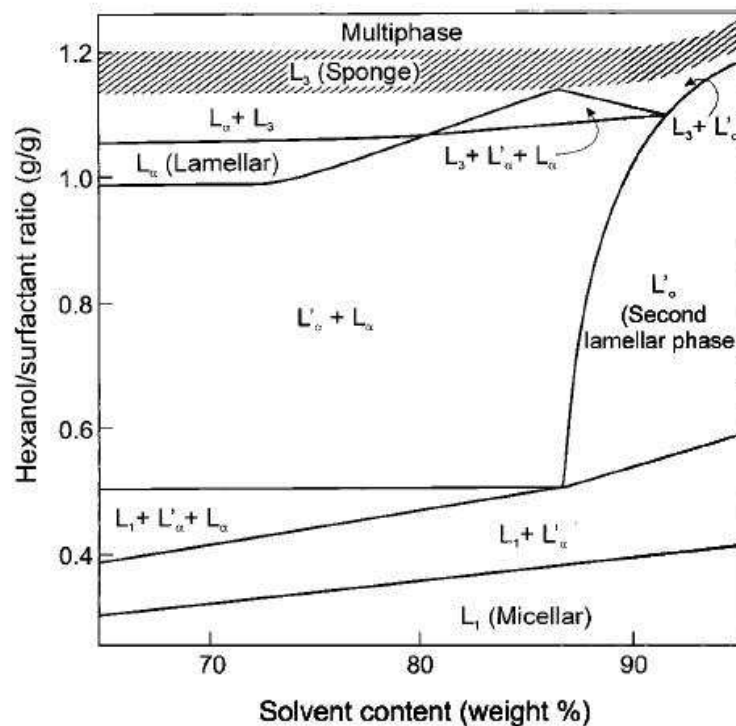


Figure 4: Phase diagram of the 1-hexanol / surfactant / solvent system

According to its form factor, pure $\text{CpCl}\cdot\text{H}_2\text{O}$ in water favours a micellar structure (L_1). Addition of 1-hexanol and hence an increase of the hexanol/surfactant ratio, alters the shape of the structure. First a mixture of micelles with a type lamellar LLC structure ($L_1 + L_\alpha'$) occurred, followed by a mixture of different lamellar structures ($L_\alpha' + L_\alpha$). After reaching a pure lamellar structure (L_α) a special phase became thermodynamically favoured (L_3 , the so-called “sponge” phase, highlighted in Figure 4). It consists of a three-dimensional continuous connected pore system with bilayer membranes, dividing the solvent volume into two equal continuous parts (fig. 5).¹⁷ Since the phase behaviour remained the same, 0.2 M HCl can be used instead of the 0.2 M NaCl solution to achieve the same results.^{14, 18} That implies that, in either solvent, the electrostatic interactions between headgroups are similar

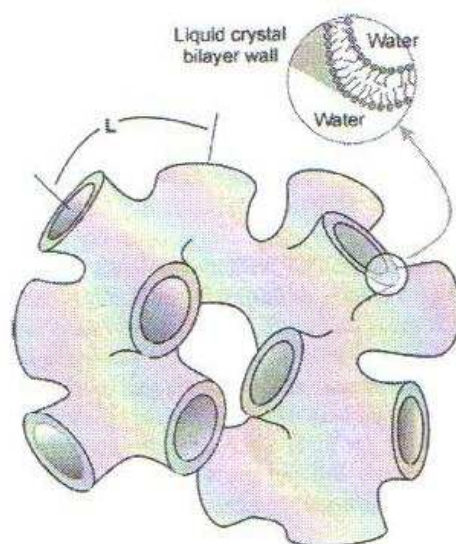


Figure 5: Schematic drawing of the L_3 “sponge” phase

The L_3 “sponge” phase was first observed experimentally in the early 1980’s and subsequently extensively studied regarding its physical properties.¹⁹ Apart from $\text{CpCl}\cdot\text{H}_2\text{O}$ various other surfactants were observed to show a transition from the micellar phase into the L_3 “sponge” phase by adding an auxiliary chemical as 1-hexanol or resembling homologous compounds. For instance cetyldecylpyridinium bromide,²⁰ dodecyldimethylaminoxide²¹ or octylbenzenesulphonate²² were also able to achieve the transition. In literature various thermodynamic calculations¹⁵ and mathematical models²³

of surfactant / solvent systems can be found. A crucial parameter for the behaviour of bilayer LLC Phases is the bending energy as function of the mean curvature modulus κ , the Gaussian curvature modulus $\bar{\kappa}$ and the bending rigidity. Strong positive values of $\bar{\kappa}$ favour the formation of micellar structures, whereas negative values favour the formation of a multiconnected large aggregate structure.^{18, 19} For charged surfactants, the charge density on the membrane has also a strong influence on κ and $\bar{\kappa}$, and hence also the pH value of the solvent has to be taken into account. Assuming a sufficient concentration of surfactant in the solvent, a Gaussian curvature of $\bar{\kappa} = 0$ would result in a L_α lamellar phase, however a negative value leads to the L_3 “sponge” phase, with local variations of $\bar{\kappa}$ from 0 to the minimum, i.e. the interface between aqueous and nonaqueous regions bends away from the hydrocarbon chains of the amphiphile.¹⁴ As dilution of the system exceeds values of 99 wt% solvent content (fig. 4), the L_3 “sponge” phase may be charged to a vesicular phase L_{ves} .¹⁵

Based on an appropriate template, the idea of true liquid crystal templating implies the conversion of the surfactant morphologies into an inorganic replica via addition of liquid precursors that may fill empty spaces and solidify e.g. via the sol-gel transition. The approach corresponds to nanocasting of materials²⁴ where the self assembled morphology of soft matter is “hard copied” into inorganic hard matter (fig. 6).

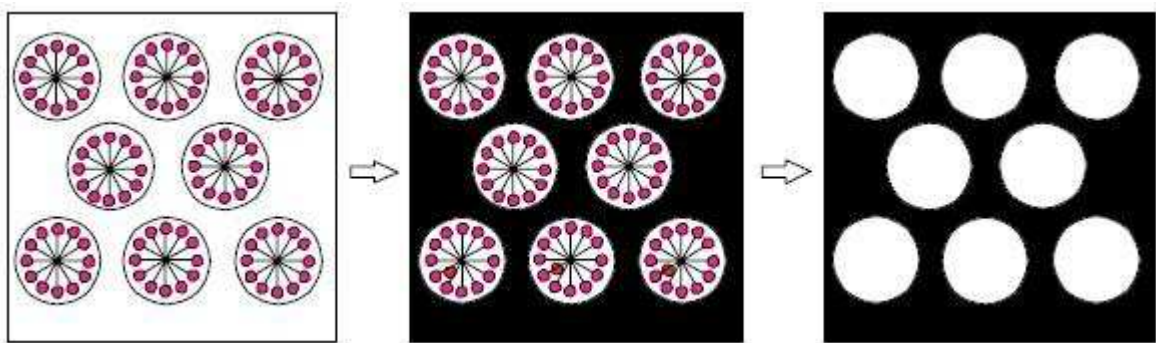


Figure 6: The principle of true liquid crystal templating

The casting process starts at the surface of the LLC phase and hence various interactions have to be taken into account for the interface between the template and the inorganic

precursor. After solidification of the inorganic phase, the template is removed and a solid negative replica of the original phase is obtained.

For pore-like aggregates, the mass relation of surfactant, auxiliary chemical and solvent determines the pore size. Three different size regimes are defined by IUPAC.²⁵

- Micropores: pore diameters < 2 nm
- Mesopores: pore diameters 2 - 50 nm
- Macropores: pore diameters > 50 nm

But the approach is also related with problems. For instance, sol-gel transition releases alcohol from hydrolysis and condensation reactions (chapter 1.2.), and many lyotropic surfactant phases are incompatible with it.²⁶

1.2. Sol-Gel Process of Silica Compounds²⁵

The sol-gel process can be described as the creation of an oxide network by progressive polycondensation reactions. This method enables a soft chemical approach to synthesise amorphous oxide materials.

- A “sol” is a stable suspension of colloidal solid particles of polymers in a liquid. The particles can be amorphous or crystalline.
- A “gel” consists of a porous three dimensional continuous solid network surrounding and supporting a continuous liquid phase. In most sol-gel systems, gelation (i.e. sol-gel transition) is due to the formation of covalent bonds and hence irreversible. Other interactions could be hydrogen bonds or van der Waals forces.

Compounds serving as silica sources for the sol-gel transition are silica containing precursors, where tetraalkoxysilanes ($\text{Si}(\text{OR})_4$) are the most common ones.

In general, the sol-gel process can be divided into several steps:

Hydrolysis and condensation of the molecular precursors: The formulation of sols.

The basic chemistry behind sol-gel processing is the transformation of Si-OR and Si-OH containing species to siloxane compounds by condensation reactions. The mechanism can be depicted by a simple scheme, but the process is more complex since hydrolysis and condensation compete with each other during all steps. Fig. 7 shows some of the intermediates that can be obtained in the initial stages of the reaction using Si(OR)₄:

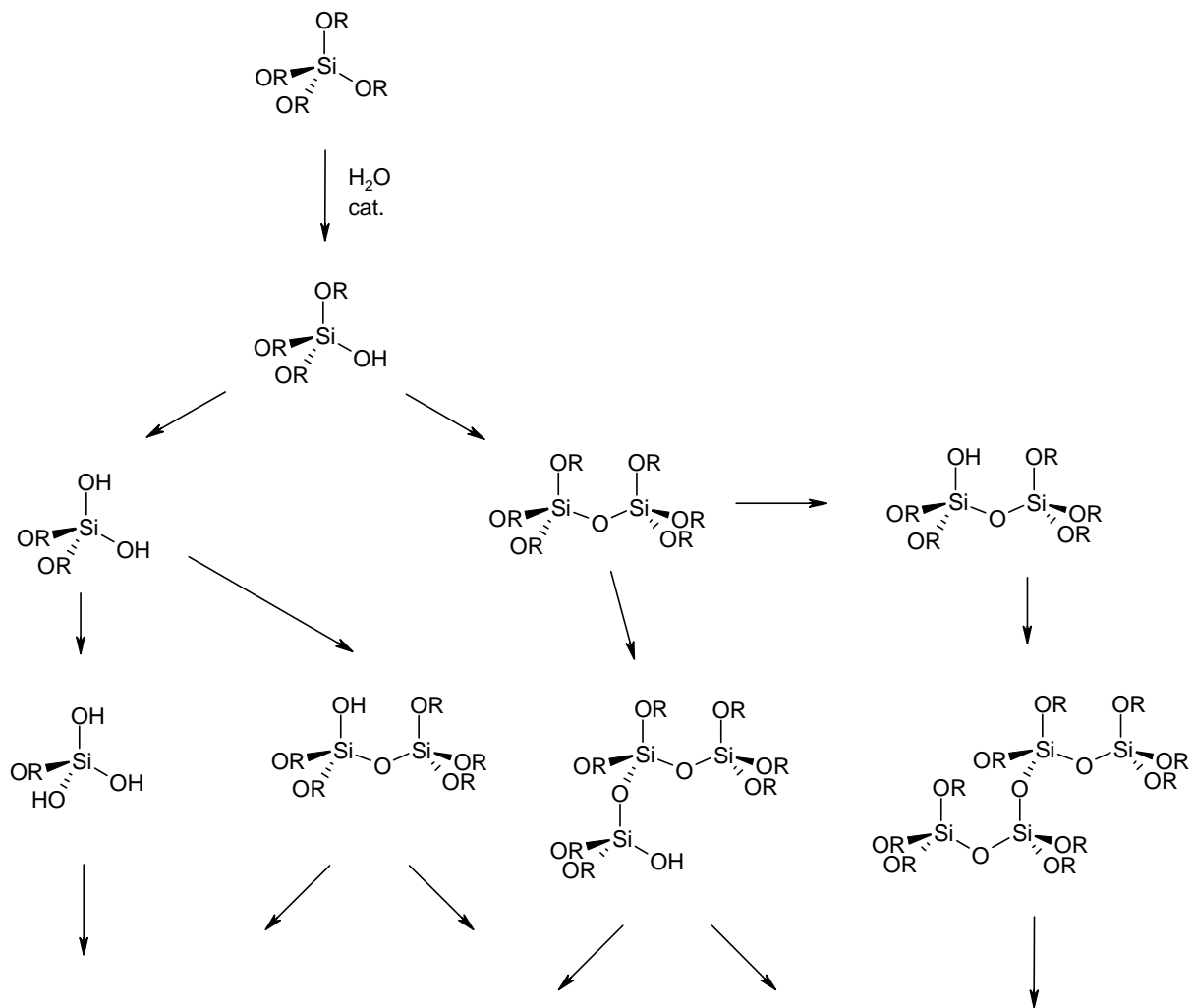
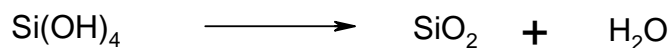


Figure 7: Initial stages of the hydrolysis and condensation steps using Si(OR)₄

The rate of hydrolysis and condensation reactions, respectively are influenced by various factors during in the conversion process.

- The kind of solvent
- Temperature

- pH value
- Steric and inductive effects of the precursors. In fact, branching of the alkoxy group or increasing of the chain length lowers the hydrolysis rate. The substituents attached to a silicon atom are very important regarding the electron density on the central Si-atom. For acidic conditions, precursors with aliphatic organic groups (e.g. RSi(OR)_3) increase the electron density and hence the reaction rate. In mixtures of tetraalkoxysilane and substituted alkoxy silane the different reaction rates can lead to phase separation.
- In aqueous solutions: The alkoxy group to water ratio (R_w). For sol-gel processes the overall reaction is the following:



That implies that two equivalents of water are necessary to convert one molecule of a tetraalkoxysilane (i.e. four alkoxy groups) to SiO_2 ($R_w = 2$). As a general rule, $R_w \gg 2$ favours the condensation reaction, and $R_w \leq 2$ favours hydrolysis.

Sol-gel transition (gelation)

In the initial phase of the gelation, three dimensional oligomeric particles as nuclei are generated, with $-\text{OH}$ groups on their outer surface followed by an aggregation of the oligomers to larger particles with polymeric substructures. Due to electronic effects acidic conditions lead to the generation of linear structures (Reactions are favoured on terminal Si-atoms \rightarrow three dimensional polymer like network) and basic conditions lead to branched structures (Reactions are favoured in the middle of the chains \rightarrow spherical agglomerates). As the aggregation and condensation carries on, the viscosity of the sol increases gradually until the sol-gel transition (gel point) is reached and hence a continuous network, the wet gel, is formed. The gel time (t_{gel}) is the time at which the gel point is reached after starting the hydrolysis and condensation reactions. The volume of the gel in this stage is the same as that of the original precursor solution. The gel time is generally depended on the rate of hydrolysis and condensation reactions as mentioned above. A simple picture for gelation is that the particles grow by aggregation or

condensation until they collide to give clusters of particles. The clusters become bigger and bigger by repeated collisions until the last link between two giant clusters of particles form the gel (mathematically described by the percolation theory). Note that gelation is no thermodynamic event by the last bond of the formation.

Aging

At the gel point, a considerable number of hydroxyl and alkoxy groups that haven't reacted yet are still present, but the sharp increase of viscosity freezes the gel body in a particular network structure. Hence the chemical reactions are not finished at t_{gel} and structural rearrangements take place in the wet gels ("aging" of the gels). This phenomenon occurs because:

- The gel network still contains a continuous liquid phase which is in fact a sol that eventually can condense to the existing network.
- The network is still flexible, allowing neighbouring Si–OH or Si–OR groups to approach and react with each other. This causes shrinkage of some gels as long as the gel exhibits sufficient flexibility. Driving force is the reduction of the large solid-liquid interface.
- Due to the reversibility of hydrolysis and condensation reactions, mass can be dissolved from thermodynamically unfavourable regions and again condensed to more favoured regions.

Drying

This step describes the evaporation of pore liquid from a wet gel by conventional methods, i.e. by temperature increase or pressure decrease. Three different stages can be distinguished:

- During the drying procedure, the gel shrinks by that volume that was previously occupied by the liquid, causing a decrease of the pore size accompanied by a rise of the surface tension in the pore liquid and an increase of the networks stiffness. The liquid flows from the interior of the pores to the surface.
- As the network becomes too stiff for further shrinkage, the tension in the gel reaches a point that makes cracking very likely. The liquid/gas interface retreats into the body, but with a remaining liquid film on the pore walls.
- The liquid film is ruptured and liquid eventually remains only in isolated pockets.

Usually, conventional drying methods like heat treatment result in a collapse of the gel body to a powder (Xerogel). However, certain drying procedures (e.g. supercritical drying with CO₂ or EtOH) enables the retain of the gel body volume by replacing the pore liquid by air (Aerogel).

1.3. Structuring of Waveguides by Two Photon Polymerisation

The concept of multi photon absorption was theoretical predicted by Maria Goeppert-Mayer already in 1931, but experiments failed due to the high necessary intensity of light. In the last couple of years, three dimensional structuring of waveguides in an appropriate photocurable medium, like a monomer, by two-photon absorption (TPA) laser structuring using the two photon polymerisation (TPP) process raised a big deal of interest. This rather new and innovative method enables the realization of optical circuits in a special thin layer.¹ To trigger the photoinitiation, it is necessary to achieve the excited state of suitable initiator molecules by absorption of a certain amount of energy by photons. In two photon polymerisation the material is polymerized not by one UV photon, as for single photon absorption, but by simultaneous absorption of two photons at a longer wavelength, usually in the red-near-infrared (NIR) spectral range (left hand image of Figure 8). To trigger the generation of radicals and hence the polymerisation, the sum of energy of both photons have to fulfil the resonance-requirement for an excited electronic state.

By pulsing the laser in femto second intervals, the intensity of the NIR laser can be remarkably increased. Focusing the laser by a lens decreases the diameter of the beam resulting in a further increase of the intensity (right hand image in fig. 8). Therefore, since the polymerisation rate has a dependence on the square of the light intensity, the likelihood to induce photopolymerisation by the simultaneous absorption of two photons by an appropriate photoinitiator (PI) is constricted to the focal volume of the laser beam.^{27, 28} In contrast, single photon adsorption has a linear dependence of the light intensity, i.e. polymerisation could be triggered in the entire beam path through the sample, with a decreasing rate across the sample as light is adsorbed.

For TPP, since common monomers have a negligible linear absorption in the NIR range, the laser can penetrate deeply into materials and hence polymerisation can be induced exclusively inside the focal volume. By TPP, a spatial resolution down to 100 nm can be achieved.

Apart from the mentioned generation of optical circuits by waveguides, TPP has various fields of application as for example the fabrication of complicated 3-D microstructures

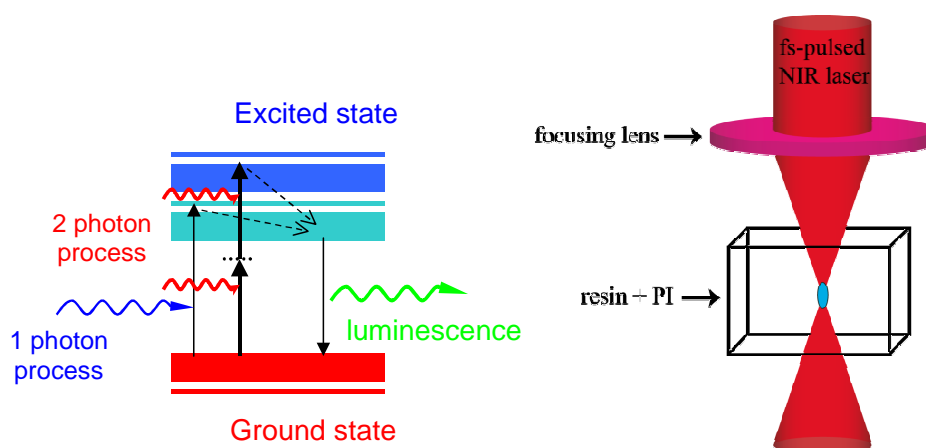


Figure 8: Single photon adsorption vs. two photon adsorption

1.4. State of the Art of Silica – Based Nanoporous Materials

In 1992 members of the Mobil Research and Development Cooperation presented the MCM-41 (Mobil Composition of Matter) as member of the M41S family, a molecular sieve with zeolitic structure and hence the first example of a mesostructured material was synthesized with a material made by calcination of aluminosilicate gels based on an ordered hexagonal array of cylindrical micelles.^{29, 30} The MCM approach described a development of a ordered pore structure, obtained from a non-ordered surfactant solution by co-precipitation with a condensing sol-gel mixture throughout the condensation process. This released a development for the formation of mesoporous material by amphiphile / water systems, due to the high potential of such material in various fields of application. The approach of true liquid crystal templating (chapter 1.1) with addition of a

suitable silica precursor, starting from an organized liquid crystal phase, gained a great deal of interest. One pathway to control and retain the surfactant mesophase geometries and structure morphologies contained the use of non-ionic amphiphiles as structure directing agent.³¹ Hexagonal and cubic templated amorphous monolithic silica structures with 3 nm channel size and full transparency were prepared based on true liquid crystal templating. A remarkable example is the use of non-ionic amphiphilic triblock copolymers of the Pluronic type (Polyethyleneoxy_m-Polypropyleneoxy_n-Polyethyleneoxy_m; e.g. P123, F127) in acidic conditions, the so called SBA (Santa Barbara Amorphous) materials, which enabled the synthesis of highly ordered mesoporous silica structures in cubic, hexagonal and lamellar symmetries up to 30 nm pore size depending on the applied surfactant.³² Hydrogen bonds stabilized the interface between silica-compound and surfactant (ether oxygens of the polyalkyl compound). Hence, transparent and porous monolithic samples were accessible by addition of tetraalkoxysilane to the LLC, whereas the resultant material conformed to the shape of the container in which it forms.^{33, 34} Another route to porous silica materials included the assembly of cationic amphiphiles in a 0.2 M NaCl solution.¹⁶ With help of an auxiliary chemical, the L₃ “sponge” phase, as explained in chapter 1.1, was employed as template with an obtainable range of pore diameter up to 100 nm. Apart from its transparency, the major features of such a system compared to other silica / surfactant systems are the isotropic structure and the pore connectivity that makes the pore network well suitable for the transport of materials throughout the system. The phase behaviour didn't differ very much by replacing the NaCl solution by diluted hydrochloric acid (0.2 M HCl).

Nowadays, the range of suitable silica precursors in material science is very broad. Apart from common tetraalkoxysilane precursors, the use of various inorganic-organic hybrid molecules have gained various applications in the last couple of years.³⁵

A difficult step in the preparation of porous material by true liquid crystal templating is the removal of the surfactant from the solid and for wet chemical methods as sol-gel chemistry, the drying procedure of the resulted solid including the intended retaining of the materials transparency. Common methods as calcination, i.e. heat treatment (400 – 500°C), result in cracking of the material (chapter 1.3.). However, other approaches were more successful with retaining the shape and transparency of the material. Supercritical solvent extraction (SSE) yielded optical clear porous materials sufficiently robust to withstand reinfiltration by a simple solution after the drying step as well as by various

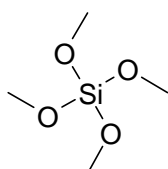
monomers.^{36, 37} The choice of the solvent plays a key role, since the use of CO₂ resulted in a severe coloration of the material but with ethanol transparent material could be obtained. The same results could be achieved by continuous Soxhlet extraction avoiding high pressures and temperatures as well as specialized equipment.³⁷ An alternative gentle method contained treatment with trimethylchlorosilane purposing an extraction of the used templating agent and crack free drying procedure by reversing the surface polarity by modification of the material with organic methyl groups.³⁸

Nanoporous silica material has found numerous fields of application in biological separation, catalysis, catalysis support and as membranes. Furthermore, authors suggested also use for optical applications.³⁶ Thus, in this work the material is considered to serve as porous host material for polymeric waveguides, made by TPP of an appropriate photocurable monomer which was infiltrated in a previous step.

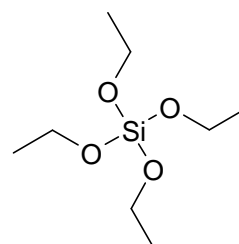
2. METHODS

2.1. Silica Sources

Tetraalkoxysilanes are a very common compound class used in sol-gel chemistry. The two types of these compounds used in this work were:



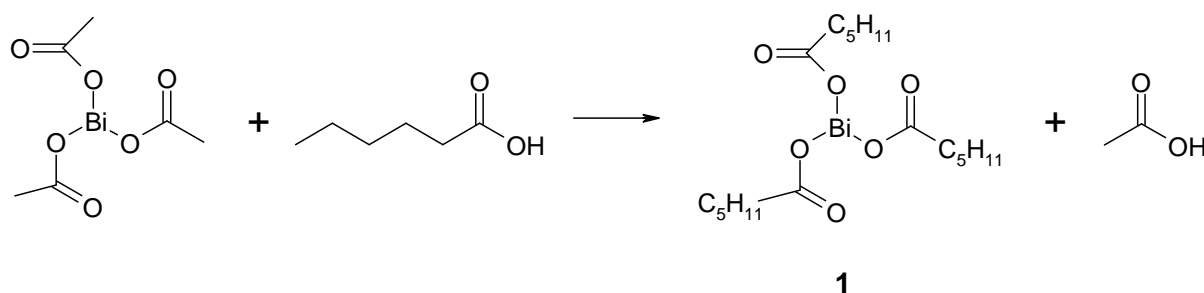
Tetramethoxysilane (TMOS)



Tetraethoxysilane (TEOS)

As solvent 0.2 M HCl was used. Hence aqueous acidic conditions were present to convert the precursors to a rigid lattice with favour to chain-like networks regarding to pH value of ~ 1 (chapter 1.2). Since, the solid silica networks derived from TMOS and TEOS are very brittle, inorganic-organic hybrid compounds were synthesised, in order to enhance the mechanical properties of the host material with flexible polyethyleneglycol (PEG) chains.

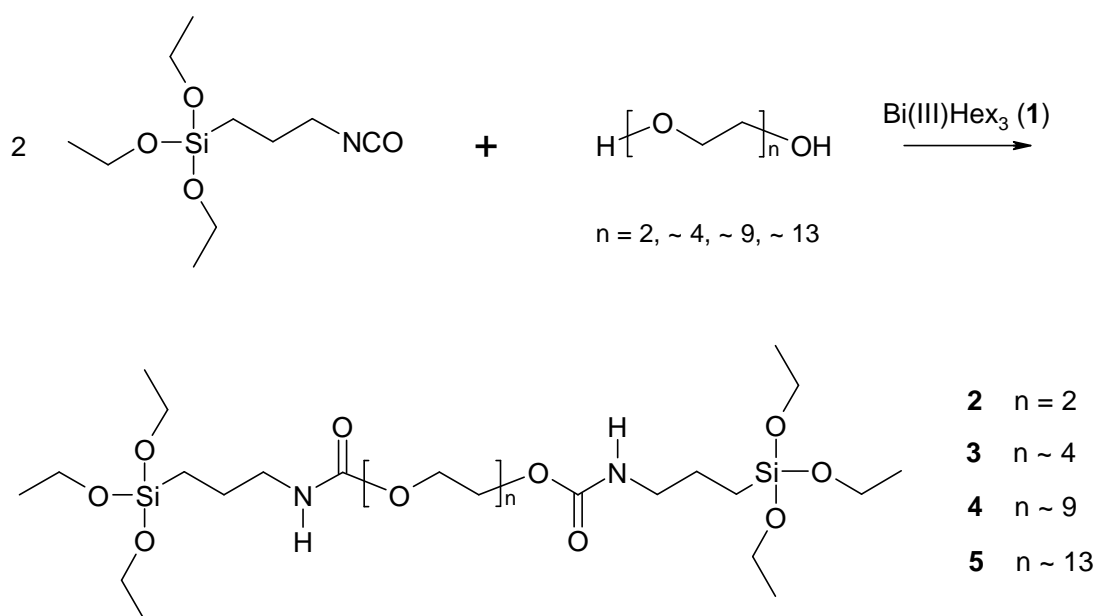
Prior to the preparation of the co-precursors, bismuth(III)hexanoate (**1**) was synthesised to act as catalyst for the subsequent $-NCO$ coupling reaction. (**1**) was obtained by a transesterification of bismuth(III)acetate and n-caproic acid:^{39, 40}



Methods

According to successful tests on the following reaction and due to a difficult purification process via recrystallisation, (1) was further used as-prepared.

Now, 4 types of co-precursors with different spacer lengths could be synthesized.⁴¹ The reaction connected two isocyanopropyltriethoxysilane (ICPTES) molecules with one molecule of the respective polyethyleneglycol via a urethane bonding to the co-precursor compound. Since trialkoxysilanes have a shorter t_{gel} than tetraalkoxysilanes, it was expected that ethoxy groups on the Si-atom would counteract that acceleration of gelation (chapter 1.2).



Polyethyleneglycols (PEG) are liquids up to a molecular weight of 600 g/mol, while compounds with higher molecular weights are solid. In general, PEG are very hydrophilic, therefore it is necessary to remove the adsorbed water prior to the conversion with the silica compound (chapter 3.1.2). Apart from diethylenglycol (DEG), all used compounds are polydispers with the average molecular weight included in the respective compound name (i.e. PEGxxx). In order to describe them more convenient, the by rounded mean of the chain length was used (tab. 2).

The coupling reaction of ICPTES with DEG and the PEG compounds, respectively, was accompanied by heat development due to exothermic effects and proceeded over night for

Methods

a full conversion. With the increasing number of ethyleneglycol units, the products appeared slightly turbid.

Table 2: Synthesized co-precursors

	compound name	spacer	average spacer length	rounded mean	\overline{M}_w , co-prec [g/mol]
2	ICPTES/DEG	Diethyleneglycol	n = 2	n = 2	600.86
3	ICPTES/PEG200	Polyethyleneglycol 200	n = 4.25	n \approx 4	694.74
4	ICPTES/PEG400	Polyethyleneglycol 400	n = 8.75	n \approx 9	894.74
5	ICPTES/PEG600	Polyethyleneglycol 600	n = 13.25	n \approx 13	1094.74

All $^1\text{H-NMR}$ measurements showed the same chemical shifts. A peak at $\delta = 3.10$ ppm occurred due to the methylene group next to the nitrogen of the urethane group. Remaining isocyanate groups would show a peak of the methylene group next to $-\text{NCO}$ at ca. $\delta = 3.30$ ppm. Depending on the average spacer length of polyethyleneglycol, the peak at 3.58 – 3.66 ppm differed in the area. This signal originates from the methylene group next to oxygens in the spacer. Urethane groups showed an ATR-IR signal at 1706 cm^{-1} . However, the signal of remaining isocyanate groups would appear ca. 2273 cm^{-1} . Hence, according to $^1\text{H-NMR}$ and ATR-IR measurements, there was no need for further purification procedures and the product could be used for sol-gel processes as-prepared. For the $^1\text{H-NMR}$ -spectrum of **5**, the peak for the methylene group on the spacer side next to the urethane group was missing. Hence the expected coupling reaction probably failed. Since the spectrum exhibited the above mentioned peak at app. 3.10 ppm, a possible reason could be that ICPTES did not react with $-\text{OH}$ groups of PEG600, but with H_2O molecules (i.e. PEG600 was not dry enough). Due to general disadvantages of this co-precursor (chapter 4.1, 4.2, 4.3), an exact origin of this fact was not tracked in more detail.

The synthesised co-precursors had two crucial properties for the further use:

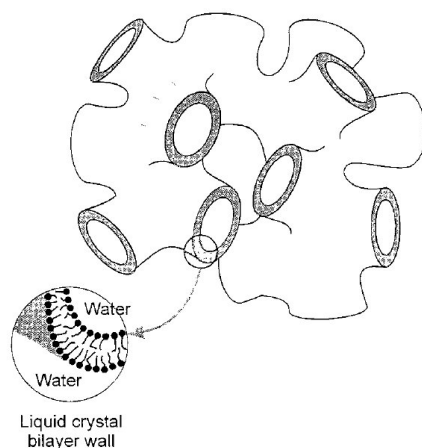
- All compounds (**2**, **3**, **4** and **5**) were fully soluble in TMOS. Thus a homogenized mixture of the co-precursor in TMOS could be prepared prior to addition to the template aqueous solution.
- All compounds were fully soluble in water. This was required for the use as silica source in aqueous solution.

2.2. Mesoporous Template

To create solids with an appropriate porosity for infiltration with monomer, the approach of true liquid crystal templating (compare to 1.1) of surfactants was chosen. A first method contained an estimation of cylindrical rods with a diameter of ca. 10 nm. Therefore, an amphiphilic block-copolymer (Pluronic[®] 123) was used in combination with n-nonane as swelling agent and mesitylen as auxiliary chemical.^{42, 43} Due to experimental difficulties in the accomplishment this method of creating a porous host material was abandoned.

Hence, a template based on the L₃ “sponge” phase was considered (chapter 1.1).^{14, 16, 18, 36, 37} Since only certain types of amphiphilic molecules conform to the requirements needed to form such a system, 1-hexadecylpyridium chloride monohydrate (CpCl·H₂O) was chosen as surfactant. In combination with an auxiliary agent (1-hexanol) and a solvent (0.2 M HCl), the L₃-sponge phase was generated, which should have the following crucial properties:

- Full transparency
- Low viscosity (comparable to water); if the viscosity appeared pretty high or turbidity was visible, the system wasn't in the L₃ phase.
- Stable over a long period of time.
- The solvent content (0.2M HCl) of the L₃-sponge phase (amount of solvent in the mixture [wt%]) should determine the pore size after the subsequent sol-gel transition based on the template.



2.3. Calculation of the Initial Weights

Considering Figure 4, an appropriate ratio of 1-hexanol to surfactant had to be chosen. For all samples prepared in this work, this ratio was fixed at 1.16, which should guarantee the formation of L₃-sponge phases. Commonly, the amounts of 1-hexadecylpyridinium chloride monohydrate ($m_s = 0.43$ g) and 1-hexanol ($m_h = 0.50$ g) were fixed. Based on this ratio and a chosen solvent content C_{solv} , the amount of solvent (0.2 M HCl) in [g] could be calculated by:

$$m_{solvent} = \frac{C_{solv} (m_s + m_h)}{1 - C_{solv}} \quad \text{eq. (2)}$$

$m_{solvent}$	amount of 0.2 M HCl [g]
C_{solv}	solvent content [wt%]
m_s	amount of surfactant [g]
m_h	amount of hexanol [g]

Regarding the constant ratio of 1.16, changes in m_s had to be considered also in m_h and vice versa. Considering Figure 4, a reasonable value for C_{solv} had to be chosen prior to the calculations. For most samples a solvent content of 75 wt% was chosen for precise investigation. Solvent contents of 85 wt% and 95 wt% were tested in order to study the difference on preparation process and the resulting structure.

For the calculation of initial weights for the precursor and used co-precursor, respectively, several assumptions had to be made:

- The choice of the molar ratio of alkoxy groups to H₂O (R_w value; tab.3). It has to be considered that the total mole number of used precursor (n_{prec}) contains silica compounds, which were used as unmodified precursors (TMOS, TEOS). Each of these molecules represented 4 alkoxy groups; therefore equation (3) contains “4” in the denominator.

Methods

Table 3: R_w values

R_w	molar ratio silica compound : H_2O
2	1 : 2
1	1 : 4
0.941	1 : 4.25

- Concerning the co-precursors structure, one molecule contained two Si-atoms. Hence, one molecule co-precursor included 6 alkoxy groups and an aliphatic chain, which connected the two Si-Atoms (Therefore, n_{Prec} had to be multiplied with $(6/4) = 1.33$).
- 0,2 M HCl contains 0.7 wt% HCl and 99.3 wt% H_2O

Now, the initial weight of the precursor compounds can be calculated by the following equations:

$$n_{Prec} = \frac{m_{solvent} \cdot 0.993}{M_{H_2O} \cdot 4} \cdot R_w \quad \text{eq. (3)}$$

n_{Prec} moles of the totally used precursor [mol]
 $m_{solvent}$ amount of 0.2 M HCl [g]
 M_{H_2O} molecular weight of water [18 g/mol]

$$m_{TMOS} = \frac{n_{Prec} \cdot C_{TMOS} \cdot M_{TMOS}}{100} \quad \text{eq. (4)}$$

m_{TMOS} amount of tetramethoxysilane[g]
 C_{TMOS} content of tetramethoxysilane in the precursor mixture [mol%]
 M_{TMOS} molecular weight of tetramethoxysilane [152.22 g/mol]

Methods

$$m_{CoPrec} = \frac{n_{Prec} \cdot C_{CoPrec} \cdot 1.33 \cdot M_{CoPrec}}{2 \cdot 100} \quad \text{eq. (5)}$$

m_{CoPrec}	amount of co-precursor [g]
C_{CoPrec}	content of co-precursor in the precursor mixture [mol%]
M_{CoPrec}	molecular weight of co-precursor [g/mol]

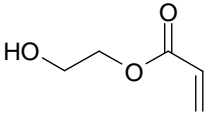
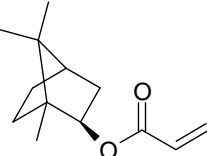
Note that the sum the contents of TMOS and cp-precursor denotes the total content of precursor:

$$100 = C_{TMOS} + C_{CoPrec}$$

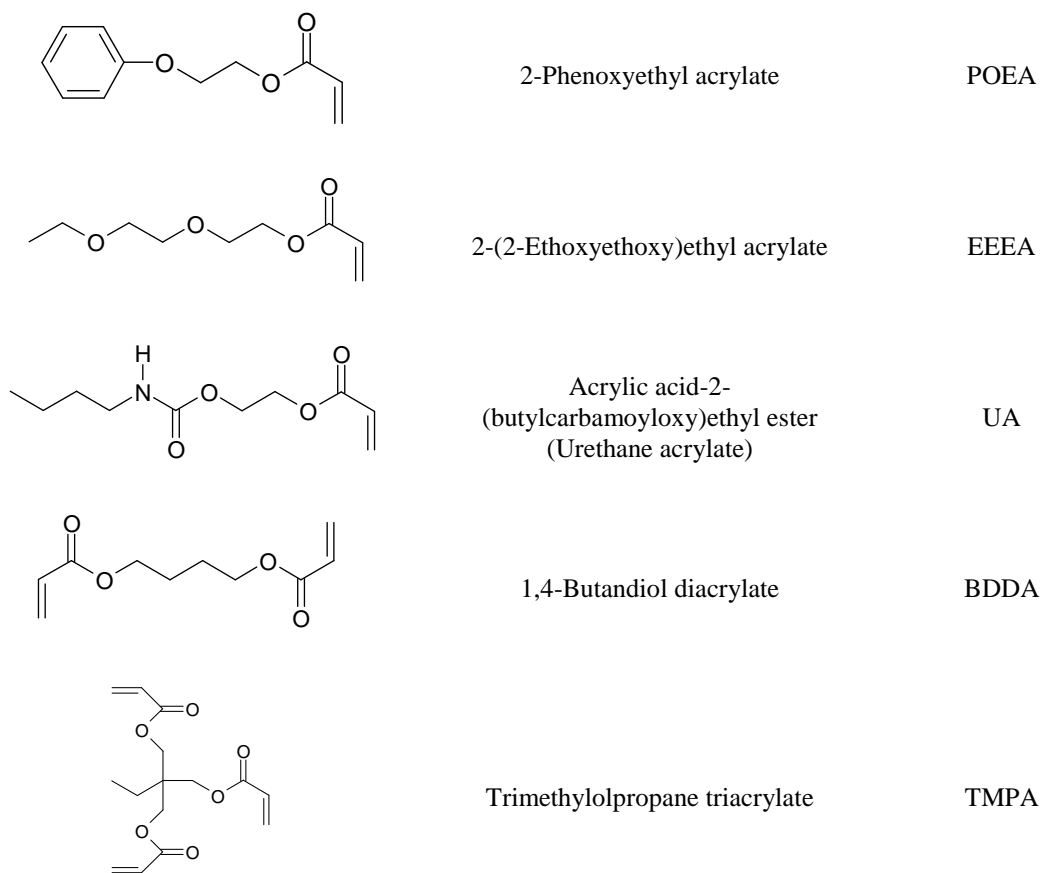
2.4. Monomers

To generate waveguides in the host material, appropriate monomers had to be infiltrated in the mesoporous solid. Due to the requirement of a big difference in the refractive index between carrier material and monomer, and concerning their ability for photocuring, tests on several monomers were performed. All of them are acrylates with one, two or three acryl groups per molecule with the ability for radical polymerisation and chosen regarding aspects as high refractive index, low volatility, reactivity or degree of cross-linking. Hence, the following acrylate-compounds were tested in the course of this work (tab. 4):

Table 4: Tested monomers for the infiltration

structure	name	abbreviation
	2-Hydroxyethyl acrylate	HEA
	Isobornyl acrylate	IBOA

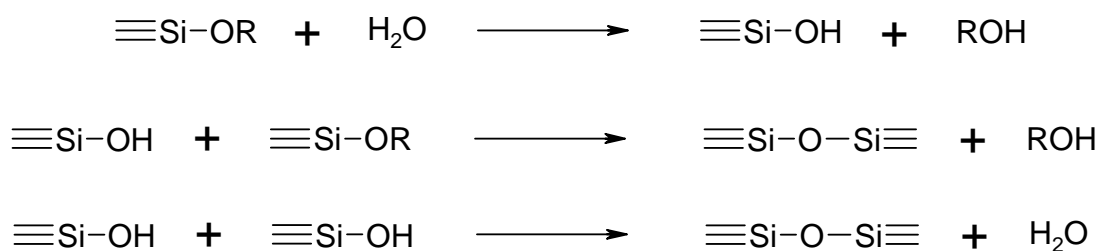
Methods



All monomers were fully soluble in ethanol, which is necessary both to infiltrate them as mixture and to remove the remaining monomer subsequent to photocuring.

2.5. Preparation of the Carrier Material

2.5.1. Sol-Gel Transition



Based on the L₃-sponge phase, the precursor or precursor mixture was added to prepare a colloidal solution (Sol). The gel time (t_{gel}) was reached, when the vessel could be turned upside down without any movements of the interior. The obtained wet gels retained the shape of the hardening vessel and began to shrink after several days during the aging procedure. The transparency of the samples decreased both with increasing PEG spacer length of the co-precursor and their increasing content in the sol. Independent of the type of precursor mixture, the gels were allowed to stand for 3 days.

Accordingly, the preparation of both monolithic forms and thin films (thickness: 80 – 200 μm) was possible, only depending on the type of the vessel. Monolithic samples with the following sizes were synthesized:

- Diameter: 3.5 cm, 2.25 cm
- Height: 5 mm, 3 mm

2.5.2. Solvent Exchange

Three days after the start of preparation, the gelled samples were treated with successive solvent exchanges, both in order to remove parts of the surfactant from the solids and to prepare them for the following extraction process. Since the pore liquid had been aqueous until this point of the process, the solvent exchange was carried out stepwise with the following solvents:

- EtOH : H₂O 50wt% : 50wt%
- EtOH : H₂O 75wt% : 25wt%
- pure EtOH (2 times)

The samples were covered with the according solvent mixture in its vessel to a solvent height of app. 3 - 5 mm above the sample surface (ca. 1.5 g solvent was necessary), sealed again and allowed to stand for 1 day until the next exchange step was carried out. Finally, samples covered with pure ethanol were ready for the following extraction step.

The used solvent was recollected and vaporized by a rotary evaporator until the surfactant precipitated from the solvent. Since $\text{CpCl}\cdot\text{H}_2\text{O}$ is fully soluble in ethanol substantial parts of the template were removed just by the solvent exchange. $^1\text{H-NMR}$ measurements confirmed that the precipitate was the used surfactant (compare with chapter 4.3.3).

2.5.3. Extraction of the Template

Continuous Soxhlet extraction was chosen, to be applied on monolithic samples on the one hand to remove the remaining parts of the template and on the other hand to avoid, microscopic cracking that would appear without extraction in monolithic carrier material during the subsequent infiltration step.

The samples were cushioned in layers of glasswool. In this manner, three samples could be positioned in one extractor, divided from each other by a layer of glasswool. The samples had to be kept in ethanol, and the time for the transfer from the vessel in the extractor had to be as short as possible, in order to avoid macroscopic cracks that may occur during vaporisation of the solvent.

2.6. Generating Waveguides

2.6.1. Infiltration with Monomer

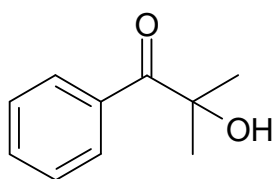
After solvent exchange (thin films) and Soxhlet extraction (monoliths), respectively, the samples could be infiltrated with an appropriate monomer (tab.4). Resembling to the solvent exchange the infiltration was carried out stepwise with mixtures of monomer with ethanol, since the viscosity of the monomer decreased in the mixtures. Thus, the infiltration was supposed to be more effective:

- Monomer : EtOH 50wt% : 50wt%
- Monomer : EtOH 75wt% : 25wt%
- pure monomer

Methods

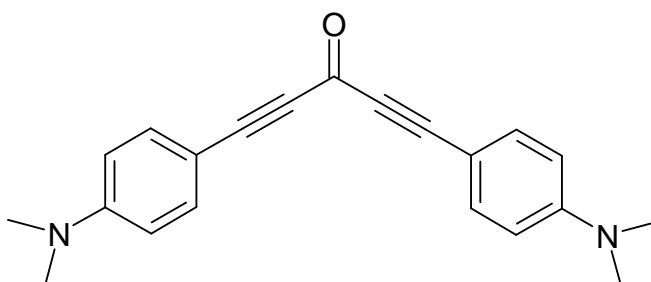
The samples were covered with the respective mixture in their glassy vessel, again to a mixture height of app. 3 - 5 mm above the sample surface (ca. 1.5 g solvent was necessary). Afterwards, the vessel was tightly sealed until the next exchange step was carried out.

For the second and third infiltration step, photoinitiator was added. Therefore, exposure to daylight should be avoided from this state on, in order to prevent curing. The used photoinitiators and their amount regarding the initial weights of monomer are:



- Darocur[®] 1173; 2 wt%, based on monomer:

This PI was used, in order to check the application of the respective monomer. To cure the monomer, the sample was kept under argon and exposed to UV-Light for 30 min. Parts of the sample were covered with an aluminium foil to achieve partial polymerisation.



- 1,5-Bis[4-N,N-(dimethylamino)phenyl]penta-1,4-dien-3-on (NDPD); 0.05 wt%, based on monomer

This PI was used for two photon polymerisation (TPP) application.⁴⁴

Uncured monomer had to be removed after the curing procedure:

- The sample was rinsed with ethanol, in order to dissolve the remaining monomer. Cured monomer is insoluble in ethanol, thus those regions were not affected by this process. While the approach was applicable for thin films, monolithic samples got microscopic cracks during this process.
- In order to stabilize the monolith, a second monomer with much lower refractive index as compared to the waveguide monomer, could be infiltrated with the same procedure like the first monomer and cured with Darocur[®] 1173. This step was not carried out for TPP-structured waveguide samples.

2.6.2. Two Photon Polymerisation

The infiltrated samples were structured by TPP to generate waveguides. This work was accomplished at the Joanneum Research Institute in Weiz.

Test were carried out to determine the ability for full infiltration of monomer in the carrier material as well as to find out the optimal laser power and structuring speed, respectively. Since thin films are stable even without a liquid in the pores, they were covered with ethanol over night in the tightly sealed vessel. Thus, big parts of the uncured monomer should be dissolved. However, monolithic samples could not be treated with alcohol, because the samples cracked when the monomer was dissolved (Obviously, this type of samples needed a pore liquid as scaffold). Therefore, monoliths were investigated subsequently, with the monomer remaining in the pores.

2.7. Determination of Thermal Properties

2.7.1. Thermogravimetric Analysis

Thermogravimetric analysis (TGA) was applied for the following reasons:

- Thermal behaviour of the various co-precursors
- Determination of the amount of infiltrated monomer. This correlated with the porosity of the material

Methods

In TGA, the mass of the sample in a controlled atmosphere was recorded continuously as a function of temperature or time as the temperature of the sample was increased linearly with the time.⁴⁵ A plot of mass or mass percent as a function of temperature is called a thermogram or a thermal decomposition curve. A typical instrument for thermogravimetry consists of a sensitive analytical balance, a furnace, a purge gas system for providing an inert gas atmosphere and a computer for instrument control and data acquisition and display, respectively. The mass change was detected by an analytical balance with the sample holder housed in the furnace, to guarantee thermal isolation. This furnace, equipped with a probe to record the temperature, should provide appropriate heating and cooling rates. Nitrogen was used to purge the furnace.

For a measurement, the following required inputs were chosen (tab. 5):

Table 5: Required inputs for TGA

Input	Value
Heating rate	10 °C/min
Max. Temperature	800 °C
Nitrogen flow rate	5 - 7 ml/s

For measurements of the carrier material, a sample piece of app. 20 ± 5 mg was placed in the platinum sample holder.

Regarding the uncertainty of the measurement for these carrier material samples, the following point had to be considered (apart from the systematic error of the device, which could be neglected):

Prior to the measurement, the samples were stored in the respective monomer, in order to avoid cracking, which could occur even for infiltrated samples. The monomer was carefully removed from the selected sample piece, in order to guarantee no remaining substance on the sample surface. Thus, only the monomer located in the sample pores vaporized during the TGA measurement. Tests concerning the reproducibility of the measurements resulted in an error of ca. 5 %, obviously due to some remaining monomer on the sample surface.

2.7.2. Differential Scanning Calorimetry

Concomitant to TGA measurements, differential scanning calorimetry (DSC)⁴⁵ measurements could assign the appearing mass losses to certain types of transition. In DSC, differences in the heat flow into a substance and a reference were measured as a function of sample temperature. For this work, heat flux DSC was employed with the sample pan and the reference pan and a thermoelectric disk. Thermocouple junctions under the sample pans monitored the differential heat flow through the two pans on a computer screen. Nitrogen was purged through the system to guarantee an inert atmosphere. The required inputs for the measurements were (tab. 6):

Table 6: Required inputs for DSC

Input	Value
Heating rate	10 °C/min
Max. Temperature	500 °C

2.8. Determination of Mechanical Properties

Since only small pieces of sample were available for investigation, nano indentation (NI) was chosen to determine the mechanical properties.⁴⁶ According to this approach, the following materials parameter could be derived from the force/indentation depth data set:

- Indentation modulus (E_{IT})
- Indentation hardness (H_{IT})
- Plastic and elastic parts of the deformation work (W_{plast} , W_{elast})

Sample Preparation:

The sample pieces (10 – 30 mm²) were fixed on the sample holder by an epoxy resin mixed with hardener and a thixotropic agent.

Procedure:

For the test, the procedure was displacement controlled using the progressing indentation of a diamond pyramid with triangular base (Berkovich pyramid) to the default setting of

Methods

maximum displacement (indentation depth) of $1000 \text{ nm} \equiv 1 \text{ }\mu\text{m}$ in the sample. The test force, the corresponding indentation depth and time were recorded during the whole test procedure. As result of the test, a set of data for the test force and the relevant indentation depth as a function of time was obtained (fig. 9). Since the indentation tool must have higher hardness than the test piece, a diamond indenter was used.

After the indentation process, a permanent cast of the indenter with the depth h_p (depended on η_{IT} ; compare to chapter 2.8.3) remained in the material.

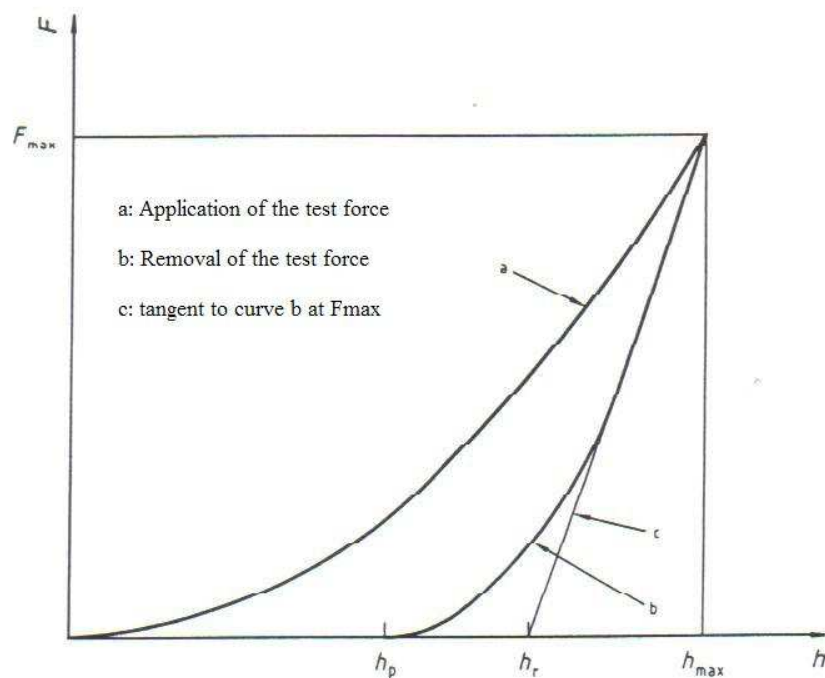


Figure 9: Test force vs. Indentation depth

Note that the temperature should be constant and the relative humidity should not exceed 50 %. In general, measured values were only comparable if they had the same conditions during the measurements. Deviations led to systematic uncertainties in the results. Further sources for uncertainties are listed in.⁴⁶ For all measurements the following required inputs were chosen (tab. 7):

Methods

Table 7: Required inputs for NI

Input	Value
Percent to unload	100%
Surface approach	10 nm/s
Δx for finding surface	0 μm
Δy for finding surface	-50 μm
Maximum depth (h_{max})	1000 nm
Load rate multiple for unload rate	1
Allowable drift rate	0.05 nm/s
Approach distance to store	1000 nm
Peak hold time	30 s
Time to load	20 s
Surface approach distance	8000 nm
Surface approach sensitivity	25%
Poisson's ratio (ν_s)	0.2

2.8.1. Indentation Hardness (H_{IT})

Indentation hardness is a measure of the resistance against permanent deformation or damage by a second, harder material. It is defined as the maximum test force, divided by the projected (cross-sectional) contact area of the indenter with the test piece:

$$H_{IT} = \frac{F_{max}}{A_p} \quad \text{eq. (6)}$$

H_{IT}	Indentation hardness [GPa]
F_{max}	Maximum test force [N]
A_p	Projected area of contact of the indenter at distance h_c from the tip [mm^2]

Indentation hardness was given in [N/mm^2] or [GPa] (1 GPa \equiv 1000 MPa \equiv 1000 N/mm^2). Note that for indentation depths $< 6 \mu\text{m}$, the area function of the indenter is not equal to that of the theoretical shape, since all indenters have some degree of rounding at the tip. For a Berkovich indenter, the projected contact area is given by:

$$A_p = 23.96 \cdot h_c \quad \text{eq. (7)}$$

$$h_c = h_{max} - \varepsilon(h_{max} - h_r) \quad \text{eq. (8)}$$

h_c	Depth of the contact of the indenter with the test piece at F_{max} [mm]
ε	Correction factor
h_r	Point of intersection of the tangent c to curve b at F_{max} with the indentation depth-axis [mm]

The contact depth was derived from the force removal curve using the tangent depth and the maximum displacement correcting for elastic displacement of the surface. The correction factor depended on the indenter geometry (For a Berkovich pyramid: $\varepsilon = 3/4$).⁴⁶

In order to compare the indentation hardness with results in the literature, hardness values (H_{IT}) were correlated to Vickers hardness (HV). Note that no direct conversion can be made due to different size and shape of the indenter and therefore resulting different deformation behaviour. Usually the following conversion factor is used:

$$HV = \frac{H_{IT} \cdot A_p}{g_n \cdot A_s} = 0.0924 \cdot H_{IT} \quad \text{eq. (9)}$$

A_p	Projected area of contact of the indenter at distance h_c from the tip [mm ²]
A_s	Surface area of the indenter at distance h_c from the tip [mm ²]
g_n	acceleration due to gravity [9.80665 m/s ²]

2.8.2. Indentation Modulus (E_{IT})

The indentation modulus could be calculated from the slope of the tangent from the unloading part of the force-displacement curve. E_{IT} is usually in the range of the Young's modulus of the material. Significant differences between the indentation modulus and

Young's modulus may occur, however, if either pile-ups or sink-ins are present or if the material is very anisotropic.

$$E_{IT} = \frac{1 - (v_s)^2}{\frac{1}{E_r} - \frac{1 - (v_i)^2}{E_i}} \quad \text{eq. (10)}$$

E_{IT}	Indentation modulus [N/mm ²]
v_s	Poisson's ratio of the test piece
v_i	Poisson's ratio of the indenter (for diamond 0.07)
E_r	Reduced modulus of the indentation contact [N/mm ²]
E_i	Modulus of the indenter (for diamond $1.14 \cdot 10^6$)[N/mm ²]

$$E_r = \frac{\sqrt{\pi}}{2C\sqrt{A_p}} \quad \text{eq. (11)}$$

Indentation modulus is given in [N/mm²] or [GPa] (1 GPa \equiv 1000 MPa \equiv 1000 N/mm²)

2.8.3. Plastic and Elastic Parts of the Indentation Work

The mechanical work W_{total} indicated during the indentation procedure is only partly consumed as plastic deformation work W_{plast} . During the removal of the test force, the remaining part was set free as work of the elastic reverse deformation W_{elast} . Since the mechanical work is defined as the area between the function resulting from the application of the test force and the x-axis, both W_{plast} and W_{elast} appeared as different part of this area.

$$W_{total} = W_{elast} + W_{plast} \quad \text{eq. (12)}$$

The elastic part is expressed by the following relation.

$$\eta_{IT} = \frac{W_{elast}}{W_{total}} \cdot 100 \quad \text{eq. (13)}$$

η_{IT}	Relation W_{plast}/W_{total} [N/mm ²]
W_{plast}	Elastic reverse deformation work of indentation [N·m]
W_{total}	Total mechanical work of indentation [N·m]

Hence, the plastic part is given by:

$$100 \% - \eta_{IT} = \frac{W_{plast}}{W_{total}} \cdot 100 \quad \text{eq. (14)}$$

2.9. Structural Properties

2.9.1. Scanning Electron Microscopy

In order to obtain first structural informations of fracturing areas and surface areas of the samples, scanning electron microscopy was carried out. In general, the device consisted of the following components: ⁴⁷

- An electric gun, with a heated tungsten filament as cathode and an anode maintained at an adjustable potential (For this work 20 kV), produced high energetic electrons. The Wehnelt cylinder between the two electrodes modified the electric field, in order to focus the emitted electrons in one point below the anode.
- The produced electronic beam passes by several electronic lenses with magnetic fields to adjust the intensity of the electronic beam and to focus or defocus it. Additional, deflection coils enabled a scanning of the beam on the sample surface.
- A moveable and revolving sample holder was located in a sample chamber, which could be evacuated to a pressure of app. 10^{-5} bar. The samples were arranged circular near the edge of the sample holder.
- By scanning the high energetic beam of electrons over the sample, several types of signals were produced from the surface: backscattered, secondary and Auger

electrons; X-ray fluorescence. Backscattered and secondary electrons are used to depict an image of the sample, in order to get morphologic and topographic information about the surface. It produced images of high resolution, examining also closely spaced features on the surface.

Depending on the surface morphology, secondary electron images varied in its brightness (intensity), whereas backscattered electrons vary the intensity regarding to the atomic number of the various atoms.

Small pieces of the samples were fixed on the sample holder, covered with an aluminium foil, with conductive silver glue. Since the samples were isolators, it was necessary to coat the surfaces with a thin conductive gold film by vapour deposition. Now the sample chamber could be loaded with the sample holder. To carry out measurements, the sample chamber was evacuated to a pressure of app. 10^{-5} bar.

The maximum resolution of the device to obtain reasonable surface images was $\times 15000$, i.e. it was not possible to register mesopores. Using a higher resolution made the images blurry and not usable, obviously suffering on the restricted sample conductivity (Although they are covered with a gold film).

2.9.2. Atomic Force Microscopy

Atomic force microscopy (AFM) is a powerful tool for nano scale analytics both to image the sample surface and to obtain various spectroscopic data.⁴⁷ The aim of this approach for the work was to gain complementary informations to SEM images regarding surface topology and porosity of the samples.

The approach included a soft microscale cantilever equipped with a sharp tip at its end (Figure 10) that was used to raster the specimen surface by the help of a piezoelectric scanner. Interactions between tip and sample led to a deflection of the cantilever. The vertical displacement of the cantilever was measured by focusing a laser spot onto the back of the cantilever and detecting the position of the reflected beam with a photodiode. Two common modes were applied in this work:

Methods

- Contact mode (constant force). The tip was in contact with the sample surface permanently. As the tip rasters across the surface with constant force, it was vertically deflected regarding the samples topology by repulsion forces. An image could be generated by this deflection and the resulted bending of the cantilever. Since, the tip dragged across the surface, this mode could cause damages at the surfaces.
- Intermittent contact (“tapping”) mode. The cantilever was driven to oscillate up and down near to its resonance frequency by a small piezoelectric crystal. Due to the various interactions acting on the cantilever, when the tip came close to the surface, the oscillation decreased or increased according to the samples topology. During the operation a feedback loop adjusted the tip-sample separation, in order to maintain the oscillation amplitude and force constant. Hence an image could be obtained. Additionally, informations could be obtained by the phase displacement between the phase signals of input and cantilever-output. The “tapping” mode achieved a better resolution as the contact mode.

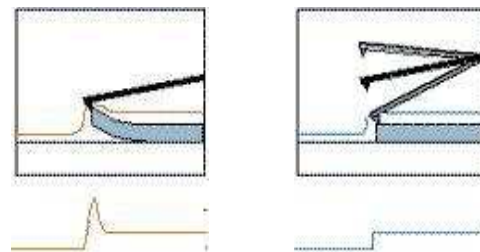
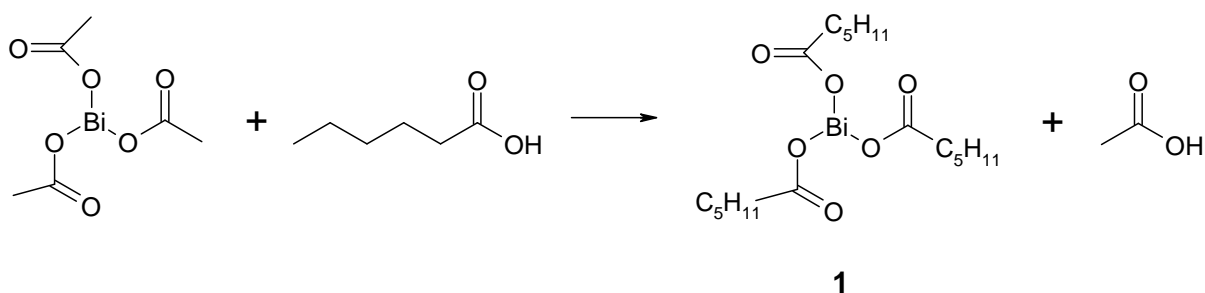


Figure 10: left image: contact mode; right image: “tapping” mode

3. EXPERIMENTAL

3.1. Synthesis of the Co-Precursor Compounds

3.1.1. Synthesis of Bismuth(III)hexanoate



Chemicals:

1.926 g	(5 mmol)	Bismuth(III)acetate
1.925 g	(16.5 mmol)	n-Caproic acid
220 ml		Toluene dry

Synthesis:^{39, 40}

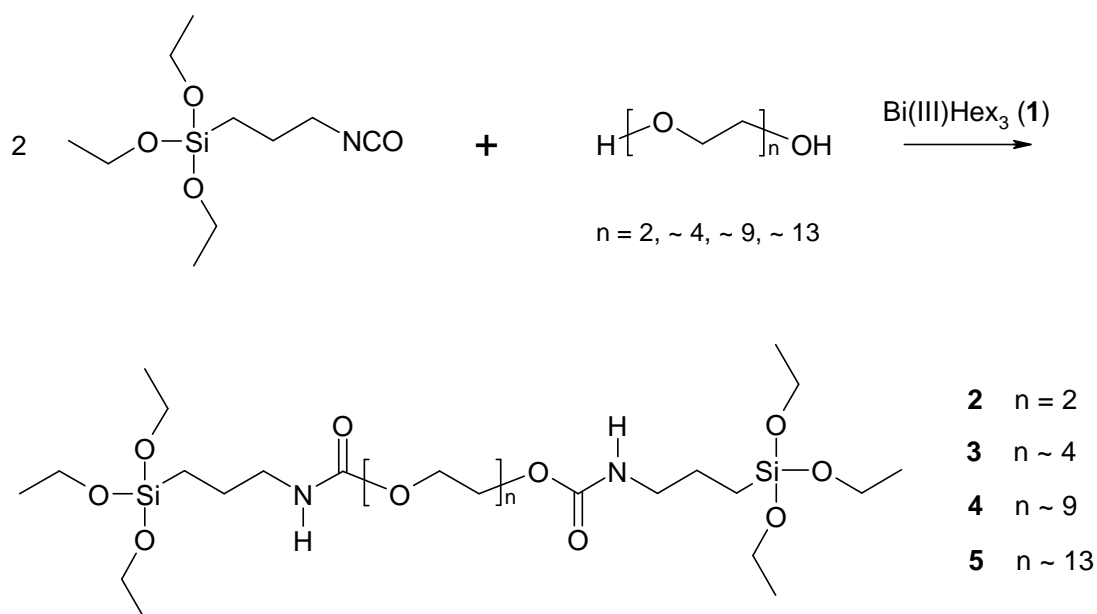
Bismuth(III)acetate and n-caproic acid (10% excess) were dissolved in 110 ml of dry toluene in a 250 ml 3-neck flask and purged with argon. Subsequently, the mixture, equipped with a magnetic stirrer and reflux condenser, was heated up to 125°C and refluxed for app. 3 h. Afterwards, the reflux cooler was replaced by a distillation bridge, in order to remove the azeotropic mixture of acetic acid and toluene (28:72 wt%; bp: 105.4°C acc. to lit.) over a period of 4 h. The distillation was repeated by refilling the flask with 110 ml dry toluene. Finally, the resulting oily liquid was first kept at 40°C and 0,03 mbar for 1 h (a white solid appeared) and then slowly heated up to 140°C at the same pressure, to get rid of the remaining n-caproic acid, which did not react. The white solid turned again to an oily liquid, until finally a brown solid appeared, caused by the cooling to ambient temperatures at atmospheric pressure.

Experimental

Analytics:

- 1** $^1\text{H-NMR}$: (CDCl_3) δ [ppm]: 2.40 – 2.31 (t, 2H, -CO-CH₂-)
1.69 – 1.65 (m, 2H, -CO-CH₂-CH₂-)
1.40 – 1.33 (m, 4H, -CH₂-)
1.00 – 0.91 (m, 3H, -CH₃)

3.1.2. Synthesis of Co-Precursors with different PEG chain lengths



Chemicals:

12.369 g	(50 mmol)	Isocyanopropyltriethoxysilane
2 2.653 g	(25 mmol)	Diethyleneglycol
3 5.002 g	(25 mmol)	Polyethyleneglycol 200
4 10.000 g	(25 mmol)	Polyethyleneglycol 400
5 15.000 g	(25 mmol)	Polyethyleneglycol 600
6.25 ml		Chloroform dry
0.2 ml		0.5 M 1 in Chlorobenzene

Experimental

Preliminaries:

Drying procedure of Polyethyleneglycols:

- Diethyleneglycol was dried via distillation at 108°C – 113 °C and 2 mbar.
- Due to the high boiling points of PEG 200 – 600 (> 300°C), the drying procedure was carried out via addition of 4 Å molecular sieves and stirring for 24 h.

The water contents of the various PEG compounds according to Karl-Fischer-Titration are shown in tab. 8. Since PEG 600 was a solid, a determination of the water content wasn't possible.

To avoid adsorption of moisture, the Polyethyleneglycols were kept under argon.

Table 8: Water content of used polyethyleneglycol compounds

	number of measurements	water content [ppm]
PEG 200	2	68,7
PEG 400	3	39,7
PEG 600	no measurement possible	

*Synthesis:*⁴¹

First of all, a 100 ml flask was silanized by treatment with some ml of dichlorodimethylsilane, which subsequently was removed from the flask by purging it twice with dry diethylether. Afterwards, the silanized equipment was placed in a drying oven for at least 1 h at 70°C.

The as-prepared flask, equipped with a magnetic bar, was filled with the respective polyethyleneglycol compound and isocyanopropyltriethoxysilane. After a short period of stirring, in order to obtain a homogeneous emulsion of the educts, dry chloroform was added, which resulted in a full solubility of the two compounds. To prevent subsequent hydrolysis of the product, the flask was purged with argon. To start the reaction, **1** was added, accompanied by a strong heat development regarding exothermic effects. Due to the polyethyleneglycol compound, the products became slightly turbid, whereas the degree of translucence increased with the increasing length of spacer. To guarantee full conversion, the reaction proceeded over night for app. 15 h. ¹H-NMR and ATR-IR measurements showed a full conversion and no remaining isocyanate groups.

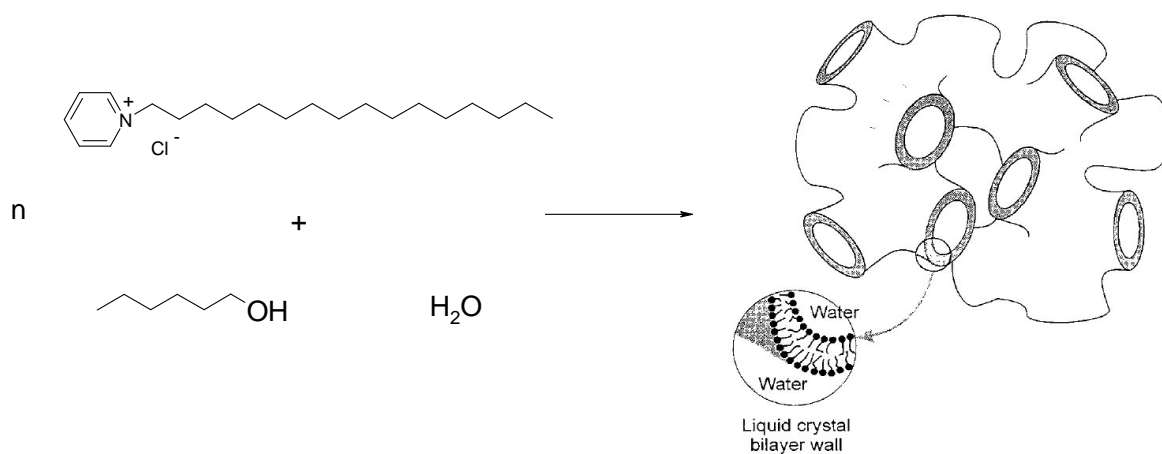
Experimental

Analytics:

$^1\text{H-NMR}$: (CDCl_3) δ [ppm]: 4.22 – 4.14 (t, $-\text{CO-O-CH}_2\text{-CH}_2\text{-O-}$)
3.81 – 3.72 (m, 12H, $\text{CH}_3\text{-CH}_2\text{-O-Si}\equiv$)
3.66 – 3.58 ($-\text{CO-O-CH}_2\text{-CH}_2\text{-O-}$)
3.17 – 3.07 (s, 4H; 12,2H; 30H; 50H; $-\text{CH}_2\text{-NH-}$)
1.68 – 1.50 (m, 4H, $\equiv\text{Si-CH}_2\text{-CH}_2\text{-}$)
1.24 – 1.14 (t, 18H, $\text{CH}_3\text{-CH}_2\text{-O-}$)
0.65 – 0.55 (t, 4H, $\equiv\text{Si-CH}_2\text{-}$)

IR (cm^{-1}): 3344, 2978, 2933, 2890, 1706, 1527, 1445, 1392, 1245, 1195, 1166, 1102, 1075, 955, 862, 753

3.2. Generation of the L_3 “Sponge” Phase Template



Chemicals:

For a L_3 “sponge” phase template needed in further use, the following formulation was necessary:

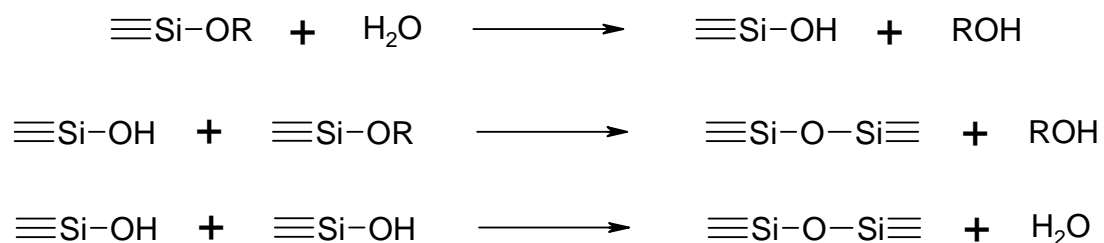
0.430 g	(1.33 mmol)	$\text{CpCl}\cdot\text{H}_2\text{O}$
0.500 g	(4.90 mmol)	1-Hexanol
2.790 g	0.2 M HCl	

Experimental

*Synthesis:*¹⁴

The surfactant 1-hexadecylpyridinium chloride monohydrate (CpCl·H₂O) and 1-hexanol were placed in a penicillin flask, equipped with a magnetic bar. After 2 min stirring in the closed flask, 0.2 M HCl was added via a syringe followed by a period of agitation. The appearance of the solution should turn from turbid to completely clear within a few minutes, resulting from a transformation of the lamellar to the L₃ “sponge” phase. If the solution retained its original state longer than 30 min, a few mg of either CpCl·H₂O or 1-hexanol, depending on which compound had an excess, could be added to achieve the phase transformation. Finally, a stable solution was established, which hardly was distinguishable from water. Samples which did not clear within 30 min were discarded.

3.3. Preparation of the Carrier Material



Chemicals:

L₃ “sponge” phase template (amount: acc. to 3.2)

TMOS

Co-Precursor (**2, 3, 4, 5**)

EtOH

Monomer (acc. to 2.4)

Photoinitiator (NDPD; Darocur[®] 1173)

Tab. 10, 11 and 12 show the initial weights of tetramethoxysilane (TMOS) and co-precursor, calculated by equations (2-5) as well as the designations of the samples, used

Experimental

in this work. To downscale the amounts of precursors, the calculations had to be carried out with lower initial weights of CpCl-H₂O and 1-hexanol, respectively. The solvent content C_{solv} describes the amount of 0.2M HCl in the template, and R_w determines the molar ratio of alkoxy groups of the precursors to H₂O (chapter 2.3).

Table 9: Initial precursor weights for the sol-gel process; $C_{\text{solv}} = 75$ wt%; $R_w = 0.941$

sample	TMOS cont. [wt%]	co-precursor	spacer of co-precursor	co-precursor cont. [wt%]	m_{TMOS} [g]	m_{CoPrec} [g]
A	100		---	---	5.513	---
B1	95		DEG	5	5.237	0.723
B2	90	2	DEG	10	4.961	1.447
B3	80		DEG	20	4.441	2.894
C1	95		PEG200	5	5.237	0.837
C2	90	3	PEG200	10	4.961	1.673
C3	80		PEG200	20	4.441	3.346
D1	95		PEG400	5	5.237	1.077
D2	90	4	PEG400	10	4.961	2.155
D3	80		PEG400	20	4.441	4.310
E1	95		PEG600	5	5.237	1.318
E2	90	5	PEG600	10	4.961	2.636
E3	80		PEG600	20	4.441	5.273

Table 10: Initial precursor weights for the sol-gel process; $C_{\text{solv}} = 85$ wt%; $R_w = 0.941$

sample	TMOS cont. [wt%]	co-precursor	spacer of co-precursor	co-precursor cont. [wt%]	m_{TMOS} [g]	m_{CoPrec} [g]
A ($C_{\text{Solv}}=85\%$)	100		---	---	10.413	---
D3 ($C_{\text{Solv}}=85\%$)	80	4	PEG400	20	8.330	8.140

Table 11: Initial precursor weights for the sol-gel process; $C_{\text{solv}} = 95$ wt%; $R_w = 0.941$

sample	TMOS cont. [wt%]	co-precursor	spacer of co-precursor	co-precursor cont. [wt%]	m_{TMOS} [g]	m_{CoPrec} [g]
A ($C_{\text{Solv}}=95\%$)	100		---	---	34.941	---
D3 ($C_{\text{Solv}}=95\%$)	80	4	PEG400	20	27.931	27.294

Table 12: Initial precursor weights for the sol-gel process; $C_{\text{solv}} = 75$ wt%; $R_w = 2$

sample	TMOS cont. [wt%]	co-precursor	spacer of co-precursor	co-precursor cont. [wt%]	m_{TMOS} [g]	m_{CoPrec} [g]
A ($R_w=2$)	100		---	---	11.714	---
D3 ($R_w=2$)	80	4	PEG400	20	9.376	9.158

Experimental

Synthesis:

Prior to the reaction, the co-precursor was dissolved in TMOS until a homogenous mixture was formed. The solution was now added via a syringe to the template, in order to silicify it. Due to the exothermic hydrolysis of the reaction, a water bath was provided to avoid high temperatures and the addition was carried out dropwise. All the samples turned slightly turbid, caused by the development of methanol bubbles during hydrolysis, but after further addition it became clear again. An exception was the mixture with compound **5**, which retained its cloudiness even after full conversion and homogenization.

After the addition, the mixture was slightly stirred for a short time (est. 30 s – 1 min), both to get rid of the occurring bubbles and to cool it down to ambient temperatures. Subsequently, the prepared sol could be transferred into appropriate vessels, which were tightly sealed. Depending on the type of the co-precursor and its content in the silica source, the gel time varied between several days (**A**) and only a few minutes (**D3**, **E3**, **D3**($C_{\text{Solv}}=85\%$), **D3**($C_{\text{Solv}}=95\%$), **D3**($R_w=2$)).

After an aging time of 92 h (3 days), the solvent exchange from the water to ethanol was carried out. Therefore, the solid was covered with solvent mixtures in the following steps with a treatment time of 1 day in the sealed vessel for each mixture: 1.) EtOH : H₂O 50wt% : 50wt%; 2.) EtOH : H₂O 75wt% : 25wt%; 3.) EtOH; (optional 4.) pure EtOH). After treatment, the solvent was carefully removed by a Pasteur pipette. Note that the samples were never allowed to dry during the various exchange steps.

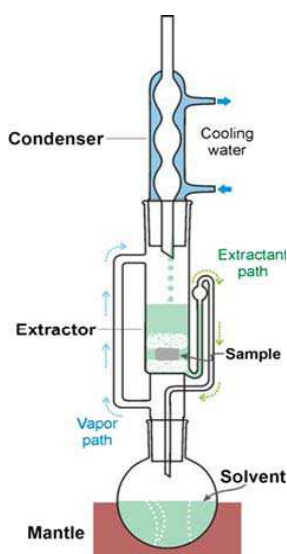


Figure 11: Soxhlet extractor

Now, thin films were ready to be infiltrated with an appropriate monomer. However, monolithic samples were additionally treated by continuous Soxhlet extraction (Figure 11).

The extractor was equipped with a reflux cooler, a 500 ml flask, half filled with the extracting solvent EtOH and a magnetic stirrer. The solvent was heated up until a continuous stream of hot solvent throughout the apparatus occurred. In such a manner, the extraction procedure retained for 3 days,

Experimental

in order to remove as much template as possible. After the extraction, the samples were transferred to glassy vessels, in order to accomplish the following infiltration with monomer. Vessels made of polystyrene would be etched by in some of the monomers. Note that the samples were immediately covered with the first monomer mixture and tightly sealed, in order to avoid cracking of the material due to vaporisation of EtOH.

Infiltration with monomer resembled to the procedure of the solvent exchange. Each of the three monomer mixtures was allowed to stand for 1 day in the tightly sealed vessel. For the second and third step, a certain amount of photoinitiator, based on the monomer amount, was added (2 wt% Darocur[®] 1173 for test purposes, 0.05 wt% NDPD for two photon polymerisation (TPP) application).

1.) monomer : EtOH 50wt% : 50wt%; 2.) monomer : EtOH 75wt% : 25wt%; 3.) pure monomer

4. RESULTS

The letters in the sample names are designated according to the used type of precursor (compare also to tab 10 – tab. 12):

- **A**: no co-precursor (100 wt% TMOS)
- **Bx**: ICPTES/DEG (**2**)
- **Cx**: ICPTES/PEG200 (**3**)
- **Dx**: ICPTES/PEG400 (**4**)
- **Ex**: ICPTES/PEG600 (**5**)

The numbers in the sample names refer to the content of precursor and co-precursor, respectively:

- **x = 1**: 95 wt% TMOS; 5 wt% co-precursor
- **x = 2**: 90 wt% TMOS; 10 wt% co-precursor
- **x = 3**: 80 wt% TMOS; 20 wt% co-precursor

Sample names without index represent a solvent content (C_{Solv}) of 75 wt% and $R_w=0.941$ (chapter 2.3). Samples with changes for these parameters are marked accordingly.

4.1. Gel Time

The type of precursor determined the gel time t_{gel} (i.e. the time at which a continuous network was formed after starting hydrolysis and condensation reaction). It was determined just by taking the time from the start until the vessel could be turned upside down, without any appearance of viscous movement. It is well known that increasing the length of the alkoxy groups (e.g. TMOS \rightarrow TEOS) increases the gel time by a decrease of the reaction rate. However, by replacing an alkoxy group by an aliphatic group, t_{gel} decreased dramatically.

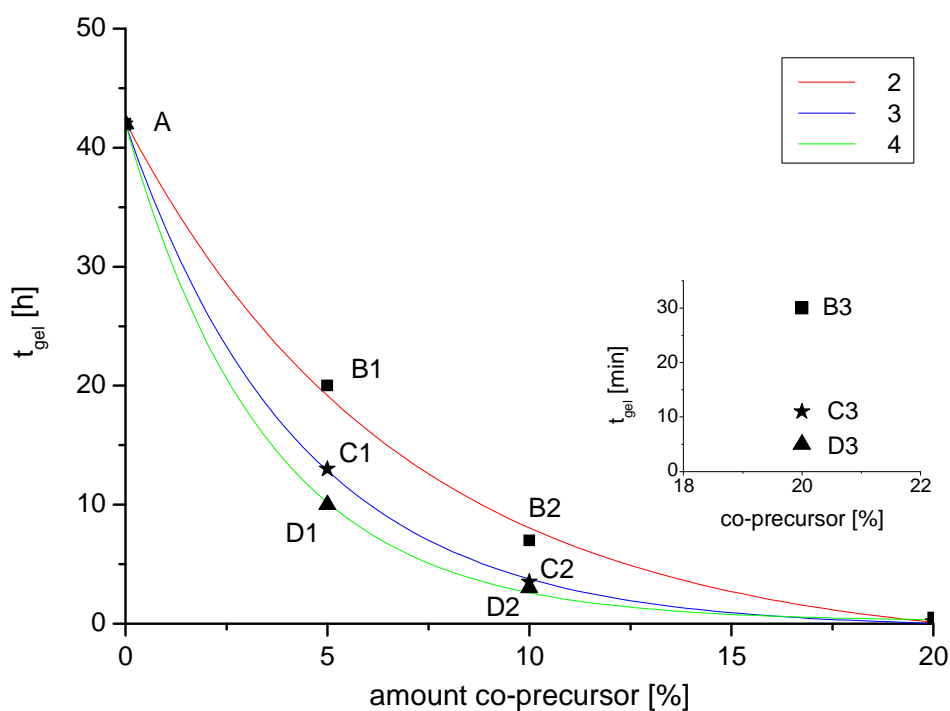


Figure 12: Gel times of the various precursor mixtures; $C_{\text{solv}} = 75$ wt%

Samples made of TMOS (sample **A**; the compositions of the various samples are given in tab. 10; chapter 3.3) took over 40 h to gel, if they stood tightly sealed. Already the addition of 5 wt% **2** lowered t_{gel} by the half (fig. 12). The longer the spacer length of the co-precursor, and the higher its amount in a mixture with TMOS, the shorter became the gel time. At 20 wt% amount it took only a couple of minutes to turn the colloidal solution

Results

into an elastic gel body. Experiments for higher amounts failed, since t_{gel} was already reached before the solution could be casted in an appropriate vessel. Therefore, 20 wt% amount of co-precursor in a mixture with TMOS was the limit for reasonable use of the approach.

Table 13: Gel times of various mixtures, varying C_{solv} and R_w

sample	solvent content [wt%]	R_w	t_{gel}
A	75	0,941	~ 42 h
A ($C_{\text{solv}}=85\%$)	85	0,941	~ 30 h
A ($C_{\text{solv}}=95\%$)	95	0,941	~ 24 h
A ($R_w=2$)	75	2	~ 15 h
D3	75	0,941	6 min
D3 ($C_{\text{solv}}=85\%$)	85	0,941	6 min
D3 ($C_{\text{solv}}=95\%$)	95	0,941	6 min
D3 ($R_w=2$)	75	2	6 min

While samples made of TMOS gelled much faster with increasing solvent content and with a higher R_w value, samples with 20% **4** seemed to be not affected by this acceleration (tab. 13). A suggestion was, since t_{gel} was measured in minutes, it just appeared constant. Probably, the time decrease is just a few seconds.

4.2. Refractive Indices

To determine refractive indices, an Abbe refractometer, thermostated at 20 °C by a water bath, was used. The colloidal solution was measured immediately after addition of the precursor, by putting a drop of the sol on the refractometer. Fig. 13 gives a survey of refractive indices for samples with a constant solvent content of $C_{\text{solv}} = 75$ wt% and a difference in the precursor composition.

Results

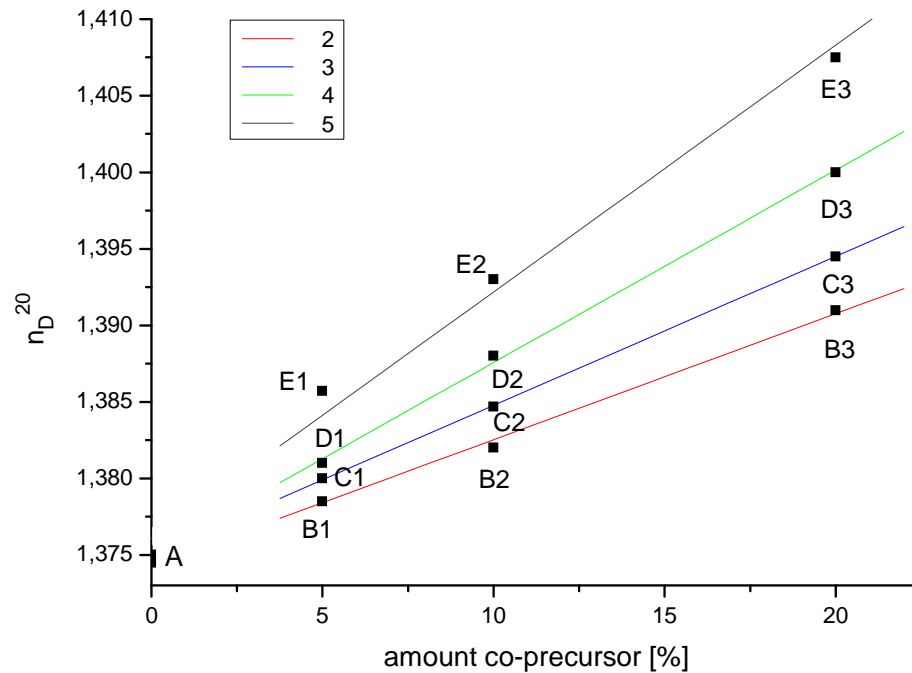


Figure 13: Refractive indices for various precursor mixtures; $C_{\text{solv}} = 75 \text{ wt\%}$

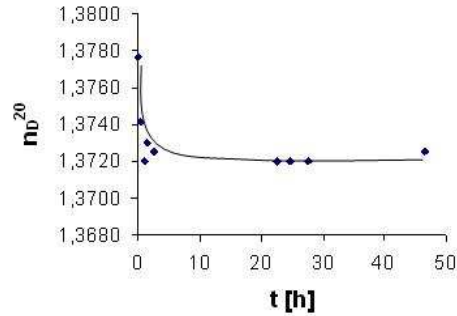
Samples without modification by a co-precursor, had a very low index ($n_D^{20} = 1.3750$). Raising the content of co-precursor and its spacer length resulted in an increase of the refractive index to values of about 1.41. Hence, enhancement of other material properties resulted in an unwelcome elevation of the refractive indices, and this would lead to a lower difference Δn from the host material to the polymer waveguide.

Depending on the type of precursor, the sol-gel transition took a certain time. To observe the alteration of the refractive index during this process, the change of the value was overviewed for the gelation of sample **A**, because it had the longest t_{gel} . The tightly sealed hardening vessel was equipped with a needle and a syringe, in order to take samples in a certain time interval (tab. 14).

Results

Table 14: Development of the refractive index of sample **A** during the sol-gel transition

time [h]	n_D^{20}
0	1.3777
0.5	1.3741
1	1.3730
1.5	1.3725
2.5	1.3730
22.5	1.3720
25.5	1.3720
27.5	1.3720
46.5	1.3725



After approximately 46 h, t_{gel} was reached. The refractive index remained almost constant throughout the whole gelation process with a slight decrease in the first hour, which has been neglected, since the carrier material had the lower index compared to the polymeric waveguide. Hence, refractive indices for the sol, can be taken as representative for those for the solid gel as well. Commonly, polymers exhibit a higher refractive index than the respective monomers, with an increase of app. $\Delta n = 0.04$ to 0.05 (e.g. 2-ethoxyethyl acrylate: $n_D^{20} = 1.4247$; poly(2-ethoxyethyl acrylate): $n_D^{20} = 1.4710$)

It was interesting, that with an increase of the solvent content, n_D^{20} decreased slightly both for samples with pure TMOS and for samples containing a co-precursor (tab. 15).

Table 15: Refractive indices of various mixtures, varying in C_{solv} and R_w

sample	solvent content	R_w	n_D^{20}
A	75	0.941	1.3750
A ($C_{solv}=85\%$)	85	0.941	1.3695
A ($C_{solv}=95\%$)	95	0.941	1.3655
A ($R_w=2$)	75	2	1.3715
D3	75	0.941	1.4040
D3 ($C_{solv}=85\%$)	85	0.941	1.4000
D3 ($C_{solv}=95\%$)	95	0.941	1.3980
D3 ($R_w=2$)	75	2	1.4060

To guarantee a reflection of light at the waveguide-cladding interface, the refractive index of the polymeric waveguides should be remarkably higher than those of the host

material. As mentioned in chapter 2.4, various types of monomers have been tested, in order to choose the most suitable one (tab. 16).

Table 16: Refractive indices of the contemplated monomers

monomer	n_D^{20}
HEA	1,4520
IBOA	1,4762
POEA	1,5200
BDDA	1,4569
EEEEA	1,4385
UA	1,4600
TPA	1,4748

Concerning the refractive indices, it was obvious that all monomers are suitable to serve as compound for waveguide structuring with the stipulated increase of at least $\Delta n \geq 0.003$ compared to the cladding material. Since compounds with aromatic groups had the highest values, 2-phenoxyethyl acrylate (POEA) has been chosen as monomer for the infiltration. Besides, this monomer had a comparably low viscosity and did not show any coloration after polymerisation.

4.3. Observation of the Carrier Material throughout Preparation

4.3.1. General Considerations

To achieve a porous template for the precursor compounds, it was necessary to assemble the used surfactant CpCl·H₂O in a L₃-sponge phase. The formation was easily visible just by its clear water-like appearance.¹⁸ L_α lamellar phases in contrast were quite turbid, and furthermore discernible by their viscous behaviour. Solutions with a hexanol/surfactant ratio at the boundary to the L₃ “sponge” phase (i.e. ca. 1.12) did not appear turbid but very viscous. If the ratio exceeded the upper threshold of the L₃ phase, it became turbid again and separated into a cloudy and a clear phase when the agitation stopped.

Results

Based on fig. 4, the following fig. 14 shows the phases of a system with $C_{\text{solv}} = 75 \text{ wt\%}$ (chapter 3.2) from the left hand to the right hand side: L_{α} phase (hexanol/surfactant: ca. 1.06); $L_{\alpha} + L_3$ (ca. 1.12); L_3 phase (ca. 1.16); multiphase (ca. 1.24).

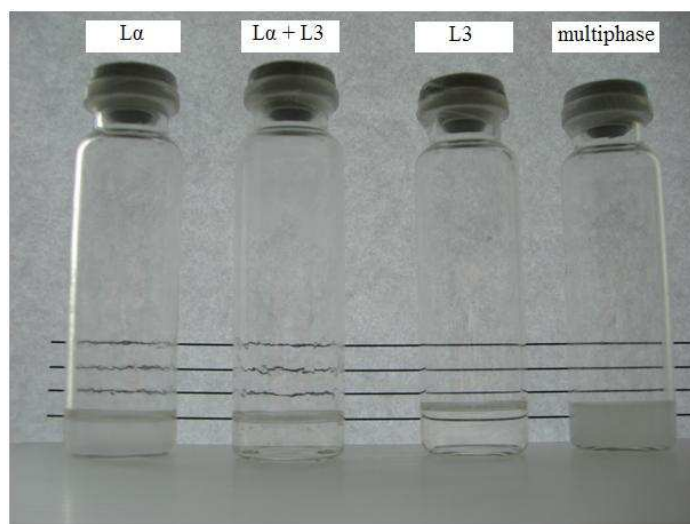


Figure 14: Appearance of the various phases of the system

1-hexanol / CpCl·H₂O / water ($C_{\text{solv}} = 75 \text{ wt\%}$)

A very crucial property of the carrier material was its transparency. Sample **A** appeared totally transparent and hence suitable for use for waveguide applications. Although addition of co-precursors with polyethyleneglycol spacer groups enhanced the mechanical properties of the material, the transparency suffered. The greater the chain length of the polyethyleneglycol and the higher the content of co-precursor, the more turbid the sample appeared, making formulations with co-precursor concentration $> 20 \text{ wt\%}$ and chain length $> n \approx 9$ (i.e. compound **4**) unsuitable for optical applications.

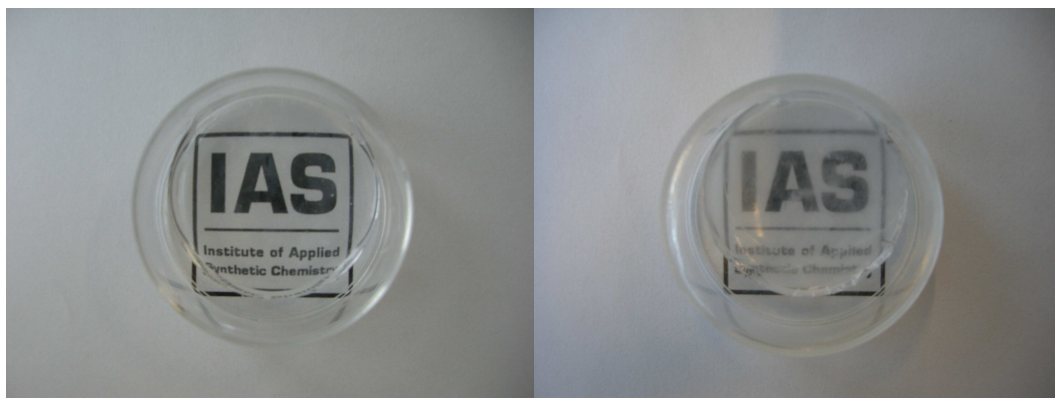


Figure 15: Turbidity as function of the co-precursor content (left hand side: **B1**; right hand side: **E3**)

Results

The left picture in fig. 15 shows the monolithic sample **B1**. Its appearance did not differ from samples made of pure TMOS (sample **A**) and even for sample **D3** the transparency was fully maintained.

However, the right picture shows sample **E3** that had an unclear result regarding the synthesis (chapter 2.1). In the image, there is an obvious cloudiness visible. A reason could be that PEG 600 is already a turbid solid at room temperature, and hence the according co-precursor compound remained turbid as well. Dissolving in TMOS and addition to the prepared L₃-sponge phase solution did not change the appearance and neither do the gelation process. Hence, PEG 400 has been chosen as upper threshold for the spacer length.

Moreover, the turbidity got stronger for a solvent content of 95 wt%. Acc. to literature, the pore size increases with an increased solvent content, and it gets close the wave length of visible light for a very high solvent content, thus causing light scattering and therefore decreased transparency.

Another problem of the preparation procedure was the formation of macroscopic and microscopic cracks when the pore liquid vaporized.

Macroscopic cracking was triggered by the shrinkage of the material. By increasing the amount of co-precursor and the spacer length, this cracking could be suppressed. However, the shape of the sample had to be taken into account. Hence, crack-free thin films could be synthesised. Monolithic samples were more susceptible to cracking, especially when the solvent exchange from H₂O to EtOH had already been carried out. With water as solvent in the pores, even monoliths had a crack-free appearance (fig. 16). Obviously, this was caused by the higher surface tension and reduced volatility of water. Monolithic samples always had to be covered with ethanol prior to the infiltration with monomer, in order to avoid the vaporisation of the solvent due to microscopic cracks. Rinsing of the material with ethanol after the curing procedure for removal of the non-cured monomer from the host material always caused microscopic cracks immediately with the vaporisation of ethanol. As possibility, a second monomer with a remarkable lower refractive index could to be infiltrated (Acc. to chapter 3.3). However, for sample **D3**, the ethanol in the pores of thin films could be vaporized at any state of the preparation process in order to obtain an empty carrier material (fig. 16; the monolithic sample **D3** was still covered with some ethanol).



Figure 16: Suppression of cracking by co-precursors

The infiltration process with POEA induced a lot of stress in the porous carrier material, obviously released by the steric structure of the resin compared to the solvent. While thin films resisted those forces even after solvent exchange, monolithic samples cracked due to the infiltration process. However, by applying Soxhlet extraction the monoliths achieved enough resistance to withstand the stress of the infiltration, and thus this step didn't lead to further cracking.

4.3.2. Mass Loss

The mass values were tracked gravimetrically by an analytical balance by subtracting the tare of the used vessel. It should be noted that it was not possible to remove the solvent from the sample completely, due to the danger of cracking by solvent evaporation in the samples. Checking the reproducibility with several samples of the same composition revealed that the values are affected with an error of app. $\pm 3 - 5\%$ and can only be treated as estimation.

The mass of the samples always correlated with the status of the preparation procedure. Actually, each procedure resulted in an increase or decrease of the samples mass (fig. 17 and 18):

Results

- Each solvent exchange step (chapter 3.3) removed a certain part of the template. Regarding the lower density of ethanol compared to water, the mass should decrease in the same solvent volume.
- Contemporary to the respective steps of preparation, aging of the wet gel body released further volatile alcohol compounds.
- Soxhlet extraction removed the remaining template, leading to a further lowering of sample mass. Furthermore, a significant shrinkage, caused by further condensation reactions of the precursor, contributes the main part of mass loss at this point of preparation (compare to chapter 4.3.4).
- Of course, infiltration of monomer into the pores led to an increase of the sample mass. In fact, this can be taken as indicator that actually porosity was present.

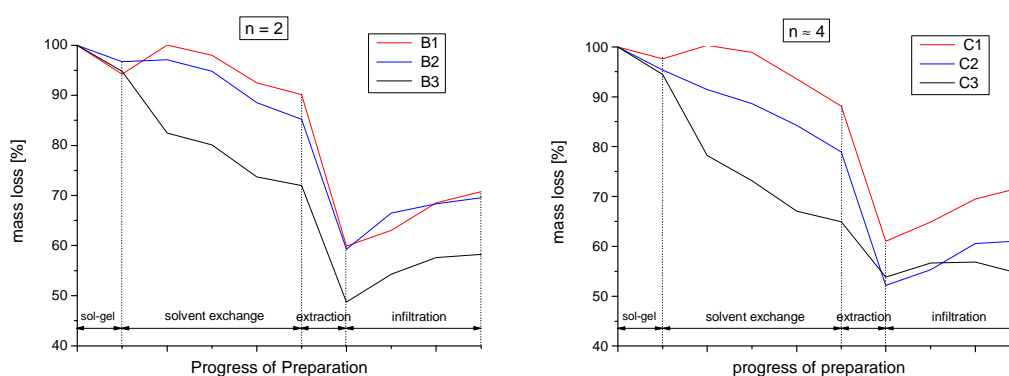


Figure 17: Mass loss of samples **B1 – B3** (left figure) and **C1 – C3** (right figure)

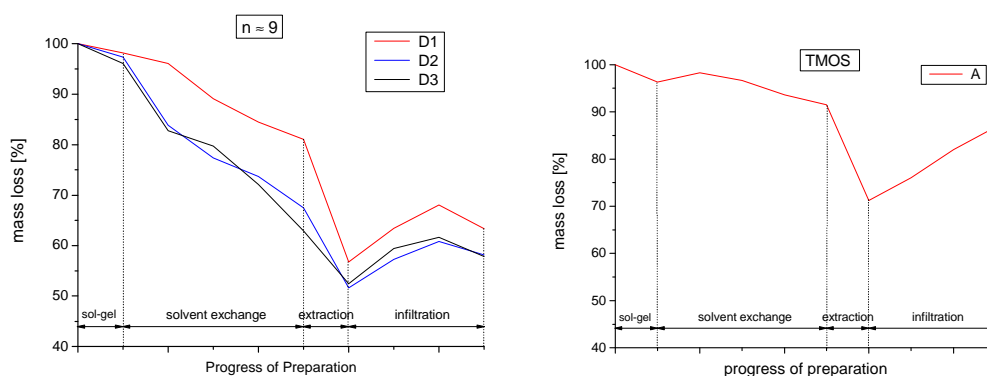


Figure 18: Mass loss of samples **D1 – D3** (left figure) and **A** (right figure)

First of all, the sol-gel transition caused development of methanol and ethanol, respectively. This was accompanied by a general mass loss of app. 5 wt%. Subsequently, exchanging the solvent from water to ethanol in 4 steps led to a very different course in the mass change tendency between the respective compositions. Increasing the amount of co-precursor and its spacer length resulted in a remarkable mass loss compared to sample **A**. A possible reason was that according to chapter 2.3, the spacer lengths governed the molecular weight of the co-precursors and hence the initial mass. Due to the increasing ratio of precursor mass to water + template mass, this fact could lead to a decrease in the porosity and hence to a lowering of the solvent contribution to the total weight of the sample. Since the different behaviours of the various mass losses during solvent exchange were determined by the sol-gel process, the decrease of mass could be more pronounced for samples with lower porosity. The contribution caused by the removal of template during the solvent exchange (chapter 4.3.3.) should be the same for each sample. A remarkable behaviour was that the longer the spacer length, the curve with 10 wt% co-precursor amount approached from the curve with 5 wt% co-precursor amount to the curve with 20 wt% co-precursor amount. This could indicate a similarity in the pore volumes of the respective samples.

Continuous Soxhlet extraction led to a further drop in the mass to app. 50 – 60 wt%, again with the lower values for samples with a high amount of co-precursor. Finally, the last part described a mass increase due to infiltration.

4.3.3. Removal of Template

Surfactant and hexanol, respectively, were removed by the treatment with ethanol. This was carried out both during the solvent exchange and Soxhlet extraction. Each exchange step removed a certain part of template from the sample. For quantification, the solvent fractions from a sample series with the same composition were collected and vaporized by a rotary evaporator (50 °C; 90 mbar). Hence, the respective dissolved template was isolated, measured by NMR-spectroscopy and could be compared with the initial weight of surfactant and hexanol.

Results

Sample **D3** serves as example:

- L₃-sponge template: 0.43g 1-hexadecylpyridinium chloride monohydrate, 0.501g hexanol, 2.802g 0,2 M HCl
- Precursor: 4.373g TMOS ; 4.272g ICPTES/PEG400

Hence, the total mass was 12.377g. The mixture was cast into six hardening vessels with a diameter of 2.25 cm. Monolithic samples (each three of 3 mm and 5 mm height) were obtained and treated as described in chapter 3.3.

1-Hexadecylpyridinium chloride monohydrate:

¹H-NMR (CDCl₃) δ [ppm]:

9.42 (m, 2H, Aryl H); 8.45 (m, 1H, Aryl H); 8.09 (m, 2H, Aryl H); 4.86 (t, 2H, ≡N⁺H-CH₂-CH₂-(CH₂)₁₃-); 3.27; 2.06 (s, 1H, ≡N⁺H-CH₂-); 1.93 (m, 2H, ≡N⁺H-CH₂-CH₂-(CH₂)₁₃-); 1.14 (bs, 26H, -(CH₂)₁₃-); 0.76 (t, 3H, -(CH₂)₁₃-CH₃)

1-Hexanole:

¹H-NMR (CDCl₃) δ [ppm]:

3.56 (t, 2H, -CH₂-OH); 1.73 (bs, 1H,-OH); 1.30 (t, 2H, -CH₂-CH₂-OH); 1.22 (m, 6H, CH₃-(CH₂)₃-); 0.83 (t, 3H, CH₃-);

As determined by ¹H-NMR spectroscopy, the various residua from the solvent evaporation consist of CpCl·H₂O and 1-hexanol, respectively. Since 1-hexanol, is not soluble in water, only the residue from solvent exchange 3 showed a remarkable content of it (CpCl·H₂O:1-hexanol = app. 2:1). Tab. 17 shows how much template the three solvent exchange steps removed from the monolithic samples in comparison to the initial weight of the template.

Table 17: Recovered template from the various residua

substance	mass [mg]	rel. mass [%]
used template (surfactant and hexanol)	931	100
residue from solvent exchange 1	360	39
residue from solvent exchange 2	160	17
residue from solvent exchange 3	170	18

According to the addition of the three residua from the solvent exchange steps, it could be reasoned that app. 75 wt% of the template was removed just by solvent exchange. All the $\text{CpCl}\cdot\text{H}_2\text{O}$ should be dissolved, and the remaining amount of 1-hexanol was released from the carrier material by continuous Soxhlet extraction.

Since samples with the shape of thin films were difficult to extract in the common way by Soxhlet extraction, it was assumed to be sufficient to perform only solvent exchange for this sample type. Through the low thickness of the films (max. 200 μm), the diffusion of ethanol in the pores should be more effective as in monolithic samples. Additionally, the extraction, a very time and material intensive preparation step, could be skipped.

4.3.4. Shrinkage

The progress of the sol–gel process, from the gelation to the aging, caused certain shrinkage in the material. In general, the higher the amount and spacer length of the co-precursor, the higher was the shrinkage. The measured values were taken from the diameters of the samples (tab. 18 and 19).

Results

Table 18: Shrinkage of the various precursor compositions

sample	shrinkage in diameter after solvent exchange [%]	shrinkage in diameter after Soxhlet extraction [%]
A	0	17.1
B1	1.4	20.0
B2	2.9	22.9
B3	11.4	22.9
C1	2.9	22.9
C2	7.1	25.7
C3	14.3	25.7
D1	7.1	25.7
D2	12.9	28.6
D3	17.1	28.6

Table 19: Shrinkage of **A** and **D3**, varying C_{solv} and R_w

sample	solvent content	R_w	shrinkage of diameter after solvent exchange [%]
A	75	0.941	0
A ($C_{\text{solv}}=85\%$)	85	0.941	0
A ($C_{\text{solv}}=95\%$)	95	0.941	0
A ($R_w=2$)	75	2	0
D3	75	0.941	17.1
D3 ($C_{\text{solv}}=85\%$)	85	0.941	20.0
D3 ($C_{\text{solv}}=95\%$)	95	0.941	17.7
D3 ($R_w=2$)	75	2	13.3

Sample **A** results in a rather rigid network of recurrent units and hence there was no shrinkage during solvent exchange. However, samples containing co-precursor with flexible polyethyleneglycol units shrank during this process. The shrinkage values increased with longer spacer lengths and a higher amount of co-precursor. Thus, the diameter could decrease up to app. 17 % only by solvent exchange (**D3**). Obviously, the co-precursors and the therefore resulted increased flexibility of the material enabled further condensation reactions even during solvent exchange. Otherwise, a fast t_{gel} (chapter 4.1) could also correlate with a fast aging of the material and thus with a higher shrinkage.

Soxhlet extraction and its boiling ethanol caused a remarkable decrease of the samples volume in all samples, caused by further condensation reactions during the extraction. Apart from sample **D3**, this was accompanied with occurrence of macroscopic cracks at almost all samples. Probably, the increase of internal stress due to the shrinkage procedure triggered this cracking, and shrinkage was again more pronounced in samples with greater spacerlength and higher amount of co-precursor. The maximum shrinkage observed was app. 29 % from its initial volume.

Obviously, increasing C_{solv} at constant R_w value did not affect the degree of shrinkage very much. However, an R_w value of 2 lowered the decrease of diameter compared to $R_w = 0.941$, which was commonly used for sample preparation.

4.4. Thermal Properties

The measurements were accomplished by thermogravimetric analysis (TGA) and differential scanning calorimetry (DSC) according to chapter 2.7. All monomer had to be removed from the samples surface prior to the measurements, in order to detect only the substance which was located inside the pores. An estimated error of app. 5 wt% had to be taken into account for the monomer vaporisation.

4.4.1. Thermal Behaviour of the Co-Precursor

The synthesised co-precursors were studied regarding their thermal behaviour and decomposition. The following fig. 19 and 20 show the behaviour of the co-precursor. The synthesis of these compounds is described in chapter 3.1.2.

Results

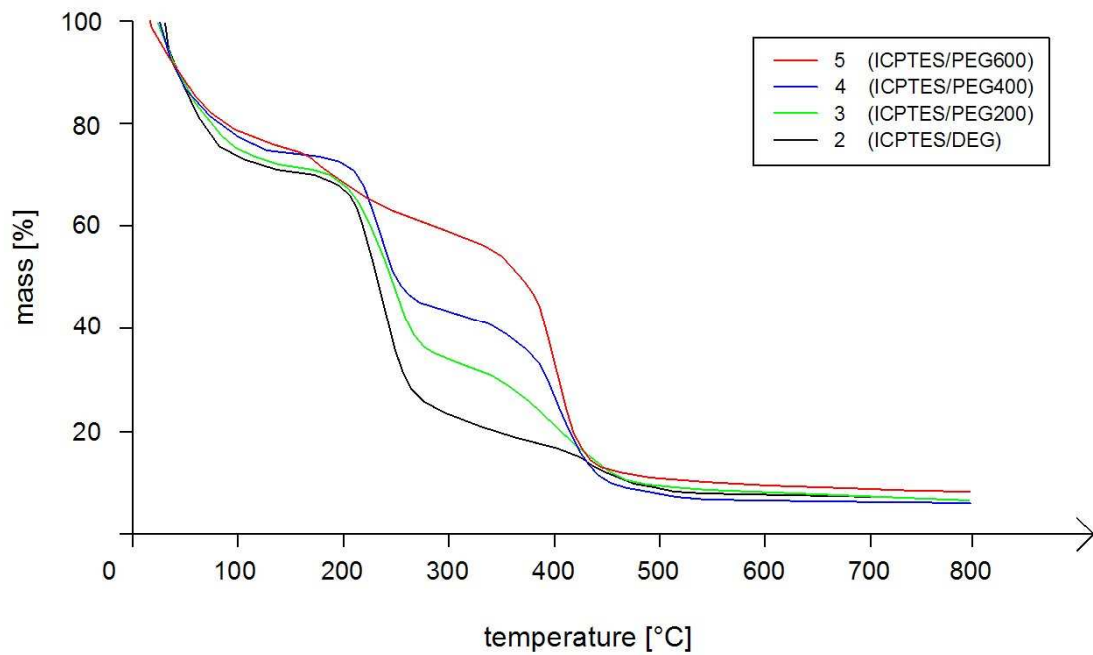


Figure 19: Thermogram of the various co-precursor compounds

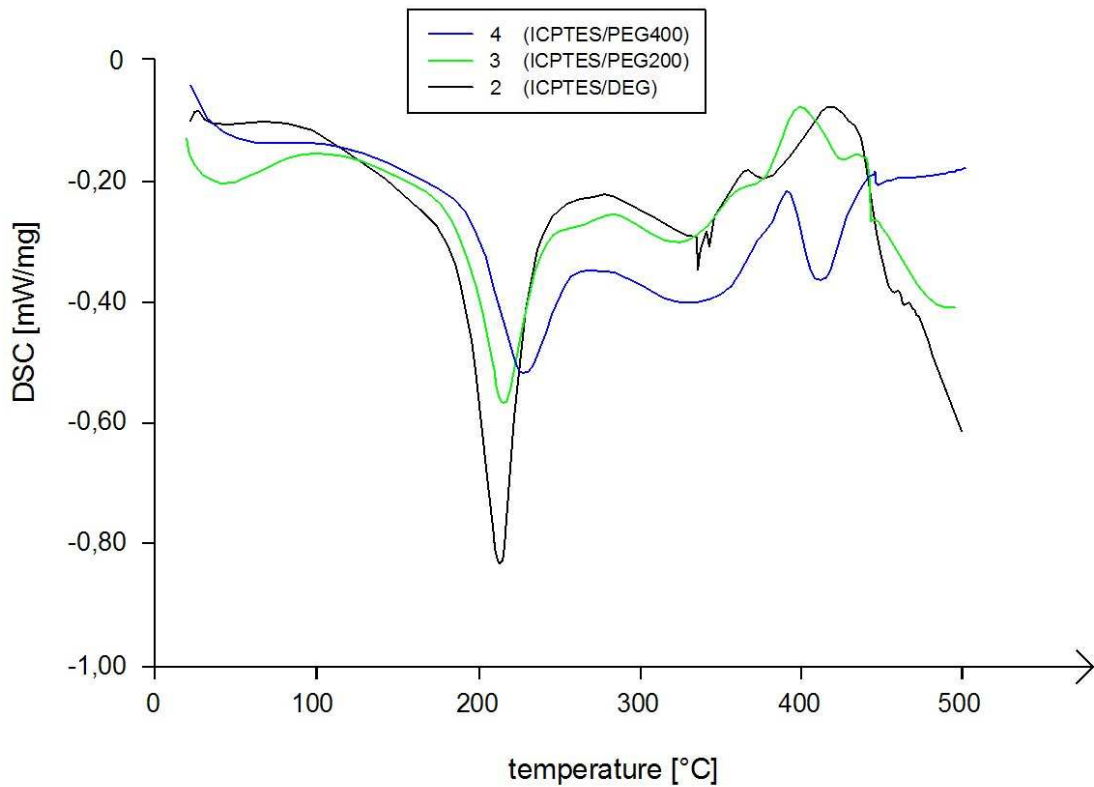


Figure 20: DSC measurements of the various co-precursor compounds

Results

The following significant steps occurred in TGA and DSC, respectively:

- The first mass loss occurred from room temperature to app. 100 °C. Apart from vaporisation of remaining ethanol from the pores, the thermal influence could carry on the condensation process and thus further alcohol could be composed. The weight loss was app. 22 – 27 wt%. After the measurement appeared the samples as small pieces of solid. Hence, gelation must have occurred during the measurement. Another contribution to that peak could be desorption of the chemisorbed species (e.g. H₂O) from the polyethylene spacer.⁴⁸ DSC showed a significant signal at app. 45 °C, which could be assigned to desorption.

According to TGA, the used PEG compounds decompose into gaseous products in a range from 250°C – 380 °C. The decomposition of co-precursors could be separated into three phases:

- The second weight loss in the thermogram was in the range 200 – 270°C. The respective DSC peak showed a physical transition of the PEG spacer, hence decomposition of PEG was assumed. The differences in the temperature of the peak for the various co-precursors, was app. 2.5 °C per ethyleneglycol unit and increased from compound **2** - **4**. Literature⁴⁸ suggested 3 K increase of melting point for each ethylene glycol unit for $M_w < 900$ mol/g.
- DSC measurements showed a chemical conversion at app. 335°C. This signal could not be assigned, but it should also have its origin also in the decomposition of PEG. In fig. 19, this third mass loss appeared as a slightly inclined line, constant for all the substances.
- The fourth weight loss (TGA: range 370 °C – 440 °C) described the final decomposition of the spacer in gaseous products. App. 10 wt% of black solids remains after the measurement. The blackening could indicate carbonic residua due to the decomposition of PEG.

Depending on the spacer length, the co-precursor decomposition behaviour varied regarding the drop of the second and fourth weight loss, respectively. A possible reason could be: Since, for pure PEG the decomposition appeared as one continuous drop, it could be assumed that there is a difference in the decomposition temperature, whether an ethyleneglycol unit was included in the chain or the connection to the silica compound and hence bonded to a urethane group. An increase of the spacer length decreased the

ratio of urethane groups to ethyleneglycol units. Hence, the second weight loss became lower and the forth weight loss became higher.

5 seemed to have a different thermal behaviour than other co-precursors. Since, this compound was not suitable for the envisaged applications, the origin of this fact wasn't investigated further (Probably the synthesis failed (chapter 2.1, 3.1.2); the according ¹H-NMR spectra did not reveal the success of the preparation).

4.4.2. Suitability of Monomers for Infiltration

The monomers listed in chapter 2.4, were investigated regarding their ability for infiltration of the carrier material (tab. 20). The monolithic host samples had the common composition **D3**. The infiltration process was carried out as described in chapter 3.3. It has to be mentioned, that app. 50 % of the used host materials showed macroscopic cracks, resulting from the extraction procedure, but despite this they could be tested. Since parts of EEEA cured during infiltration and thus remained on the sample surface, this monomer was not applied. The reason for the curing was not investigated in detail.

Table 20: Suitability of various monomers for infiltration

monomer	weight loss [wt%]	end point of weight loss [°C]	boiling points [°C]*	monolith
HEA	19	170	210 - 213	not broken
IBOA	18	185	245	broken
POEA	20	225	287	not broken
UA	not accurately detectable		not available	broken
BDDA	18	215	255	not broken
TPMA	7	200	> 200	broken

* Boiling points are obtained from various material safety data sheets, available in the internet:

HEA: <http://www.chemexpr.com/chemicals/supplier/818-61-1.html>

IBOA: <http://98.130.76.221/products/5888-33-5.htm>

POEA: <http://ntp.niehs.nih.gov/files/Phenoxyethylacrylate2.pdf>

BDDA: http://www.veredelungschemikalien.basf.de/ev-wcma-in/internet/en_GB/function/evproducts/document/30041345/TI

TPMA: <http://redox.com/mdms/data/MONOMC10.html>

IBOA, UA and TMPA were not suitable for the intended application, since the samples broke into small pieces during infiltration. Perhaps, the molecules are not flexible enough and exhibit a high double bond conversion or a high polymerisation heat. However, it was possible to infiltrate HEA, POEA and BDDA in the carrier material. Due to its aromatic structure, POEA had the highest refractive index of these monomers and hence the biggest difference to the value of the host material. While HEA became slightly yellow with time, POEA remained colourless and transparent.

The weight loss caused by monomer vaporisation was quite similar for all the tested substances (18 – 20 wt%). Furthermore, the difference between the end of the respective first bends and the theoretical boiling points was rather constant. Apparently, the monomer vaporized slowly before its boiling point was reached. In fact, these two arguments indicated that the tested carrier material is porous and able to take up monomer. The stepwise infiltration with mixtures of EtOH and monomer should minimize effects of obstruction caused by a high viscosity.

4.4.3. Monomer Content in the Carrier Material

Samples, which were already infiltrated with a suitable monomer, were investigated in this chapter. The mass loss regarding the amount of vaporized monomer gave an estimation of the materials volume, which could receive monomer, and thus an insight to the porosity of the material was given.

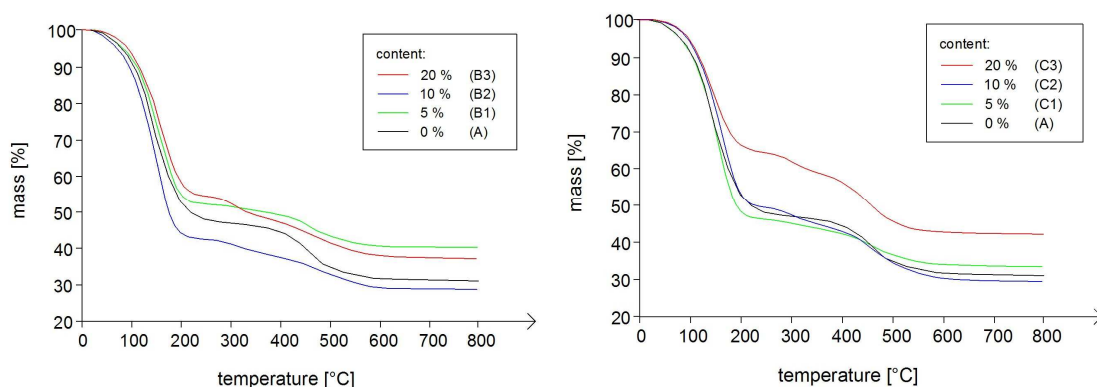


Figure 21: TGA measurements of samples containing **2** or **3** as co-precursor

Results

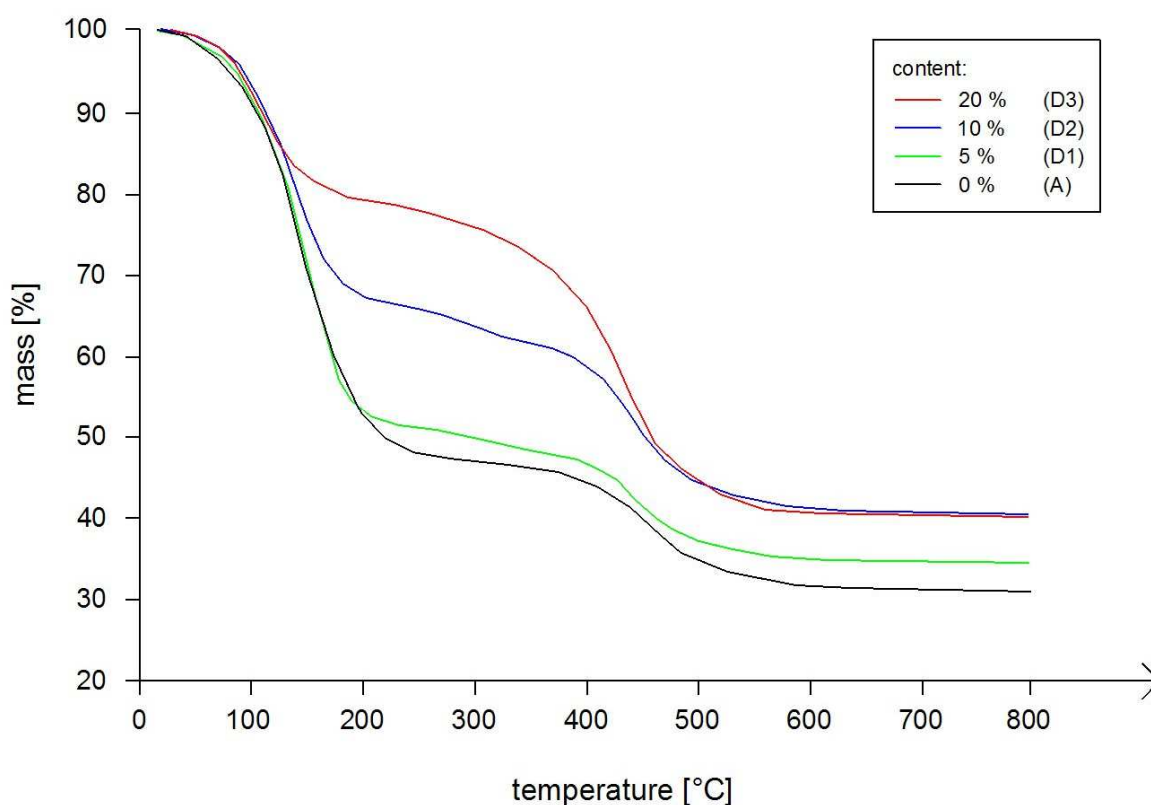


Figure 22: TGA measurements of samples containing **4** as co-precursor

The chosen substance to be infiltrated in the carrier material was HEA. Hence, the first bend ends between 165°C and 215°C depending on the sample.

Fig. 21 and 22 show the results from TGA measurements of samples with three different co-precursors and a solvent content of 75 wt%. (tab. 9). Besides, for sample **A** mass loss occurred at the same temperature range as the forth bends for samples with co-precursor. Not converted precursor seemed to decompose at this temperature range. Note that sample **A** retained its transparency after the measurement, while samples with co-precursor content appeared as black solid. A tendency of a higher remaining weight after TGA with higher co-precursor content could be observed.

The first drop in mass of sample **B2** was much more pronounced than that for **B1**. Probably, there was some monomer remaining on the surface which increased the drop. In general, an increase of the co-precursor content decreased the vaporized monomer amount, i.e. the samples volume accessible to monomer decreased.

The values ranged from app. 49 - 53 wt% for samples with 5 wt% co-precursor, to 45 – 20 wt% for samples with 20 wt% co-precursor content. Therefore, it can be speculated

Results

that the co-precursor compounds lowered the pore volume due to an increase in wall thickness although the total volume of the formulation increased respectively to the molecular weight of the used substance.

For waveguiding applications, formulation **D3** as carrier material for the chosen curable monomer POEA had a crucial consequence: To guarantee waveguiding, the difference between the refractive indices of a waveguide and the host material had to be at least $\Delta n_D^{20} \geq 0,003$. According to the results from TGA, a waveguide consists of app. 80 wt% carrier material with $n_D^{20} = 1.4040$ and 20 wt% POEA with $n_D^{20} = 1.5200$. Therefore, the difference between the refractive indices of a waveguide and the host material had to be five times greater than $\Delta n_D^{20} \geq 0,003$. Despite this, the difference was indeed $\Delta n_D^{20} = 0.1200$ and thus the stipulated increase should be possible.

The following figure shows TGA measurements from different states of the carrier materials preparation for sample **C2**.

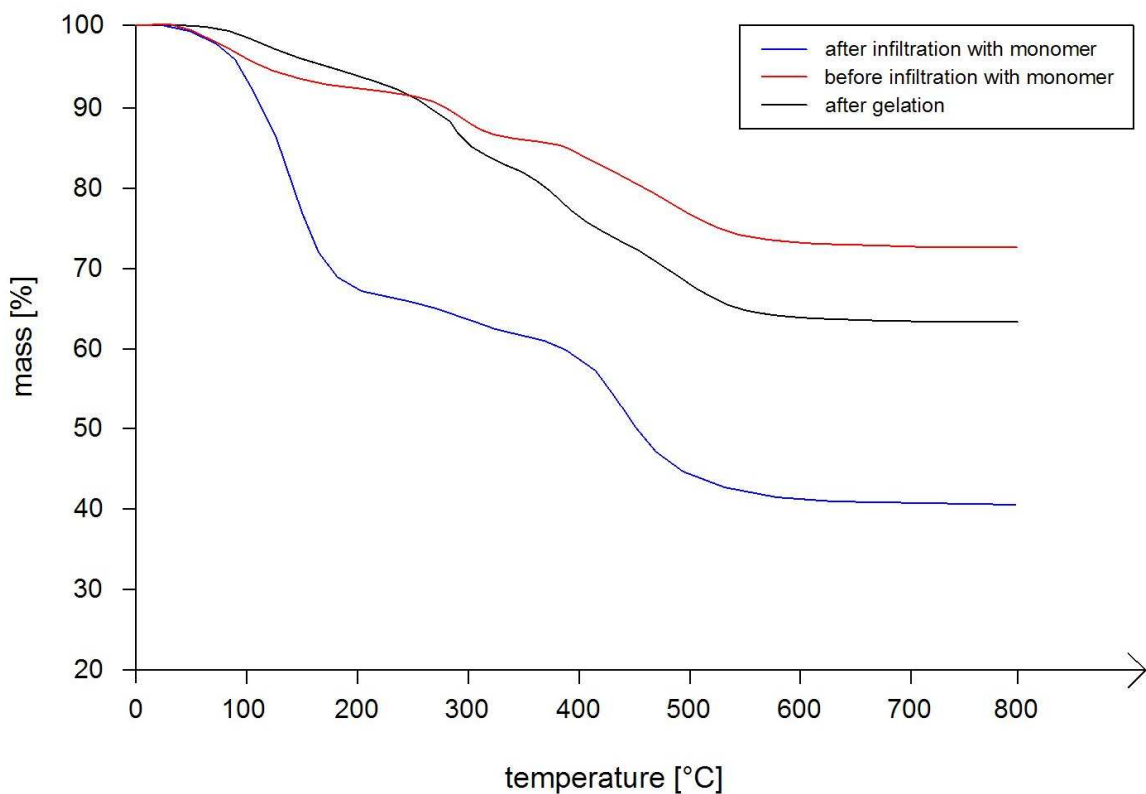


Figure 23: Tracking the carrier materials preparation regarding its thermal behaviour

There was a reduced total mass loss for the empty carrier material with accomplished Soxhlet extraction (red curve of fig. 23) compared for samples which only were allowed to gel (grey curve). The reason was the ethanol, which removed the template from the material during the exchange steps. Although the respective solvent was allowed to vaporize, there is still a weight loss at a temperature range of room temperature – 120 °C. Either, solvent was still remaining in the carrier material or further condensation reactions occurred. Since the drops of the two curves are slightly displaced, the first reason seems to be more likely.

The content of surfactant and 1-hexanol was 9 wt% of the initial weight. Since the mass loss of the grey curve was 9 wt% more than those of the red curve, it could be considered that the whole template was removed ($\text{CpCl}\cdot\text{H}_2\text{O}$ vaporized at ap. 220 °C; compare to chapter 4.3.3). Furthermore, the infiltration caused a remarkable first drop (blue curve), while the rest of the curve structure remained the same compared to the empty carrier material.

4.5. Mechanical Properties

Indentation depth-controlled nano indentation was chosen to be the method for investigating the mechanical properties of the various samples (chapter 2.8). To guarantee the accuracy of a measurement, 10 – 12 loads were carried out on one sample. In general, an uncertainty of app. 3 – 5 % both for determination of indentation modulus and hardness had to be considered. The measurements provided the sample load as function of the displacement of the Berkovich indenter in the sample. For all measurements, the maximum indenter depth was constantly adjusted at 1 μm . Hence, indenter modulus and indenter hardness could be derived from the curves. Some measurements were repeated, in order to investigate the reproducibility of the method. Regarding the accomplishment, measurements were only carried out with monolithic samples.

4.5.1. Indentation Hardness (H_{IT})

Hardness describes the resistance of a certain material against penetration by a harder material. In general, increasing both the spacer length and the amount of the co-precursor lowered the hardness of the respective sample.

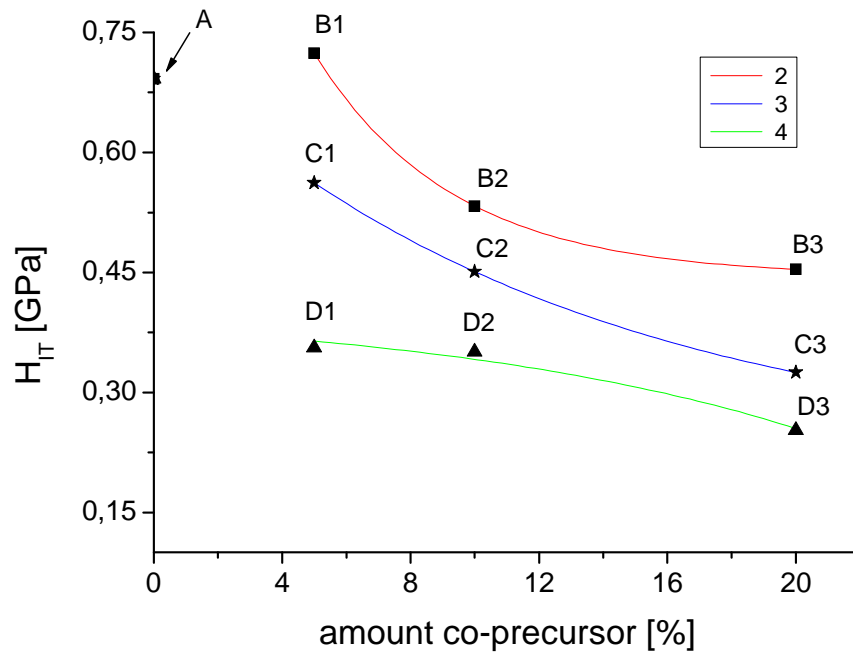


Figure 24: Indentation hardness as function of the co-precursor content

The increase of both co-precursor content and spacer length governed a remarkable decrease of the materials indentation hardness (fig. 24). However, a higher spacer length reduced the drop of hardness when the amount of co-precursor was increased. Apparently, a high molecular spacer influenced the hardness already in low contents, since a high spacer length resulted in a reduced decrease. Thus, an indentation hardness $E_{IT} = 0.253$ GPa could be achieved, i.e. the value could be reduced to one third of the value for a carrier material consisting of pure TMOS.

The uncommon increase of hardness for sample **B1** will be discussed together with indentation modulus in chapter 4.5.2.

Applying equation (9), Vickers hardness HV could be related H_{IT} , expressed in the unit [N/mm²] (1 GPa = 1000 N/mm²) by a scaling factor (tab. 21). As comparison: Iron: 30 – 80 HV5:

Results

Table 21: Vickers hardness derived from indentation hardness

sample	indenter hardness H_{IT} [N/mm ²]	Vickers hardness [HV]
A	699	(6.47)
B1	724	(6.70)
B2	533	(4.94)
B3	454	(4.20)
C1	562	(5.20)
C2	451	(4.18)
C3	325	(3.01)
D1	356	(3.30)
D2	351	(3.25)
D3	253	(2.34)

Table 22 shows the development of the hardness during the preparation of sample **D3**:

Table 22: Development of the indentation hardness during the preparation (sample **D3**)

step of progress	H_{IT} [GPa]
after gelation	0.068
after solvent exchange	0.044
after Soxhlet extraction	0.253

Exchanging the solvent from water to ethanol reduced the hardness of the material. However, extraction causes a remarkable increase accompanied by shrinkage of the sample, resulting from further condensation reactions of the gel, triggered by the high temperatures during the extraction. This led to a higher resistance of monolithic samples against microscopic and macroscopic cracking during the subsequent infiltration with monomer, although that fact was achieved on the expense of a remarkably decrease of flexibility. Obviously, Soxhlet extraction involved a soft type of drying procedure.

An obvious consequence of the reduced indentation hardness combined with the decrease in indentation modulus was the remarkably decreased tendency to macroscopic cracks. This observation was correct for thin films and monolithic samples without changed solvent, i.e. water in the pores. However, for monolithic samples with ethanol in the pores, microscopic cracking occurred during vaporization of the solvent. Not even the threshold content of co-precursor in sample **D3** could avoid cracking of those samples.

4.5.2. Indentation Modulus (E_{IT})

Young's modulus (E), as a value for the materials stiffness, is defined by the ratio of an applied stress to the resulting strain. The smaller Young's modulus, the softer is the material. As described in chapter 2.8.2., instrumented indentation experiments yield that the indentation modulus is related to the Young's modulus of the material. Concerning the behaviour of indentation modulus it is obvious that it resembled that of the indentation hardness (fig. 24). Fig. 25 gives a survey over the measured indentation modulus for various formulations of carrier material:

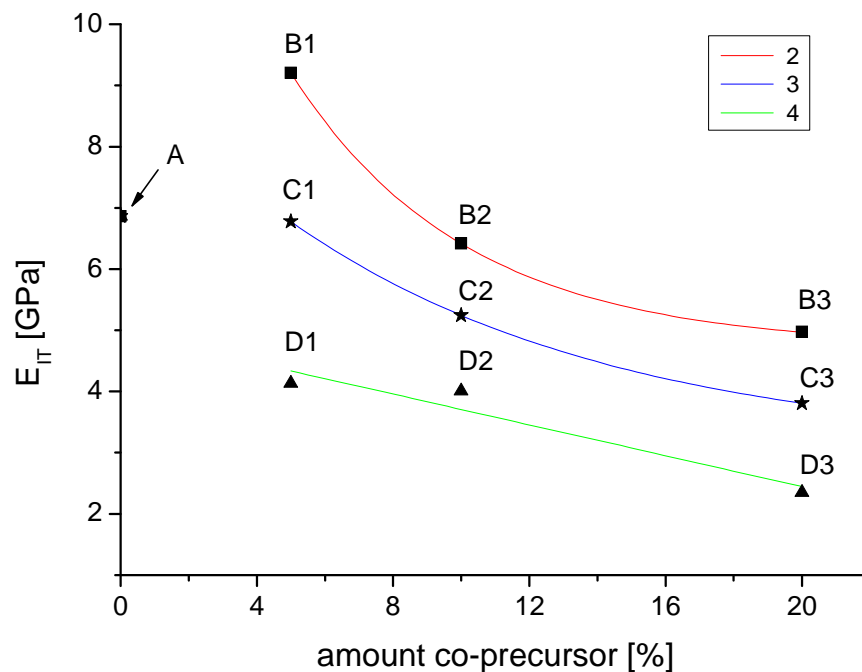


Figure 25: Indentation modulus as function of the co-precursor content

An interesting result was the remarkable increase of indentation modulus in the sample **B1** compared to sample **A** (pure TMOS) as precursor. Possibly, the reason for this behaviour was an increase of the wall thickness by addition of co-precursor compounds. Hence, this could lead to an increase of stiffness in the sample. Although the wall thickness increased further, a higher content of co-precursor apparently counteracted this effect by the increased contribution to elasticity. Formulations with a higher number of ethyleneglycol units exhibited lower stiffness.

Thus, an indentation modulus of $E_{IT} = 2.347$ GPa (i.e. app. one third of the value for samples with pure TMOS) could be achieved, accompanied by a remarkably decreased tendency for macroscopic cracks, resulted from the reduced stiffness of the material. The development of the indentation modulus during the preparation process for sample **D3** is given in tab. 23:

Table 23: Development of the indentation modulus during the preparation (sample **D3**)

step of progress	E_{IT} [GPa]
after gelation	1.155
after solvent exchange	0.494
after Soxhlet extraction	2.374

Obviously, the removal of the template from the L_3 -sponge phase bilayer reduced the indentation modulus of the material by the factor two. However, treatment of the samples with boiling ethanol by continuous Soxhlet extraction was accompanied by an enormous raise of E_{IT} . As mentioned in chapter 4.3.4., elevated temperatures trigger further condensation of the precursor molecules. Hence, the network became tighter and the stiffness increased.

4.5.3. Plastic and Elastic Parts of the Indentation Work

To determine the plastic deformation work and the elastic reverse deformation work during the indentation process, areas under the curves for application and removal of the test force had to be calculated (chapter 2.8.3). The sum of these two amounts resulted in the total mechanical work, necessary to move the Berkovich indenter to the default indentation depth in the sample. Tab. 24 gives a survey over the work determined from the load as a function of displacement:

Results

Table 24: Plastic and elastic content of the total mech. work, necessary to indent to a depth of 1 μm

sample	W_{ges} [μJ]	W_{elast} [μJ]	W_{plast} [μJ]	η_{IT} [%]	$100 - \eta_{\text{IT}}$ [%]
A	5638,8	1883,8	3755,0	33,41	66,59
B1	5197,1	2407,6	2789,5	46,33	53,67
B2	3738,2	1956,8	1781,4	52,35	47,65
B3	2957,6	1764,5	1193,1	59,66	40,34
C1	3691,2	1873,5	1817,7	50,76	49,24
C2	3047,2	1696,1	1351,1	55,66	44,34
C3	2379,1	1363,1	1016,0	57,29	42,71
D1	2360,1	1265,1	1095,1	53,60	46,40
D2	2383,7	1366,3	1017,5	57,32	42,68
D3	1487,1	1148,5	338,5	77,23	22,77

Resembling to the development of the indenter modulus and the hardness, a high content of co-precursor and a high molecular spacer led to an increase of the elastic part of the mechanical deformation work. Samples without co-precursor were very brittle with a plastic deformation work content of app. 66 % (fig. 26). However, samples containing the composition **D3** as silica source were chosen for monomer infiltration. For these samples three quarters of the deformation work was elastic and hence an according raise in flexibility could be derived (fig. 27).

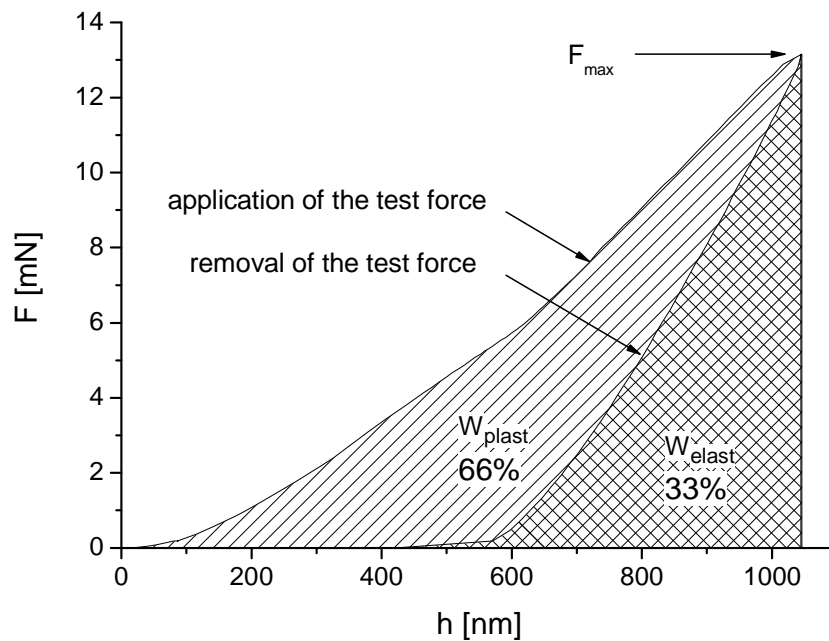


Figure 26: Mechanical deformation work of a sample **A**

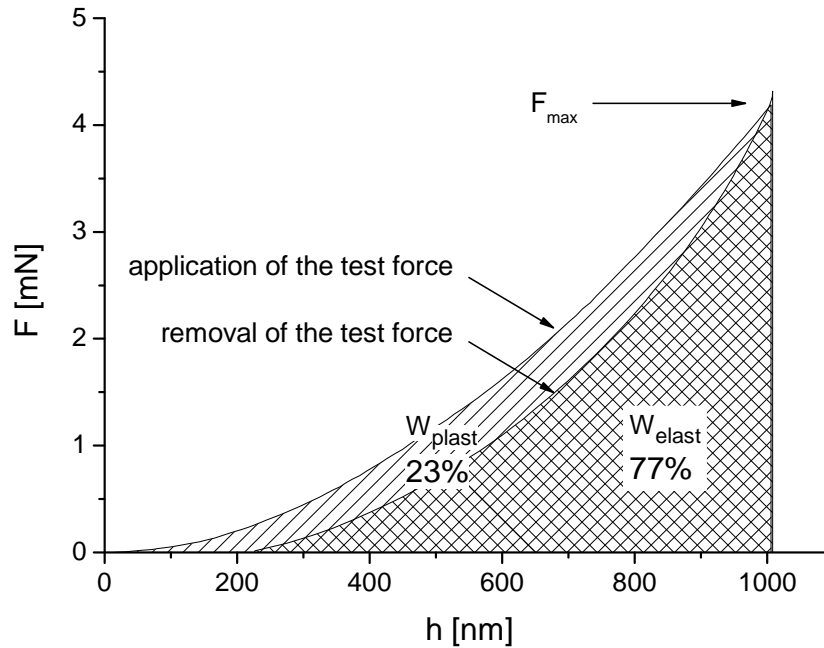


Figure 27: Mechanical deformation work of sample **D3**

A general conclusion from the measurements by nano indentation was, that by increasing the content of the co-precursor and the spacer length, a reduced brittleness of the samples occurred and hence an improved resistance against macroscopic cracking (compare to the observation in chapter 4.3.1). For thin films microscopic cracking could be suppressed as well.

4.6. Structural Properties

Surface measurements via N₂ Adsorption and using the Brunauer Emmet Teller (BET) and Barret Joyner Halenda (BJH) calculation approaches were carried out as well, but the results remain doubtful. According to these measurements, the pore size was very small for samples with pure TMOS as precursor and samples with additional co-precursor appeared dense. The samples were heat treated with app. 250°C prior to the measurement to desorb all adsorbed specie from the surface. Apparently, this caused damages in the structure, since microscopic cracks appeared on the sample after heat treatment. But for a

reasonable accomplishment of the measurements it was necessary to carry out this preliminary step. Thus, for the determination of porosity, other methods have been applied.

4.6.1. Scanning Electron Microscopy (SEM)

Prior to the measurements, the sample pieces were fixed on an appropriate carrier by a conductive silver-glue. The samples were covered with a thin gold layer via vapor deposition, in order to guarantee full conductivity. To estimate the influence of the various precursors on the porosity, images of the fracture areas were taken. The maximal zoom to obtain a reasonable resolution for the images was 15000 \times . It should be noted that due to the poor enlargement, pores in an expected size of several 10 nm could not be identified. Below, SEM images of the surface and the fracture surfaces of various samples are shown (Fig. 28 and 29):

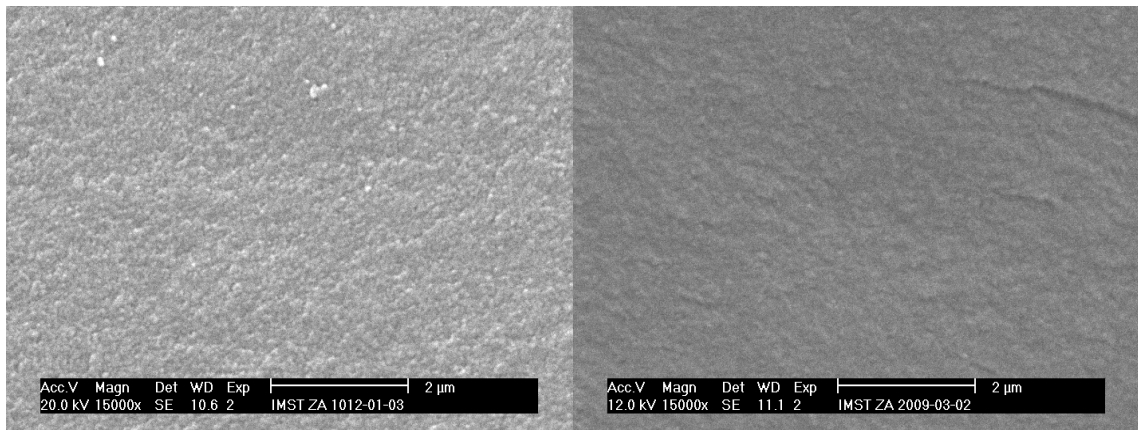


Figure 28: SEM images of a sample **A** (left) and sample **B3** (right)

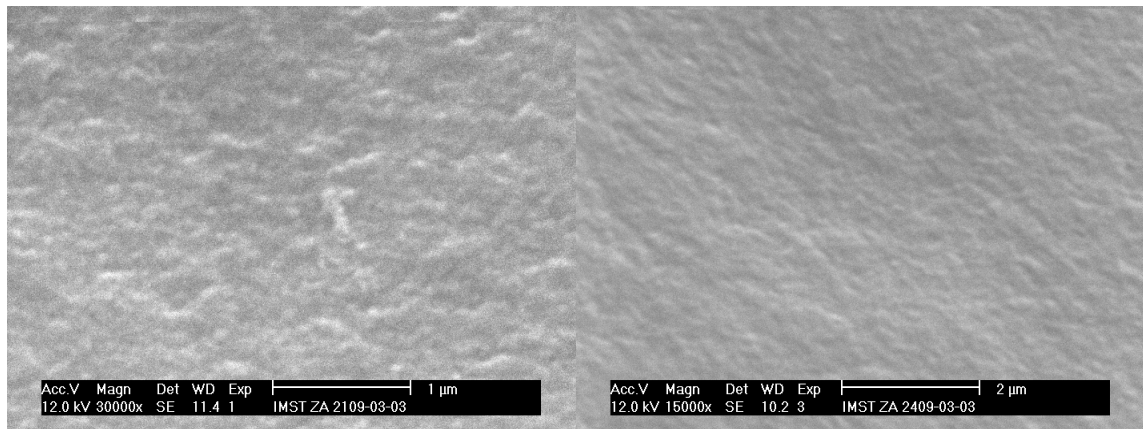


Figure 29: SEM images of a sample **C3** (left) and sample **D3** (right)

Considering the fine and irregular structure of the area, samples made of pure TMOS seemed to be rather porous. The irregularity of intensity regarding morphology would indicate an isotropic network of the pores, hence the L_3 “sponge” phase. Sample **D3** appeared quite dense and without any topographical structure as for pure TMOS. Contemplating a decrease of porosity with the spacer length, obviously a higher resolution would show the pore structure of the sample. The left picture in fig. 29 shows a blurry image of sample **C3** with a resolution of 30000 \times . Although a topological structure was visible, that could indicate porosity, no clear statement was possible. Obviously, pictures of the fracture surfaces did not reveal the pores due to the topology of the material, and a clean cut through the samples would lead to better results (compare to the AFM images in fig. 31).

In general, the SEM images suffered from poor resolution.

4.6.2. Atomic Force Microscopy (AFM)

AFM was accomplished at the FELMI Graz. Both images in the contact mode and in the non-contact (“tapping”) mode were made. Thereby, the “tapping” mode provided a much better resolution for the images.

Fig. 30 shows the fracture area of a sample **A** in the contact mode:

Results

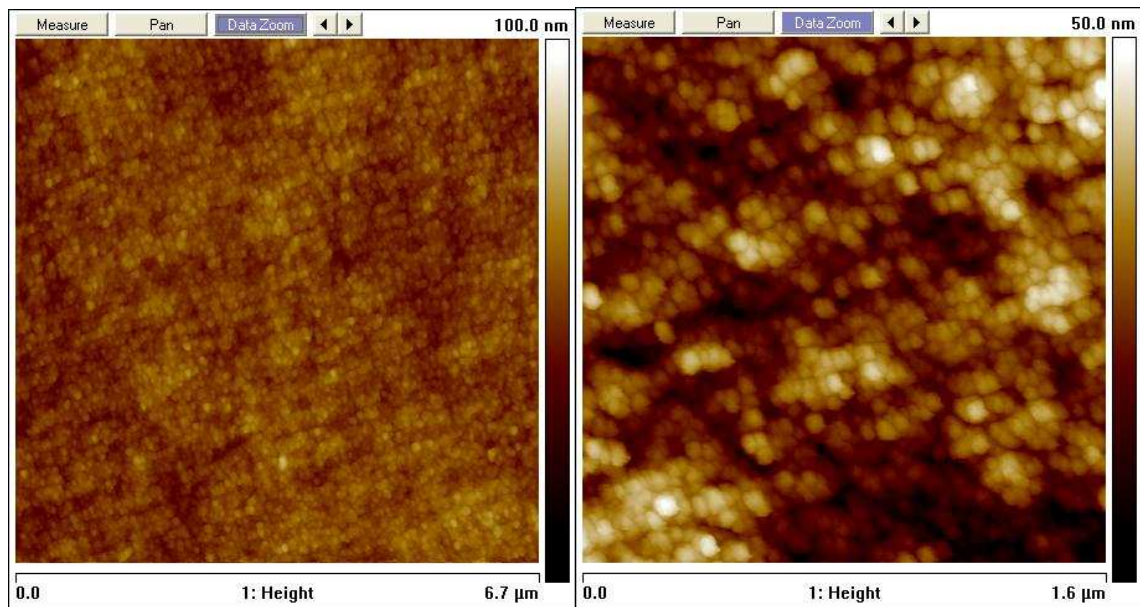


Figure 30: AFM images of fracture areas of sample **A** in different resolutions

The image on the left hand side of fig. 30 has a resolution, comparable with those made by SEM (Fig. 29). Corresponding to the SEM images, the black areas could be interpreted as deep holes, i.e. pores. The figure on the right hand side shows an image with a higher magnification that confirms a distinct topography. In fact, the difference in height is more than 50 nm, which gives the conclusion that the samples are porous.

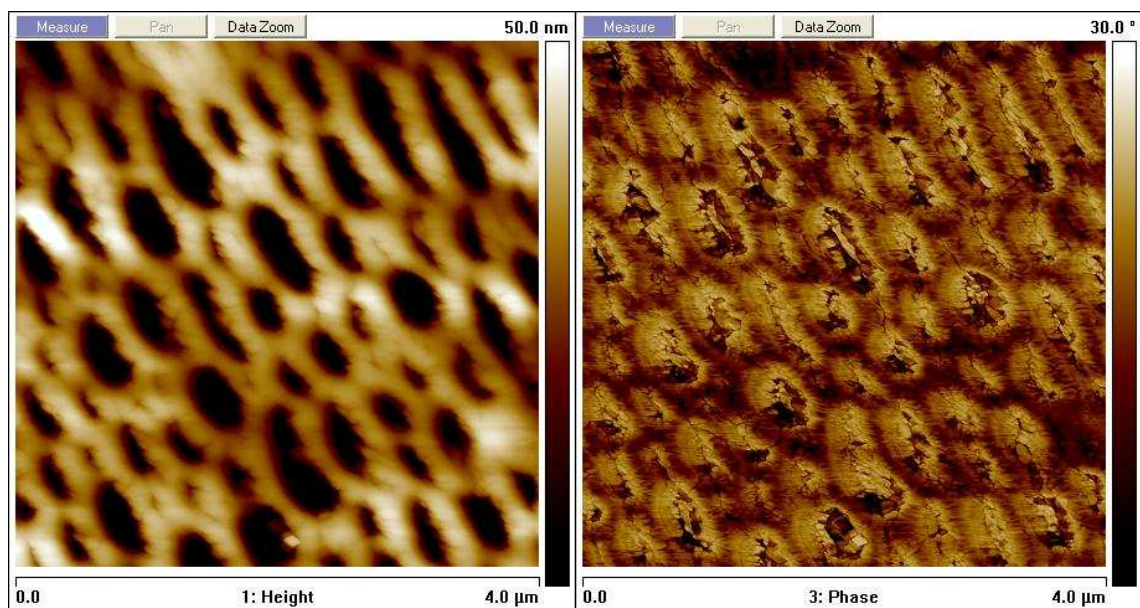


Figure 31: Cross-section AFM of sample **A** in contact mode (left image) and “tapping” mode (right image)

Results

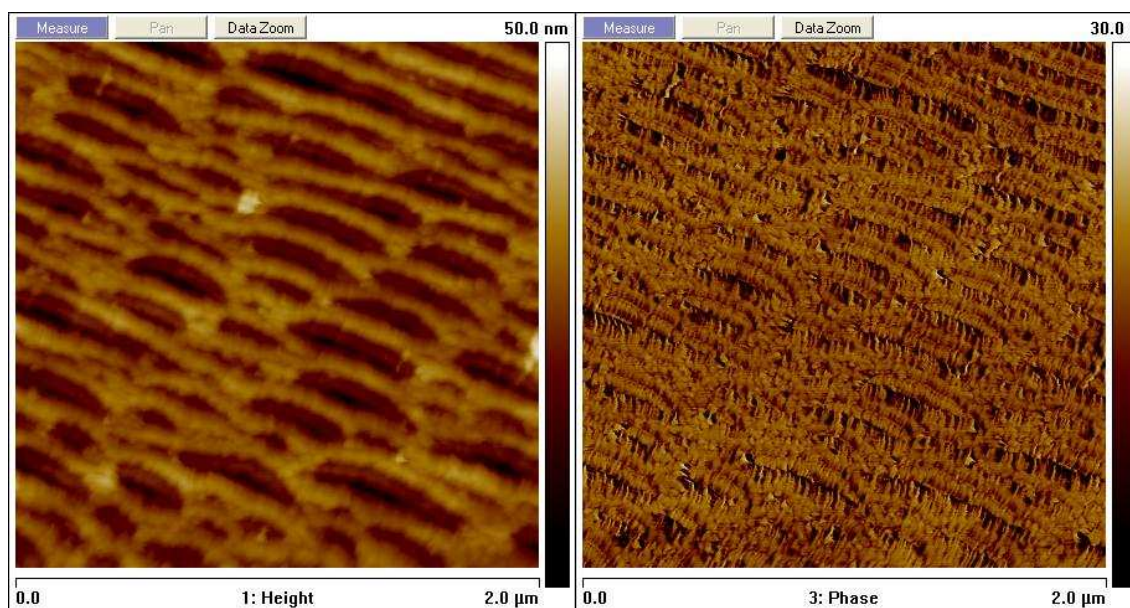


Figure 32: Cross-section AFM of sample **A** in contact (left image) and “tapping” mode (right image)

By applying microtomy, it was possible to obtain a cross-section of sample **A**. Thus, AFM images, which properly showed the pore size of the sample, could be recorded (right images of fig. 31 and 32; Fig. 32). The images contain a very structural surface indicating the L₃-sponge phase. In order to obtain reasonable images, it was necessary to dry the sample with nitrogen prior to the microscopy. The pore diameter varied between app. 80 and 280 nm, i.e. macroporous material was synthesized with SiO₂ walls between the pores (Wall thickness: app. 140 – 230 nm). Since the co-precursor increased the silica compound content of the total weight and hence the wall thickness, the pores were certainly smaller with a raise of the co-precursors content and the spacer length. According to chapter 4.4.3, the pore size could be three times smaller with the threshold formulation of **D3**. In fact, these samples, i.e. monoliths and thin films (fig. 33), did not show pores comparable to those from sample **A**. The appearing lines are artifact, caused by the sectioning of the samples at room temperature. At the moment it is obvious that samples consisting of formulation **D3** do not exhibit porosity, but probably sectioning at very deep temperatures would avoid the appearance of the artifacts, in order to make a better statement. Since the generation of waveguides was possible (chapter 4.7), there should be pores, large enough to be accessible for the monomer POEA.

The images on the right hand side of fig. 31 and 32 show images of sample **A** recorded in “tapping” mode. Hence, the scale on the right hand side of the images denotes the phase

Results

shift. Corresponding to the images taken in contact mode, the phase contrast obviously shows bilayers of host material (fig. 32).

Unfortunately, “tapping mode“ images of samples containing a co-precursor were not available at completion of this work.

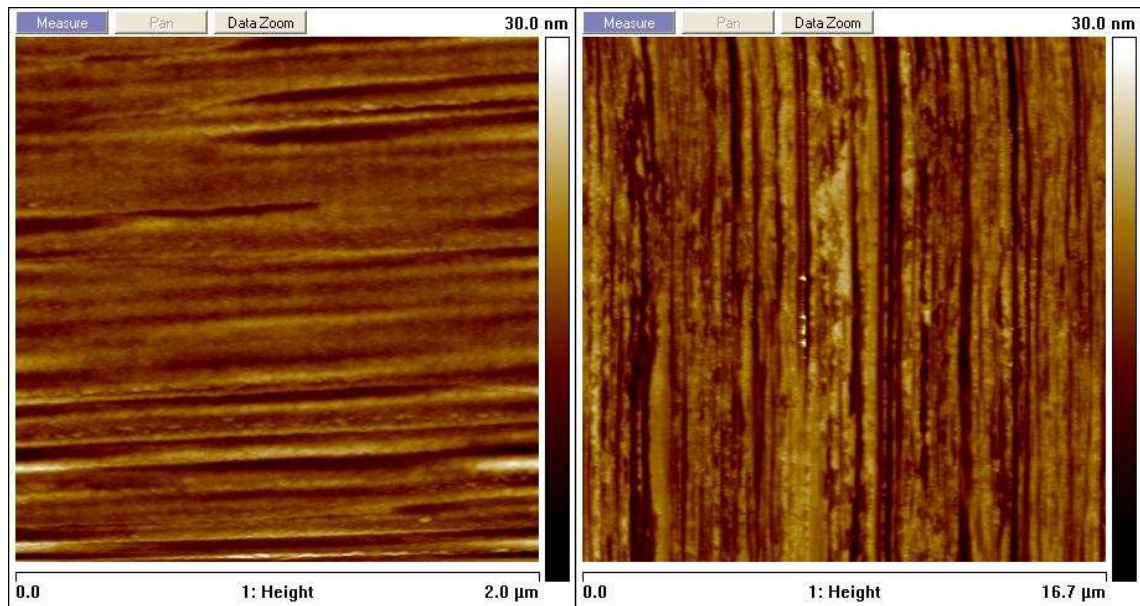


Figure 33: Cross-section AFM images of sample **D3**: monolith (left image) and thin film (right image)

4.7. Two Photon Polymerisation

The structuring process was carried out by Dr. Valetin Satzinger and Dr. Volker Schmidt on a TPP device at the Joanneum Research Institute in Weiz.

According to chapter 4.4.2, POEA was chosen to be infiltrated in the carrier material. 0.05 wt% NDPD initiated the curing process, but gave the samples a strong orange coloration. Formulation **D3** was used both for monolithic samples and for thin films. It was interesting that although AFM images (chapter 4.6.2) did not exhibit pores in sample **D3**, it was possible to inscribe waveguides in the infiltrated material.

The movement of the laser beam had a default setting of 20 mm/min.

All the images were taken with an optical microscope with different enlargements, both in transmitted light and phase contrast modus.

4.7.1. Varying the Laser Power

The fields consisted of 10 waveguides, where the first and the last line were inscribed with the maximum laser power of 200 μW . In between, the power decreased by 20 μW from line to line. For monolithic samples, the fields were inscribed both in a depth of 100 μm and 300 μm (fig. 34 and 35). Since the monolithic samples would get microscopic cracks caused by vaporisation of ethanol, the non-cured monomer was left inside the monolithic carrier for subsequent characterisation.

The depth for structuring waveguides in thin films was 75 μm and 125 μm , respectively (fig. 36 and 37). The total height of such a film was app. 200 μm .

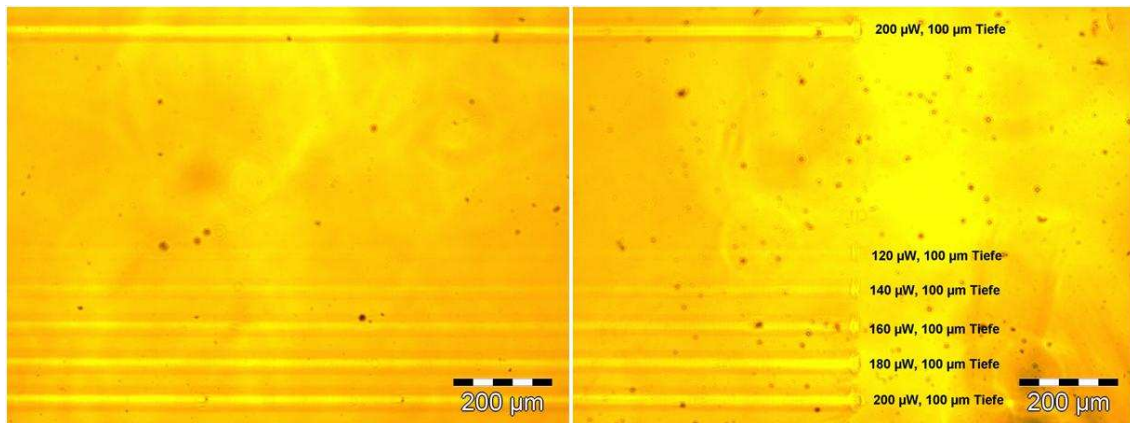


Figure 34: Structured waveguides in a monolithic sample, varying the laser power

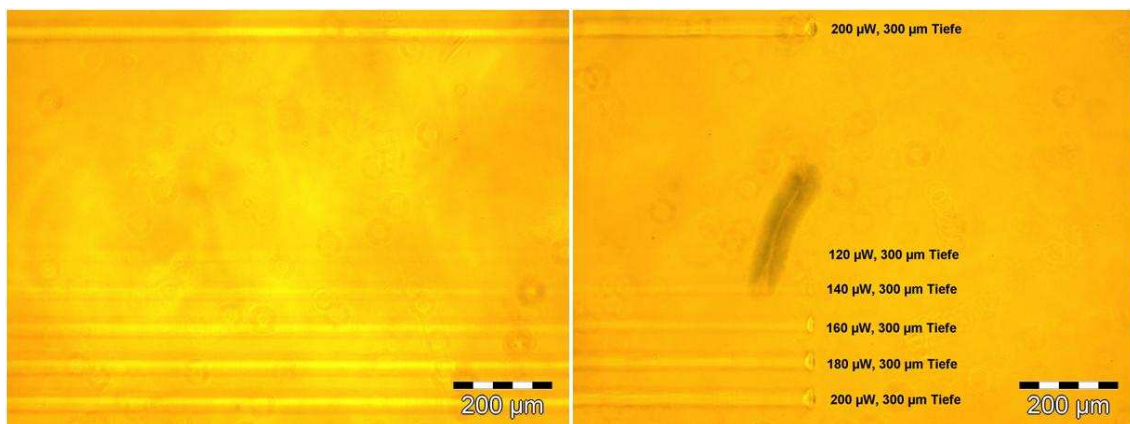


Figure 35: Structured waveguides in a monolithic sample, varying the laser power

Results

For monolithic samples, there was no obvious difference between a field inscribed in a depth of 100 μm and 300 μm , respectively. Hence, the carrier material was assumed to be fully accessible in its volume. Apart from the inscribed waveguides, the images showed many bubbles in the carrier material.

Lowering the laser power was connected with a decrease in the clarity of the lines, probably resulting from a decrease in the double bond consumption. The threshold for curing waveguides was 120 μW , but reasonable results only were achieved with a laser power of 180 – 200 μW . Note that in pure monomer the photoinitiator NDPD just needs 20 – 25 μW . The structured waveguides consisted of 80% carrier material and 20% monomer (chapter 4.4.3), so the laser power for reasonable curing obviously increased accordingly.

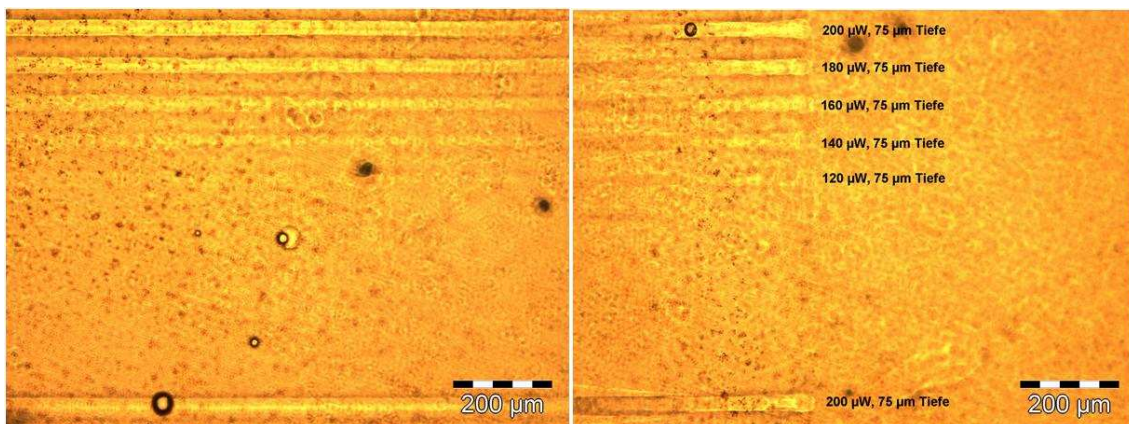


Figure 36: Structured waveguides in thin film, varying the laser power

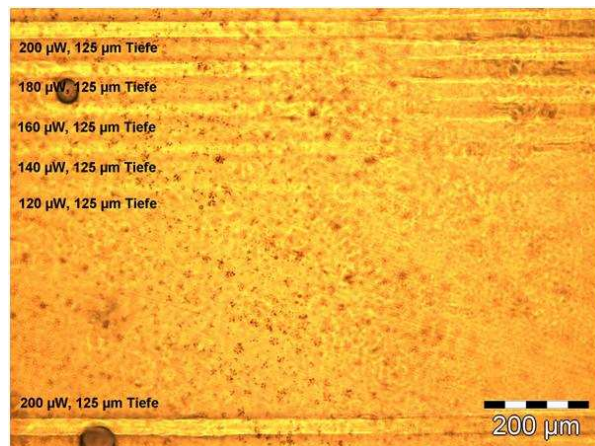


Figure 37: Structured waveguides in a thin film, varying the laser power

Results

Structuring of waveguides was also possible with thin films. Concerning the laser power, the results resembled those for monolithic samples. A difference to the monolithic samples was that the non-cured monomer was removed from the thin films by treatment with ethanol over night. Nevertheless, the material retained its orange coloration caused by the photoinitiator NDPD. The spots in the material probably resulted from the rather uneven surface caused by the preparation process. On the edges of the images, the film was unfortunately out of the focus point, because the thin films bent very strong during removal of remaining monomer with ethanol. However, the samples were flexible enough to be bent back to the initial state.

Obviously, the generation of waveguides was possible in each layer of the material, using at least 180 – 200 μW laser power to obtain satisfying results. A waveguide had a diameter of app. 35 - 37 μm (fig. 38).

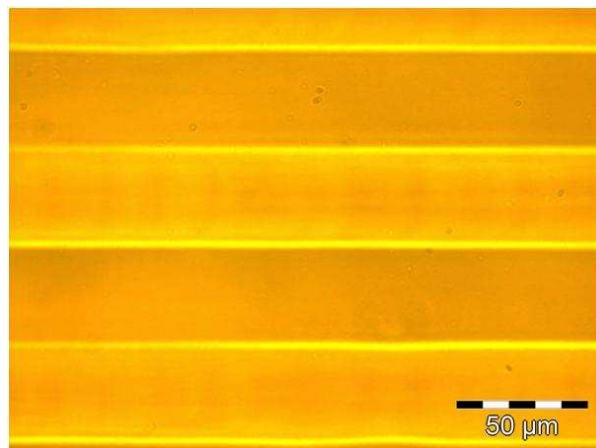


Figure 38: Microscope image of the structured waveguides

4.7.2. Varying the Speed of Structuring

The intensity of the laser in a spot could be increased either by raising the laser power or by decreasing the structuring speed. As default, the movement of the laser beam had a speed of 20 mm/min (as for the generation of waveguides in chapter 4.7.1), and the laser power could not be increased over 200 μW . Thus, a test series with variations in the speed of structuring with constant laser power (200 μW) was carried out. The slower the movement of the focus point, the higher became the intensity of photons and hence the

Results

energy in the focus. When the applied energy exceeded a certain threshold, the cladding material decomposed and the waveguide was “burned” (fig. 39 and 40).

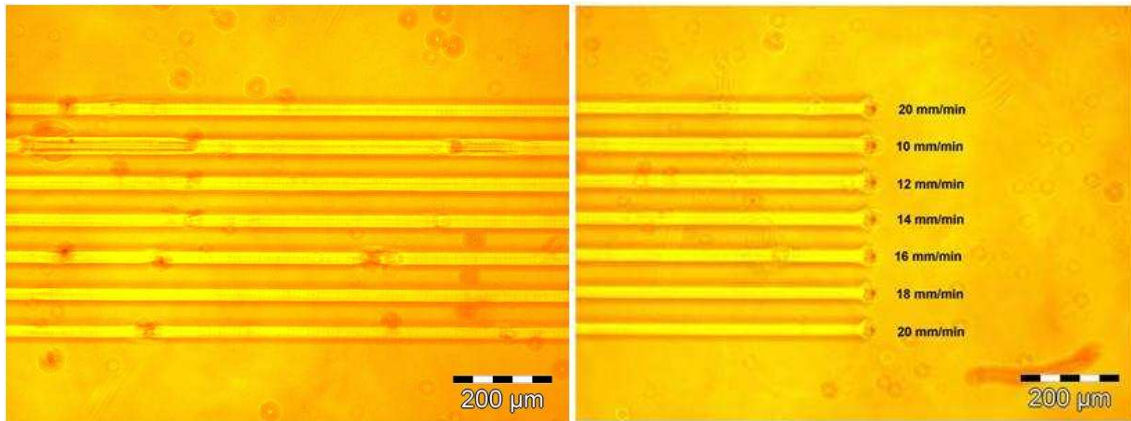


Figure 39: Waveguides in a monolithic sample, varying the structuring speed

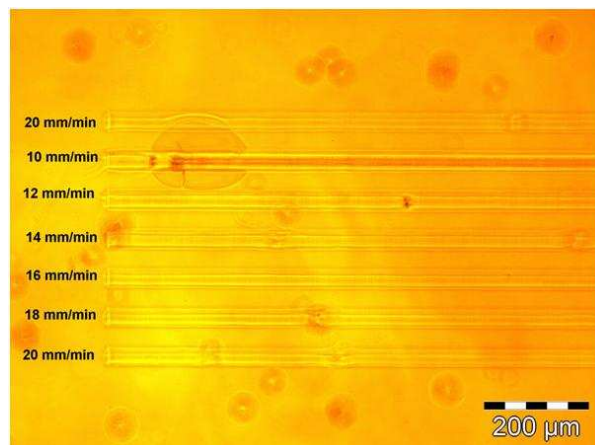


Figure 40: Microscope images of the an “burned” waveguide (10 mm/min)

Obviously, a movement of the laser beam of 10 mm/min and below, causes defect areas in the waveguides. The “burned” regions are easily visible by their dark appearance. Unfortunately, both monolithic films and thin films showed lots of bubbles in the material. These inclusions resulted probably from the formation of methanol and ethanol during the sol-gel process. Due to the short gel time for sample **D3**, the sol was apparently too viscous to get rid of all the gas-bubbles in the mixture. When a waveguide was structured through such a bubble, a defect occurred.

4.7.3. Functionality of Waveguides

The operation tests for the generated waveguides were carried out by Mag. Nicole Galler from the Institute of Experimental Physics at the Karl-Franzens-Universität in Graz. The images were again made by an optical microscope.

A structured monolithic sample (chapter 4.7.1) was prepared for cut-back measurements by breaking the samples normal to the waveguides on both sides to obtain a line field of app. 2 mm length. Now, both front sides of the samples contained a cut through all the lines of the field, which could be used for coupling light into and out of the waveguides, respectively (fig. 41).

Thus, the ability for waveguiding and the loss of optical intensity during the process could be determined. A monomode-phase with a wavelength of $\lambda = 594 \text{ nm}$ was used for the experiments.

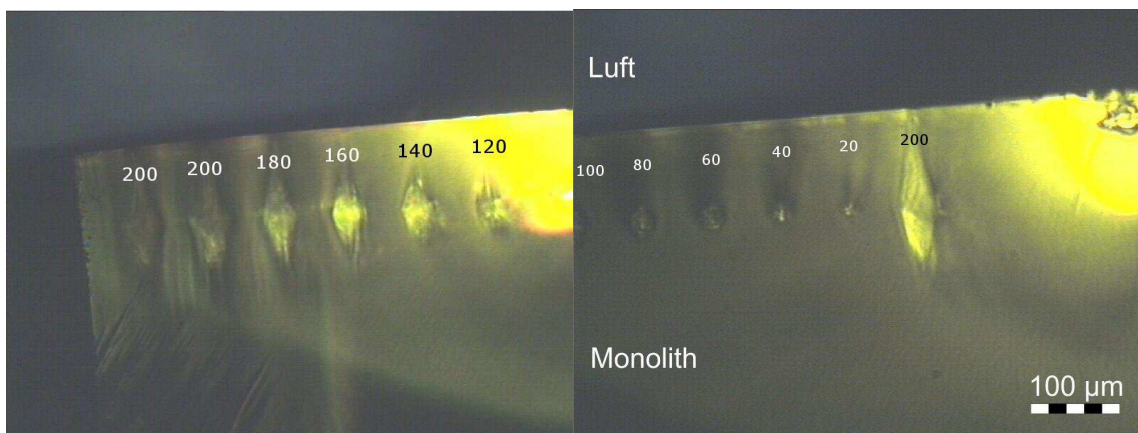


Figure 41: Front sides of structured waveguides in a monolithic sample

The images show monolithic samples with lines in $100 \mu\text{m}$ depth and decreasing laser power (compare to fig. 34). The clarity of the lines decreased with decreasing laser power ($200 \mu\text{W}$ to $20 \mu\text{W}$). In fig. 34, the view from above showed only waveguides structured with $120 \mu\text{W}$ and more. From the front side, lines structured with less than $120 \mu\text{W}$ are also clearly visible. If a waveguide was near the focus of light of the microscope, the spots brightened very obviously while the carrier material remained dark. This indicates that light could be coupled into the lines. $200 \mu\text{W}$ and focus point movement of $20 - 14 \text{ mm/min}$ should provide the best results.

Results

The following images show the front sides of the samples where the light was coupled into the waveguides (fig. 42).

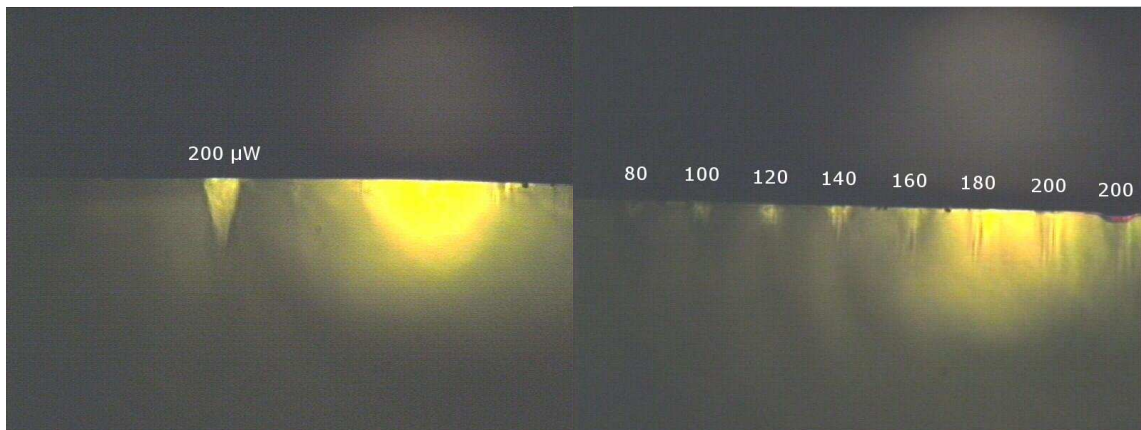
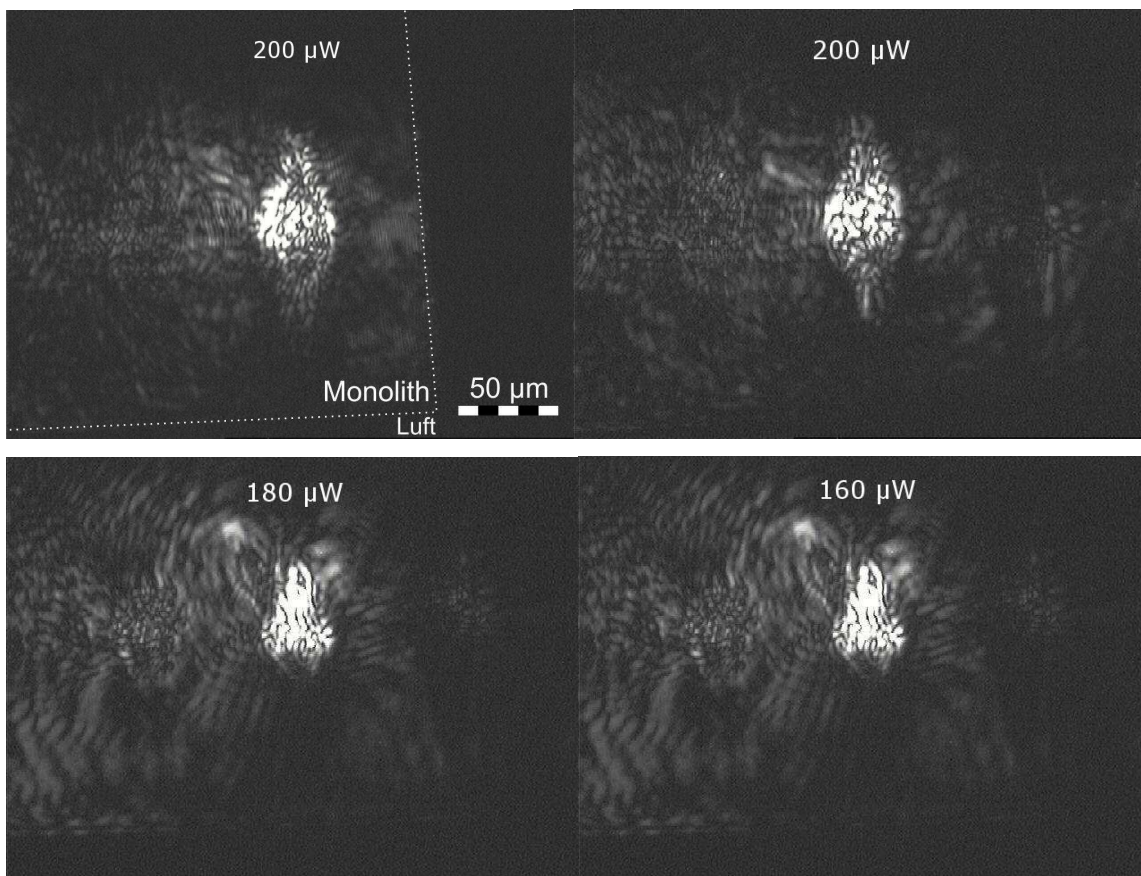


Figure 42: Incoupling of light in the structured waveguides

The light coupled out on the opposite front side of the sample. Figure 43 43 shows the intensity of the outgoing light depending of the laser power during the generation process:



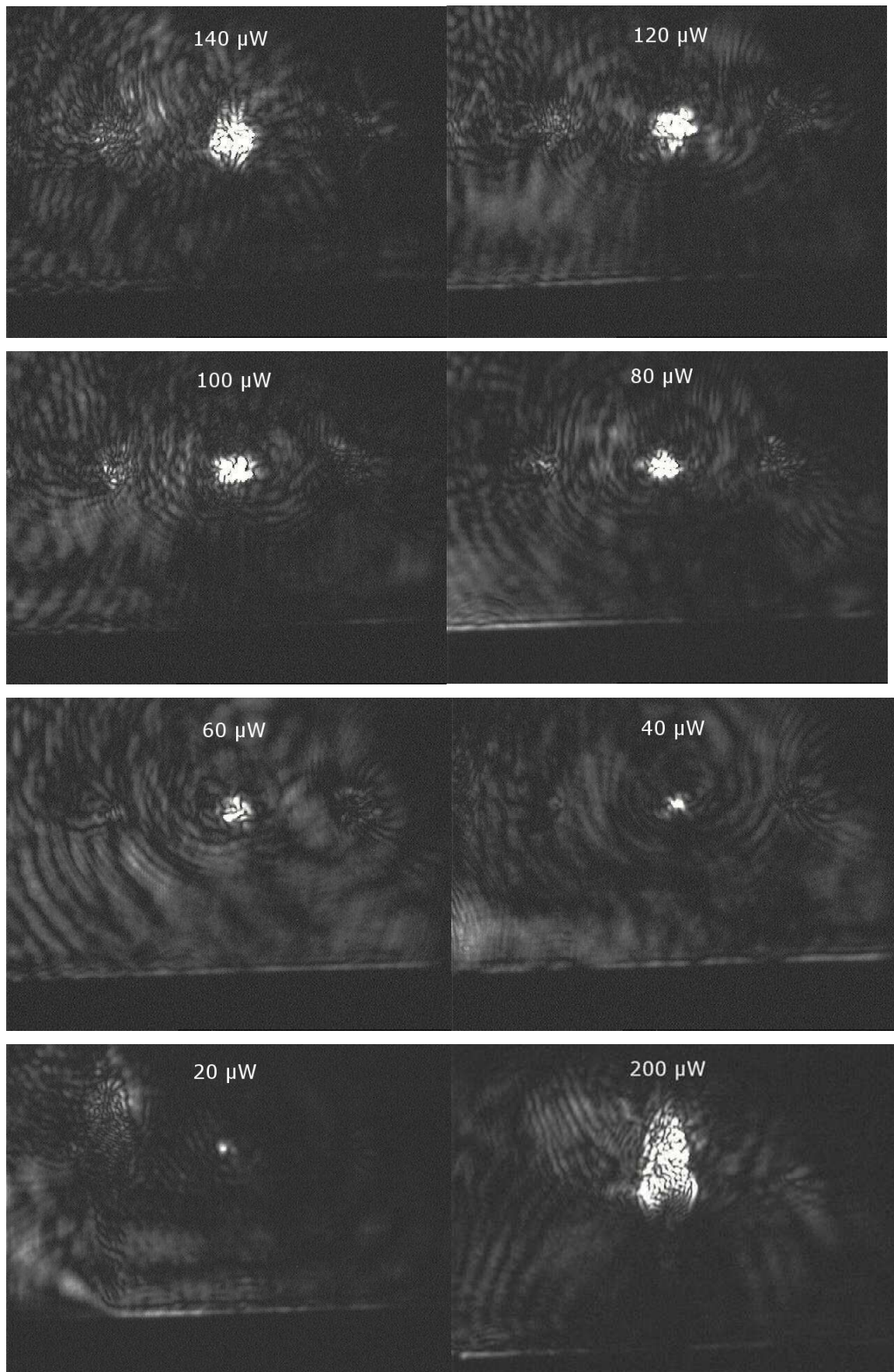


Figure 43: Intensity of outcoupled light for waveguides, structured various laser powers

Results

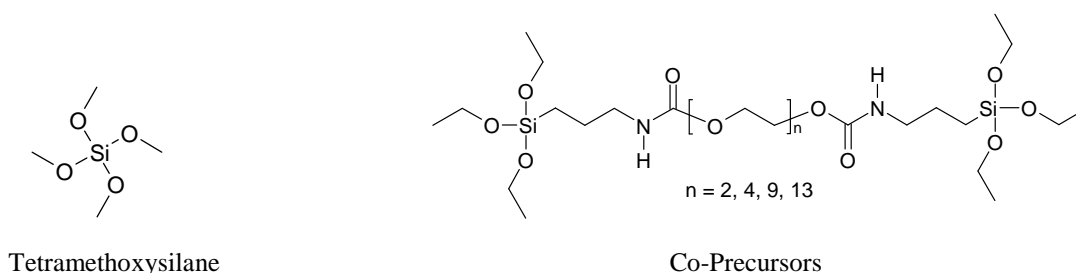
All the structured waveguides showed an ability to guide light rays, with a decrease of the diameter depending on the laser power the lines were generated at. Although the laser power decreased in the test series of fig. 34, the lines retained a constant diameter of app. 35 μm , given by the area of the laser focus. Hence, it could be assumed that for fig. 43 the decrease of the light spot diameter did not result from a decreased waveguide diameter. Note that the frequency of initiation processes and thus consumption of monomer was lower with a low power and thus the loss in the waveguides increased.

In general, the experiments showed much loss of optical intensity, which could be a result of an insufficient alignment, because the position of the waveguides in the optical path was not optimal. Hence, substantial parts of the incoming beam irradiated surrounding carrier material rather than the waveguide.

5. SUMMARY

The aim of the work was to establish a transparent, porous, silica based host material for polymeric waveguides. In this way, it should be possible to interconnect pre-aligned electric compounds of integrated circuits via direct writing of the waveguides by two photon polymerization (TPP). The porosity of the system was achieved by true liquid crystal templating by the L₃ “sponge” phase (fig. 5).¹⁴ It consisted of 1-hexadecylpyridinium chloride monohydrate as surfactant, 1-hexanol as auxiliary agent and 0.2M HCl as solvent. The correct ratio of the various compounds provided an isotropic system of pores with an adjustable size, appropriate for infiltrating a photocurable monomer.

A suitable silica sol-gel precursor was added to the pre-arranged template, in order to prepare a porous material in the desired shape. Common precursors for silica sol-gel chemistry are tetraalkoxysilane compounds, leading to a transparent but rigid network of SiO₂ units, which is very sensitive to fracturing. Therefore, inorganic-organic hybrid molecules with flexible polyethyleneglycol (PEG) spacers between two triethoxysilane heads were synthesized as co-precursor,⁴¹ in order to enhance the mechanical properties of the host material. In the course of this work, both monolithic samples and thin films were synthesized, whereas the template was removed subsequently to the gelation process by repeated treatment with ethanol solutions.



Various tests, concerning handling properties like gel time and transparency, showed that a formulation of 80 wt% tetramethoxysilane (TMOS) and 20 wt% of a co-precursor containing a PEG 400 spacer (sample **D3**) was a good trade-off between the requirements for transparency, mechanical stability and the processing of the liquid sol. Hence, that formulation was investigated in more detail and chosen as carrier material to be

Summary

infiltrated with an appropriate monomer. Although the mechanical properties probably would be further enhanced both with a higher content of co-precursor and a higher spacer length, either the sol would gel too fast or the material would become too turbid. A negative effect of the addition of co-precursor was the refractive index increase of the carrier material (n_1) compared to the respective polymer (n_2). To guarantee waveguiding, the difference had to be at least $\Delta n \geq 0.003$, with $n_2 > n_1$. In fact, mixtures of TMOS and co-precursor resulted in a refractive index of maximum $n_1 = 1.4100$. Despite this, the chosen monomer 2-phenoxyethylacrylate ($n_2 = 1.5200$) guaranteed the waveguiding ability.

Since the amount of precursor in the solvent, based on the R_w value, depended on the molecular weight of the respective silica source, adding a co-precursor with PEG spacer increased the content of precursor compounds in the sol. As a consequence, TGA measurements of material already infiltrated with monomer indicated, that the amount of monomer in the pores of the carrier material decreased from app. 53 wt% for samples made of pure TMOS (sample **A**) to app. 19 wt% for the threshold composition of sample **D3**. Determination of the pore size yielded contradictory results. While according to values calculated by BET and BJH approach of N_2 adsorption isotherms, the materials seemed to be microporous and dense, respectively, AFM images showed pronounced porosity with pore diameters of app. 80 - 280 nm for not enhanced samples. The carrier material was porous enough to be infiltrated with monomer and the AFM images confirmed the formation of the L_3 -sponge phase. However, the decrease of monomer content in the material had to be considered in the stipulated increase of the refractive index between cladding and waveguide. For the used formulation **D3**, a waveguide consisted of app. 20 wt% polymer and 80 wt% host matrix. Given a refractive index difference of at least $\Delta n \geq 0.003$ for waveguiding, this translated into a difference of $\Delta n \geq 0.015$ between waveguide and carrier material.

Concerning the mechanical properties determined by nano indentation, the values for both indentation modulus and indentation hardness of a sample **A** could be reduced up to two-third for samples consisting of the threshold content of co-precursor (**D3**). In fact, values of $E_{IT} = 2.374$ GPa and $H_{IT} = 0.253$ GPa (≈ 2.34 HV) could be achieved, resulting in a remarkable decrease of the tendency to macroscopic cracking of the material. However, for monolithic samples vaporization of the solvent ethanol resulted in macroscopic cracking for each precursor composition, but thin films remained crack free

Summary

for the enhanced sample **D3**. Unfortunately, the carrier material had no strong adhesion on the aluminum substrate and thus the gelation process was accompanied with a curvature of the host matrix.

The first attempts to generate waveguides by TPP were carried out successfully (fig. 44). Hence, lines could be structured in different depths with the suitable setting of 180 – 200 μW laser power and 20 mm/min movement of the laser beam. Decreasing the writing speed would result in a too high energy impact and a decomposition of the host material.

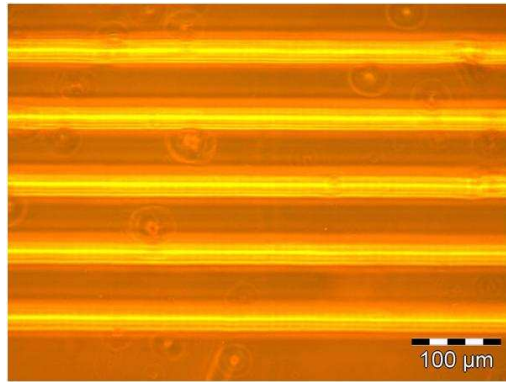


Figure 44: Generated waveguides in silica based matrix

Additionally, attempts to couple light into and out of the waveguides, respectively, were successful as well. The intensity of the light coupled out of the system depended on the laser power and writing speed used for the TPP.

Outlook

The aim of the work, to create waveguides in a silica-based matrix was successfully reached. However, there are still several issues to be solved for improved performance and processability:

- Short gelation time for enhanced samples.

In order to guarantee good handling with the colloidal solution, t_{gel} should not be lower than app. 2 h. Then processing approaches like spin coating could be used

Summary

to achieve films in a certain thickness for the respective purpose. Furthermore, the viscosity of the sol would remain rather low during the application on a substrate.

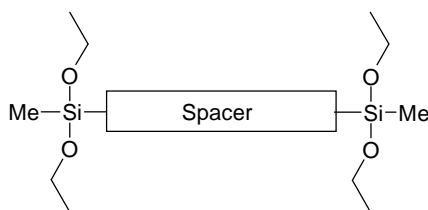
- Appearance of turbidity by applying co-precursors with a great polyethyleneglycol spacer length (\geq PEG600).
- Cracking of monolithic samples due to vaporization of ethanol.

For an improvement regarding these aspects, the following considerations could be applied:

- Due to inductive effects of the organic group on trialkoxysilanes, these compounds gel faster compared to tetraalkoxysilanes with the same alkoxy groups. A possible solution to slow down the gelation would be a change to other alkoxy groups as for instance:



Another way to adjust the gelation of the co-precursors in this work could be a substitution of an ethoxy group by a methyl group to decrease the number of groups for cross-linking and therefore the network density.

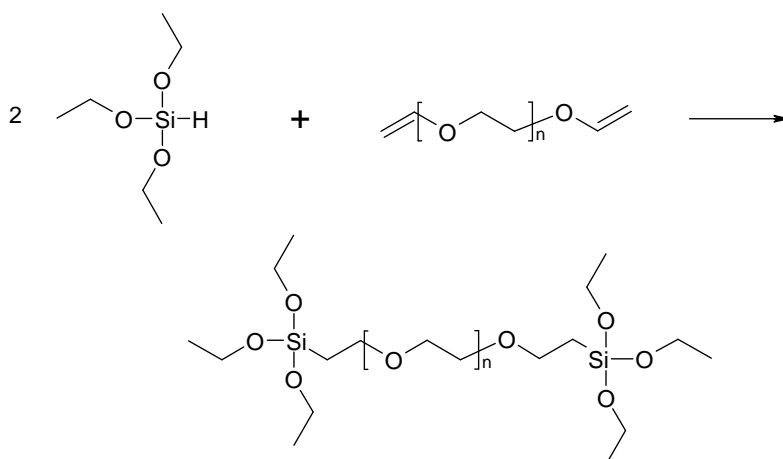


But note that in general substitution with organic groups leads to an acceleration of gelation.

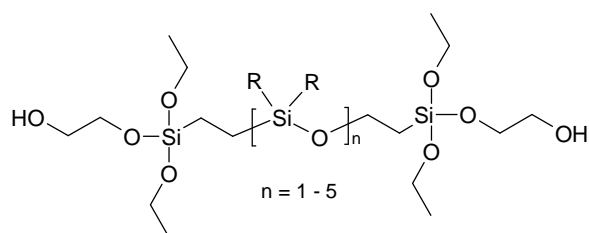
Additionally, t_{gel} could be influenced by a shift to higher pH values.

Summary

- In order to avoid interactions such as hydrogen bondings between urethane groups, which are well known to accelerate the gelation, the connection between the inorganic silica “heads” and the polyethyleneglycol spacer can be done in an alternative way. For example:

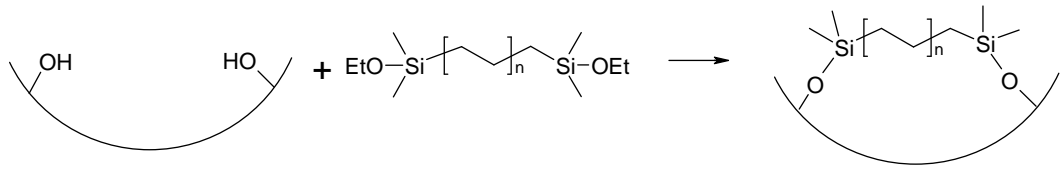


- Perhaps other spacer groups can slow down the gelation as well as enhance the mechanical properties of the porous material. For instance short polysiloxane groups could improve these properties. Hydroxyethoxysilane groups would ensure the solubility in water :



- Modification of the inner surface could lead to a higher resistance against cracking. The –OH groups of not reacted precursor can be utilized by conversion with a suitable reagents. Hence the material could be hydrophobized as well as strengthened by an additional layer in the pores. For example:

Summary



Note, that the pore diameter decreases by such an approach.

- To cast layers of the carrier materials onto a substrate, the adhesion between the two materials has to be guaranteed. Thus, surface modification of the carrier material with alkoxy silane has to be taken into account.

MATERIALS, DEVICES, ANALYSIS

Reagents were used with a common quality for the chemical synthesis. Furthermore, solvents were distilled prior to the application with common laboratory methods.

¹H NMR Spectra were recorded on a BRUKER AC-E-200 FT-NMR Spectrometer. The chemical shifts are given in ppm and referenced to tetramethylsilane (TMS). For all measurements deuterated chloroform (CDCl₃) was used as solvent with the calibration of the spectra regarding the solvent peak. The multiplicity is defined as following: (s = singlet, d = doublet, t = triplet, m = multiplet)

Infrared Spectra were obtained by the use of a Biorad FTS-135 FTIR Spectrometer with a Golden Gate ATR unit.

Refractive Indices were determined by an Abbe Refractometer manufactured by the Carl Zeiss Company, Germany and equipped with a Schott Geräte CT 050 Thermostat, filled with distilled water (adjusted at 20°C). The device operated at a wavelength of 589 nm (Sodium D-Line).

Thermogravimetric Analysis measurements were carried out on a DuPont Instruments 951 Thermogravimetric Analyzer connected to a 9900 Computer / Thermal Analyzer.

Differential Scanning Calorimetry was accomplished by a Shimadzu Differential Scanning Calorimeter, equipped with a TA-50 WSI Thermal Analyzer.

Nano Indentation was carried out by a Nano Indenter[®] XP, manufactured by NANO Instruments, Inc. Oak Ridge, Tennessee, U.S.A. and equipped with a Berkovich Indenter.

Scanning Electron Microscopy images were taken by a Phillips XL 30.

Atomic Force Microscopy images were taken by a Dimension 3100 system suitable for AFM and SPM microscopy, respectively. AFM was accomplished at the Institute of Electron Microscopy and Fine Structure Research on the Graz University of Technology.

ABBREVIATIONS

AFM	Atomic Force Microscopy
BDDA	1,4-Butandiol diacrylate
C_{solv}	Solvent content
CDCl_3	Deuterated chloroform
$\text{CpCl}\cdot\text{H}_2\text{O}$	1-Hexadecylpyridinium chloride monohydrate
DEG	Diethyleneglycol
DSC	Differential Scanning Calorimetry
E_{IT}	Indentation modulus
EEEA	2-(2-Ethoxyethoxy)ethyl acrylate
EtOH	Ethanol
H_{IT}	Indentation hardness
HEA	2-Hydroxyethyl acrylate
IBOA	Isobornyl acrylate
ICPTES	Isocyanopropyltriethoxysilane
IR	Infrared
LLC	Lyotropic Liquid Crystal
NDPD	1,5-Bis[4-N,N-(dimethylamino)phenyl]penta-1,4-dien-3-one
NI	Nano Indentation
NMR	Nuclear Magnetic Resonance
PCB	Printed Circuit Board
PEG	Polyethyleneglycol
PI	Photoinitiator
POEA	2-Phenoxyethyl acrylate
R_w	Ratio of alkoxy groups to water
SEM	Scanning Electron Microscopy
t_{gel}	Gelation time
TGA	Thermogravimetric Analysis
TMPA	Trimethylolpropane triacrylate
TMOS	Tetramethoxysilane
TPA	Two Photon Absorption
TPP	Two Photon Polymerisation
UA	Urethane acrylate

REFERENCES

- [1] Langer, G.; Riestler, M.; *"Two-photon absorption for the realization of optical waveguides on printed circuit boards"*; Proceedings of SPIE-The International Society for Optical Engineering; 6475; 64750X/64751-64750X/64759; **(2007)**
- [2] Kobayashi, J.; Matsuura, T.; Hida, Y.; Sasaki, S.; Maruno, T.; *"Fluorinated polyimide waveguides with low polarization-dependent loss and their applications to thermo-optic switches"*; Journal of lightwave technology; 16; 1024-1029; **(1998)**
- [3] Van Steenberge, G.; Geerinck, P.; Van Put, S.; Van Koetssem, J.; Ottevaere, H.; Morlion, D.; Thienpont, H.; Van Daele, P.; *"MT-Compatible Laser-Ablated Interconnections for Optical Printed Circuit Boards"*; Journal of lightwave technology; 2; 2083-1090; **(2004)**
- [4] Griese, E.; *"A high-performance hybrid electrical-optical interconnection technology for high-speed electronic systems"*; IEEE Transaction on advanced packaging; 24; 375-383; **(2001)**
- [5] Tooley, F.; Suyal, N.; Bresson, F.; Fritze, A.; Gourlay, J.; Walker, A.; Emmery, M.; *"Optically written polymers used as optical interconnects and for hybridisation"*; Optical Materials (Amsterdam, Netherlands); 17; 235-241; **(2001)**
- [6] Houbertz, R.; Schulz, J.; Froehlich, L.; Domann, G.; Popall, M.; Serbin, J.; Chichkov, B.; *"Inorganic-organic hybrid materials for real 3-D sub-mm lithography"*; Materials Research Society Symposium Proceedings; 780; 175-180; **(2003)**
- [7] Houbertz, R.; *"Laser interaction in sol-gel based materials - 3-D lithography for photonic applications"*; Applied Surface Science; 247; 504-512; **(2005)**
- [8] Schmidt, V.; Kuna, L.; Satzinger, V.; Houbertz, R.; Jakopic, G.; Leising, G.; *"Application of two-photon 3D lithography for the fabrication of embedded ORMOCER® waveguides"*; Proceedings of SPIE-The International Society for Optical Engineering; 6476; 64760P; **(2007)**
- [9] Inführ, R.; Pucher, N.U.; Heller, C.; Lichtenegger, H.C.; Liska, R.; Schmidt, V.; Kuna, L.; Haase, A.; Stampfl, J.; *"Functional Polymers by Two Photon Lithography"*; Applied Surface Science; 254; 836-840; **(2007)**
- [10] Kosswig, K.; Stache, H.; *"Die Tenside"*; München; Carl Hanser Verlag; **(1993)**
- [11] McMullen, E.W.; Ben Shaul, A.; Gelbart, W.M.; Journal of Colloid Interface; 98; 523-; **(1984)**
- [12] Israelachvili, J.N.; *"Thermodynamic and geometric aspects of amphiphile aggregation into micelles, vesicles and bilayers, and the interactions between them"*; Proc. Int. Sch. Phys. Enrico Fermi FIELD Full Journal Title:Proceedings of the International School of Physics Enrico Fermi; 90; 24-58; **(1985)**

- [13] Zimmermann, A.; *"Funktionelle Tenside als Template für Sol-Gel Prozesse"*; Diplomarbeit; Wien; Technische Universität Wien; Institut für Angewandte Synthesechemie (2006)
- [14] McGrath, K.M.; Dabbs, D.M.; Yao, N.; Edler, K.J.; Aksay, I.A.; Gruner, S.M.; *"Silica Gels with Tunable Nanopores through Templating of the L3 Phase"*; Langmuir; 16; 398-406; (2000)
- [15] Helfrich, W.; *"Lyotropic lamellar phases"*; J. Phys. Condensed Matter; 6; A79-A92; (1994)
- [16] McGrath, K.M.; Dabbs, D.M.; Yao, N.; Aksay, I.A.; Gruner, S.M.; *"Formation of a silicate L3 phase with continuously adjustable pore sizes"*; Science (Washington, D. C.); 277; 552-556; (1997)
- [17] Porte, G.; Appell, J.; Bassereau, P.; Marignan, J.; *"La to L3: a topology driven transition in phases of infinite fluid membranes"*; Journal de Physique (Paris); 50; 1335-1347; (1989)
- [18] Bhansali, S.H.; Malik, A.-S.; Jarvis, J.M.; Akartuna, I.; Dabbs, D.M.; Carbeck, J.D.; Aksay, I.A.; *"The Stability of L3 Sponge Phase in Acidic Solutions"*; Langmuir; 22; 4060-4064; (2006)
- [19] Porte, G.; *"Lammellar phases and disordered phases of fluid bilayer membranes"*; J. Phys. Condensed Matter; 4; 8649-8670; (1992)
- [20] Gomati, R.; Appell, J.; Bassereau, P.; Marignan, J.; Porte, G.; *"Influence of the nature of the counterion and of hexanol on the phase behavior of the dilute ternary systems: cetylpyridinium bromide or chloride-hexanol-brine"*; Journal of Physical Chemistry; 91; 6203-6210; (1987)
- [21] Hoffmann, H.; Thunig, C.; Munkert, U.; Meyer, H.W.; Richter, W.; *"From vesicles to the L3 (sponge) phase in alkyldimethylamine oxide/heptanol systems"*; Langmuir; 8; 2629-2638; (1992)
- [22] Filali, M.; Appell, J.; Porte, G.; *"Bilayers versus micelles in very dilute surfactant ternary systems"*; Journal de Physique II; 5; 657-664; (1995)
- [23] Cates, M.E.; Roux, D.; Andelman, D.; Milner, S.T.; Safran, S.A.; *"Random surface model for the L3-phase of dilute surfactant solutions"*; Europhys. Lett. FIELD Full Journal Title: Europhysics Letters; 5; 733-739; (1988)
- [24] Antonetti, M.; *"Silica nanocasting of lyotropic surfactant phases and organized organic matter: material science or an analytical tool?"* Philosophical Transactions of the Royal Society A; 364; 2817-2840; (2006)
- [25] Schubert, U.; Huesing, N.; *"Synthesis of Inorganic Materials"*; Second Edt; Weinheim; Wiley-VCH; pp. 192-234; 306-310. (2005)

- [26] Brandhuber, D.; Torma, V.; Raab, C.; Peterlik, H.; Kulak, A.; Huesing, N.; *"Glycol-Modified Silanes in the Synthesis of Mesoscopically Organized Silica Monoliths with Hierarchical Porosity"*; Chemistry of Materials; 17; 4262-4271; **(2005)**
- [27] LaFratta, C.N.; Fourkas, J.T.; Baldacchini, T.; Farrer, R.A.; *"Mehrphotonen-Mikrofabrikationen"*; Angewandte Chemie; 119; 6352–6374; **(2007)**
- [28] Li, L.; Fourkas, J.T.; *"Multiphoton polymerisation"*; Materials Today; 10; 30-37; **(2007)**
- [29] Kresge, C.T.; Leonowicz, M.E.; Roth, W.J.; Vartuli, J.C.; Beck, J.S.; *"Ordered mesoporous molecular sieves synthesized by a liquid-crystal template mechanism"*; Nature (London, United Kingdom); 359; 710-712; **(1992)**
- [30] Beck, J.S.; Vartulli, J.C.; Roth, W.J.; Leonowicz, M.E.; Kresge, C.T.; Schmitt, K.D.; Chu, C.T.W.; Olson, D.H.; Sheppard, E.W.; McCullen, S.B.; Higgins, J.B.; Schlenker, J.L.; *"A new family of mesoporous molecular sieves prepared with liquid crystal templating"*; J. Am. Chem. Soc.; 114; 10834-10843; **(1992)**
- [31] Attard, G.S.; Glyde, J.C.; Göltner, G.C.; *"Liquid crystal phases as template for the synthesis of mesoporous silica"*; nature; 378; 366-368; **(1995)**
- [32] Zhao, D.; Huo, Q.; Feng, J.; Chmelka, B.F.; Stucky, G.D.; *"Nonionic Triblock and Star Diblock Copolymer and Oligomeric Surfactant Syntheses of Highly Ordered, Hydrothermally Stable, Mesoporous Silica Structures"*; J. Am. Chem. Soc.; 120; 6024-6036; **(1998)**
- [33] Weissenberger, M.C.; Goltner, C.G.; Antonietti, M.; *"Mesoporous inorganic monoliths from lyotropic liquid crystalline polymer templates"*; Berichte der Bunsen-Gesellschaft; 101; 1679-1682; **(1997)**
- [34] Melosh, N.A.; Lipic, P.; Bates, F.S.; Wudl, F.; Stucky, G.D.; Fredrickson, G.H.; Chmelka, B.F.; *"Molecular and Mesoscopic Structures of Transparent Block Copolymer-Silica Monoliths"*; Macromolecules FIELD Full Journal Title:Macromolecules; 32; 4332-4342; **(1999)**
- [35] Hoffmann, F.; Cornelius, M.; Morell, J.; Froeba, M.; *"Silica-based mesoporous organic-inorganic hybrid materials"*; Angewandte Chemie, International Edition; 45; 3216-3251; **(2006)**
- [36] Malik, A.-S.; Dabbs Daniel, M.; Katz Howard, E.; Aksay Ilhan, A.; *"Silica monoliths templated on L3 liquid crystal"*; Langmuir FIELD Full Journal Title:Langmuir : the ACS journal of surfaces and colloids; 22; 325-331; **(2006)**
- [37] Dabbs, D.M.; Mulders, N.; Aksay, I.A.; *"Solvothermal removal of the organic template from L3 ("sponge") templated silica monoliths"*; Journal of Nanoparticle Research; 8; 603-614; **(2006)**

- [38] Brandhuber, D.; Huesing, N.; Raab, C.K.; Torma, V.; Peterlik, H.; *"Cellular mesoscopically organized silica monoliths with tailored surface chemistry by one-step drying/extraction/surface modification processes"*; Journal of Materials Chemistry; 15; 1801-1806; **(2005)**
- [39] Koch, T.R.; Wickham, P.P.; *"New method for the preparation of bismuth(III) triesters"*; Journal of Organic Chemistry; 44; 157-159; **(1979)**
- [40] Hachmann-Thießen, H.; *"Neue Synthesemethoden für funktionelle, biologisch abbaubare Polyester"*; Dissertation; Hamburg; Universität Hamburg; Institut für Technische und Makromolekulare Chemie **(2004)**
- [41] Kricheldorf, H.R.; Hachmann-Thiessen, H.; Schwarz, G.; *"Synthesis of trimethoxy- or triethoxysilane-end-capped polylactones via a bismuth(III)hexanoate-catalyzed one-pot-procedure"*; Journal of Biomaterials Science, Polymer Edition; 17; 721-733; **(2006)**
- [42] Yang, H.; Shi, Q.; Tian, B.; Xie, S.; Zhang, F.; Yan, Y.; Tu, B.; Zhao, D.; *"A fast way for preparing crack-free mesostructured silica monolith"*; Chemistry of Materials; 15; 536-541; **(2003)**
- [43] El-Safty, S.A.; Mizukami, F.; Hanaoka, T.; *"Transparent cubic Fd3m mesoporous silica monoliths with highly controllable pore architectures"*; Journal of Materials Chemistry; 15; 2590-2598; **(2005)**
- [44] Heller, c.; Pucher, N.U.; Seidl, B.; Kalinyaprak-Icten, K.; Ullrich, G.; Kuna, L.; Satzinger, V.; Schmidt, V.; Lichtenegger, H.C.; Stampfl, J.; Liska, R.; *"One- and two-photon activity of cross-conjugated photoinitiators with bathochromic shift"*; Journal of Polymer Science Part A: Polymer Chemistry; 45; 3280-3291; **(2007)**
- [45] Skoog, D.A.; Leary, J.J.; *"Principles of Instrumental Analysis"*; 4th Edt; Saunders College Publishing; pp. 568-579. **(1992)**
- [46] International Standard; ISO 14577-1; *"Metallic materials - Instrumented indentation test for hardness and material parameters - Part 1: Test method"*; **(2002)**
- [47] Friedbacher, G.; Rosenberg, E.; *"LV Skriptum: Analytische Chemie - Physikalische Analyse"*; **(2003)**
- [48] Jablonski, P.; *"Kalorimetrische Untersuchungen des Systems Polyethylenglykol/Wasser"*; Dissertation; Duisburg; Gerhard-Mercator-Universität Duisburg; Fakultät für Naturwissenschaften, Institut für Chemie **(2002)**